Spring 1-1-2018

Engineering the Phospholipid Monolayer on Fluorocarbon, Hydrocarbon, and Liquid Crystal Nanodroplets for Applications in Biosensing

Rajarshi Chattaraj
University of Colorado at Boulder, chattaraj.rajarshi@gmail.com

ENGINEERING THE PHOSPHOLIPID MONOLAYER ON FLUOROCARBON, HYDROCARBON, AND LIQUID CRYSTAL NANODROPLETS FOR APPLICATIONS IN BIOSENSING

by

RAJARSHI CHATTARAJ

B.Tech., National Institute of Technology, India, 2012

M.S., University of Colorado, Boulder, 2016

A thesis submitted to the

Faculty of the Graduate School of the

University of Colorado in partial fulfillment

of the requirement for the degree of

Doctor of Philosophy

Department of Mechanical Engineering

2018

This thesis entitled:
Engineering the Phospholipid Monolayer on Fluorocarbon, Hydrocarbon, and Liquid Crystal Nanodroplets for Applications in Biosensing
written by Rajarshi Chattaraj
has been approved for the Department of Mechanical Engineering

Andrew P. Goodwin (Chair)
Department of Chemical and Biological Engineering

Mark A. Borden
Department of Mechanical Engineering

Yifu Ding
Department of Mechanical Engineering

Xiaoyun Ding
Department of Mechanical Engineering

Daniel K. Schwartz
Department of Chemical and Biological Engineering

Date: March 14, 2018

The final copy of this thesis has been examined by the signatories, and we find that both the content and the form meet acceptable presentation standards of scholarly work in the above mentioned discipline.

ABSTRACT

Chattaraj, Rajarshi (Ph.D., Mechanical Engineering)

Engineering the Phospholipid Monolayer on Fluorocarbon, Hydrocarbon, and Liquid Crystal Nanodroplets for Applications in Biosensing

Thesis directed by Assistant Professor Andrew P. Goodwin

Nanodroplets (NDs) are liquid-in-liquid dispersions of ~100-800 nm size range that are often stabilized by a shell of lipids, polymer, proteins, or surfactants. NDs have been explored for a variety of biomedical applications, mostly involving drug formulation and delivery. However, the unique properties of encapsulated liquids, and the effects of interfacial chemistry on these properties, makes NDs potentially powerful candidates for new biosensing technologies. This dissertation explores different oil-in-water or fluorocarbon-in-water ND systems for in-solution sensing of biomarkers as both a platform for diagnostic assays and as a precursor to *in vivo* biosensing. Nanodroplets, because of their size, provide a large total surface area for analytes, making the assay both sensitive and fast compared to standard assay methods like ELISA. The type of response of the droplet to a stimulus also depends on the internal phase. This work includes NDs with three types of core materials: vegetable oil (fluorescent response), perfluorocarbon (PFC, acoustic response), and a thermotropic liquid crystal (LC, orientational response under polarized light). Each of these ND types is stabilized by a shell consisting of a primary saturated phospholipid and a lipopolymer, where the lipid shell is not only responsible for providing stability over reasonable time scales but also for recognizing analytes and causing a hierarchical change in the internal phase.

The first part of this study examined how ND response to a stimulus changes based on droplet aggregation. This was achieved by functionalizing the lipid monolayer shell of the NDs with aptamers or small molecules capable of specifically associating with dimeric or tetrameric analyte proteins. Through this process, vegetable oil NDs – doped with either a deactivated dye or an activating agent – were able to come together in the presence of a specific analyte, undergo content mixing, and generate a unique fluorescent signal. Similarly, PFC NDs were able to generate a higher acoustic response on aggregation. Streptavidin, as a proof-of-concept protein, and vascular endothelial growth factor, as a practical biomarker, were detected using droplet aggregation down to picomolar levels in bulk solution in 15-30 min.

The second part of this study focused on the effects of lipid monolayer phase separation and disruption on ND response. PFC NDs were found to have a heterogeneous monolayer, and acoustic response increased when unsaturated lipids were incorporated into the monolayer. Liquid crystal NDs were observed to transition from radial to bipolar orientations upon increasing the saturated lipid chain length above C16. Disruption of a gel phase C18 monolayer transitioned the orientation from bipolar back to radial. Using these observations for perfluorocarbon and LC droplets, a biologically relevant enzyme, phospholipase A_2, was detected down to clinically relevant nanomolar levels in 15-30 min: the enzyme cleaves the lipid molecules in the monolayer and disrupts its organization, generating a higher acoustic contrast for PFC NDs and an alternate orientation for internal phase molecules in LC NDs.

In summary, the current study details the effects of the ND lipid monolayer composition, phase separation, geometry, and functionalization on the internal phase response to stimuli, thus providing a framework for testing the potential of fluorocarbon, hydrocarbon, and liquid crystal nanodroplets as in-solution biosensors.

“Nitwit! Blubber! Oddment! Tweak!”

- *J.K. Rowling*

Acknowledgment

At the outset, I would like to extend my sincere gratitude towards my advisor Prof. Andrew P. Goodwin for his invaluable mentorship and constant support over a period of four years that I have been a part of his lab.

My thanks to Prof. Mark A. Borden for introducing me to the Department of Mechanical Engineering here at CU Boulder, for helping me initially explore the concepts of colloidal and interface science during my first two semesters in the department, and for taking the effort to advise me on various academic and related aspects from time to time.

I am grateful to Prof. Jennifer N. Cha for valuable suggestions regarding my research throughout the last few years.

I would also like to take this opportunity to thank the rest of my committee members – Professors Daniel K. Schwartz, Yifu Ding, and Xiaoyun Ding for taking the time to examine my research. I am particularly grateful to Prof. Borden and Prof. Schwartz for allowing me to use specialized equipment in their respective labs for my research.

None of my work would be possible without the perennial support of, and collaboration with, the members of our, and other, lab/s, both past and present, post-docs, graduate students, and undergraduates alike. Specifically, my thanks to our alumni Dr. Praveena Mohan for introducing me to the lab when I first joined, and Dr. Kaushlendra Kumar for helping me out whenever necessary with wet chemistry experiments in the lab and being a mentor in general. I'm immensely indebted to Dr. Adem Yildirim for sharing his ample expertise on colloidal silica particles and tissue culture, and for collaborating with me on multiple occasions. My thanks to Nicholas Blum,

Galen Goldscheitter, and Kavita Krishnan for being wonderful colleagues, and to my fellow current and former researchers – Ashray Parameswar, Kirsten Fitch, Michael Brasino, Glenn Hafenstine, Shambojit Roy, David Bull, Dr. Shashank Sirsi, Dr. Jameel Feshitan, and many others – for their suggestions, collaboration, and general support.

While not directly involved with my PhD, I have to thank my parents, and family members and friends – particularly, Dr. Sandipan Chattaraj, Dr. Riddhi Banerjee, Sayan Pal, Pratik Das, Ashish Kumar, and Jordan Heintz – for their support and a patient ear. Pratanu Mitra: for all those years before here. Lastly, there are those whose acquaintance I made for a short but unforgettable time during my presence in Boulder – you know who you are. Thank you all!

Table of Contents

Tables

Figures

Chapter 1. Introduction

The objective of this work is to characterize the interfacial properties of phospholipid-stabilized oil-in-water (o/w) nanodroplets (NDs) for biosensor design. There are two chief aspects to this objective. The first is to engineer a suitable phospholipid shell composition such that challenges by certain stimuli would alter the chemistry or geometry of the shell leading to a hierarchical effect on the droplet internal phase. Consequently, the second aspect involves the utilization of the change in internal (oil) phase properties as means to detect said stimuli. Before trying to understand these two aspects, let us first consider the general motivations for considering nanodroplets (or, nanoemulsions) as biosensors.

1.1. Droplet Characteristics.

Nanodroplets (NDs), are liquid-in-liquid dispersions that usually range from 100-800 nm in diameter and are kinetically stable for several days at a time[1]. These droplets, depending on their intended application, and are often stabilized by a layer of phospholipids, polymers, proteins, surfactants, or a combination of these at the aqueous-oil interface. This stabilizing layer provides biocompatibility, a platform for functionalization with targeting ligands, and a compartment for sequestration of small molecules such as drugs or fluorescent dyes. The present work concentrates on emulsions stabilized solely by phospholipids and a small amount of lipopolymer. Phospholipids are widely, commercially available, can tolerate incorporation with other amphiphilic molecules, and have the benefit of closely mimicking our cell membrane composition. A lipopolymer is

required to promote kinetic stability and slow aggregation or coalescence. In these studies, DSPE-PEG was used, where the incorporation of PEG (poly ethylene glycol) affords the droplets a degree of 'stealth' by diminishing non-specific protein interactions, which is thought to reduce the immune response from the host[2].

1.2. Applications of Droplets in Biology and Medicine.

The applications of nanodroplets can be wide-ranging, including in food, cosmetics, and pharmaceutical industries. For biomedical research, drug encapsulation and delivery are the most investigated [3,4]. These droplets are often designed to be responsive to various stimuli, including temperature[5], pH[6], light[7], or acoustic[8] or magnetic fields[9], such that exposure to the intended stimulus causes the droplets to release their drug payload at the desired site. As carriers, NDs containing non-toxic oils (e.g. soybean) can deliver antimicrobials, act as vehicles for mucosal delivery of vaccine, perform controlled delivery of cosmetics, and disperse active ingredients in skin layers[10]. In such cases, drug molecules are either miscible in the internal phase or simply rest between the surfactant chains in the droplet shell at the polymer/lipid/protein-oil interface. NDs may also have perfluorocarbons (PFC) as their internal phase. In such systems, ultrasound waves can trigger release of molecules like doxorubicin[8] or siRNA[11] encapsulated in the shell of the droplets, through thermal/mechanical effects induced by radiation forces or cavitation[12]. PFC NDs can also serve to image[13,14], ablate[15], treat[16] diseased tissue, or even fragment DNA[17], as detailed later.

1.3. Sensing of Diagnostic Biomarkers.

The importance of biomolecular sensing for diagnosing cancer and other diseases cannot be overstated. Different forms of cancer often upregulate various proteins in the blood, urine, and saliva, including growth factors, metalloproteinases, cytokines interleukins, antigens, lipases, and proteases [18–21]. The detection of elevated levels of such molecules in the bloodstream may enable earlier detection of cancerous cells as compared to standard imaging tests like MRI, CT, PET, or ultrasound, which are useful only after a tumor is well-formed. More commonly, irregular biomarker baseline levels in blood lead to difficulties in determining if a true positive result has been obtained.

The gold standard for non-oligonucleotide biomolecular assays is the ELISA (Enzyme Linked Immunosorbent Assay)[22]. ELISA is a highly sensitive method, which utilizes the attachment of the analyte to specific antibodies on functionalized surfaces. The one major drawback of ELISA and other surface-based assays is the considerable time required (on the order of hours) for diffusion-mediated ligand-receptor attachment, followed by multiple washing steps. Nanodroplet dispersions, because of their large total surface area, could perform the same function in bulk instead of being immobilized on a surface, provided that the direct interaction of NDs with biomolecules causes a detectable change in signal. At its simplest, bulk sensing involves simple mixing of ligand-functionalized nanoparticles and the blood/serum sample containing the biomarker molecule. This process thus eliminates the necessity of washing steps, while promising sensitivities similar to surface-based platforms for a significantly lower incubation time (minutes) on account of a greater available surface area for interaction. While polymeric and inorganic nanoparticles are often used in biomarker sensing platforms (usually through optical methods such as fluorescence or absorbance)[23], the use of o/w nanodroplets in similar scenarios have remained mostly unexplored. With their functionalizable stabilizing shell and variable/multiple internal

phases, amphiphile-coated emulsions could potentially serve as a promising platform for biosensing.

In-solution biosensing also represents a possible method for detection of specific biomolecules *in vivo* and quantifying local biomarker concentrations inside the body. It should be noted here that detection of molecules *in vivo* is not the same as tissue imaging, targeted or otherwise. In many cases, it might be helpful to measure the presence of markers like upregulated reactive oxygen species or acidic extracellular pH as indicators of inflammation/injury or a tumor microenvironment[24,25]. Fluorocarbon-based emulsions, bubbles, and vesicles have shown initial promise for *in vivo* biosensing, as discussed later.

1.4. Types of Nanodroplet Internal Phases.

The nanodroplets used in this work are of three distinct categories based on the type of their internal phase: hydrocarbon oils, fluorocarbon liquids, and liquid crystal forming oils. The unifying factor in these cases is that a specific analyte was able to cause the creation of a distinct corresponding signal in each of these systems. In the case of oil emulsions, a cyanine dye was added that produced a unique fluorescent signal as desired. On the other hand, emulsions with a perfluorocarbon core generated an acoustic response detectable by diagnostic ultrasound imaging. Lastly, the signal from emulsions with a liquid crystal core consisted of the varying orientation of liquid crystal molecules as visualized under cross-polarized light.

1.4.1. Hydrocarbon Derivatives. By far, the most common internal phases for o/w emulsions are hydrocarbon derivatives, including vegetable oil, silicone oil, alkanes, aromatics, etc. For biological applications, vegetable oils have the advantage of not being toxic. Unlike ultrasound-

responsive perfluorocarbons, or liquid crystals that can change their molecular alignment, the aforementioned oils do not generally have stimulus-responsive properties by themselves. Hence, hydrocarbon-derivatives (not counting liquid crystals) can be loaded with fluorescent dyes or nanoparticles, quantum dots, and magnetic nanoparticles, among others, to endow them with observable properties detectable under a light source of a specific wavelength or a magnetic field[26,27]. Lipophilic particles or dyes can be trapped between the shell molecules[28], while molecules with long alkane chains can easily be incorporated in large quantities in the internal oil phase, as detailed in **Chapter 2**.

1.4.2. Perfluorocarbons. About half of the studies in this work concern emulsions with a perfluorocarbon (PFC) core. Unlike vegetable oils or liquid crystals, perfluorocarbons can potentially be used as *in vivo* biosensors owing to their innate susceptibility to ultrasound imaging. Ultrasound, being inexpensive and safe, is a widely used modality in biological imaging. Standard ultrasound imaging is done in what is called a "B-mode", which involves the differential reflection of incident ultrasound waves based on a difference in acoustic impedances. However, such imaging is quite non-specific and often fails to distinguish different types of soft tissue.

Ultrasound contrast agents (UCAs) are a class of micro/nanoparticles that help enhance the resolution of an ultrasound image. UCAs usually contain or generate gas bubbles, the latter being excellent scatterers of sound waves in the range of 1-18 MHz. UCAs may be nanodroplets, nanobubbles, echogenic liposomes, or silica nanoparticles, but by far the most common of these is the microbubble (MB). MBs are 1-10 μm gas bubbles encapsulated by a stabilizing layer of lipids, polymers, or proteins[29]. These have been extensively explored for applications in contrast imaging of various organs and blood vessels, targeting to tumors or other tissues for specific imaging and drug delivery, sonoporation, blood-brain barrier disruption, and delivery of gases like

oxygen and NO[29–31]. However, because of their size, MBs are limited in their utility to the intravascular spaces in the body. To image or treat the tissue interstitial spaces, UCAs would need to be in the sub-micron size range to be uptaken. Unfortunately, nanobubbles are thermodynamically metastable with a low half-life and should theoretically produce a much lower contrast since scattering is inversely proportional to the sixth power of bubble radius[32].

In the early 2000s, Kripfgans et al designed microemulsions with a volatile perfluorocarbon (PFC) core, and discovered that with the application of a negative pressure gradient and/or heat, the volatile PFC could vaporize to form micron sized gas bubbles[33]. Further research on such "phase-shift" emulsions since Kripfgans' study have showed that emulsions as small as 200 nm in diameter could be vaporized using high intensity focused ultrasound (HIFU) to form microbubbles. This was especially promising, since these emulsions – or nanodroplets (NDs) – could first be allowed to extravasate through leaky tumor vasculature into the interstitial space, and then vaporized to generate MBs for contrast imaging or therapy.

1.4.2.1. Microbubble Characteristics. The ability of MBs to scatter clinically relevant ultrasound waves stems chiefly from its size and compressible internal gaseous phase. The compressible gas phase leads to oscillation of the bubble, which can be represented by the Rayleigh-Plesset model[34,35]:

$$\frac{P_B(t)-P_\infty(t)}{\rho_L} = R\frac{d^2R}{dt^2} + \frac{3}{2}\left(\frac{dR}{dt}\right)^2 + \frac{4\nu_L}{R}\frac{dR}{dt} + \frac{2S}{\rho_L R} \quad \text{.....(1.1)}$$

where, P_B and P_∞ are the internal pressure of the bubble and the external pressure, respectively, ρ_L and ν_L are respectively the density and kinematic viscosity of the surrounding liquid, and R and S are respectively the radius and surface tension of the bubble.

Equation 1.1 describes the oscillation of an ideal gas bubble trapped in a confined liquid, assuming negligible viscosity and compressibility of the medium and the bubble. To exploit the non-linear fundamental and higher-harmonics frequency response of microbubbles as a distinct signal compared to relatively linear tissue backscatter, we used, throughout this work, an imaging modality developed by Siemens, called contrast pulse sequences (CPS), or Cadence^{TM} mode. CPS involves transmitting of three pulses in each packet, consisting of two half-amplitude pulses at the beginning and end with a full-amplitude, phase-inverted pulse in the middle.

However, a naked air bubble would be thermodynamically unstable, which is why current microbubble formulations contain a stabilizing shell composed of lipids, polymers, or proteins. Evolving studies have highlighted the role of the shell in arresting gas dissolution to the surrounding medium[36]; the shell reduces the interfacial tension from ~72 mN/m (at the gas-water interface) to less than 5-10 mN/m, thus prolonging the MB half-life *in vivo* to several minutes. The shell also provides a damping element to the ultrasound-induced oscillation: seminal work by Hoff and others showed that, in the presence of a shell, bubble oscillation can be described through a second order, non-linear differential equation as relationship between bubble radius over time[37]. Lastly, while microbubbles can contain any gas, perfluorocarbons are preferred over air bubbles due to the insolubility of the former in physiological media. Certain PFC microbubble compositions like Definity® (octafluoropropane), Sonovue® (sulfur hexafluoride), and Optison® (octafluoropropane) are FDA-approved for echocardiography.

1.4.2.2. Phase-Shift Nanodroplets. PFC nanodroplets containing a volatile core have much the same broad applications as microbubbles, specifically in the fields of intratumoral imaging, drug and gene delivery, ablation therapy, embolotherapy etc[38]. The most common candidate for the core is perfluoropentane (PFP), which has a boiling point of 29^{o}C, but when contained inside a

droplet, it remains in a superheated state, increasing the boiling point to 60^{o}C or more depending on factors such as droplet size, shell composition, and ambient conditions. At room temperature, sub-micron PFP droplets can vaporize at peak negative pressures of approximately 5-7 MPa, all other factors remaining constant[39]. To be able to vaporize PFC NDs at lower peak pressures to risk minimal *in vivo* damage, Sheeran et al first formulated NDs by condensing gaseous perfluorobutane microbubbles[40]. On the other hand, very low boiling perfluobutane and octafluoropropane nanodroplets are likely to have low half-life and a tendency to non-specifically vaporize, resulting in a low signal-to-noise ratio. Perfluorohexane (PFH) has a bulk boiling point of 56^{o}C and hence requires high peak pressures (6-10 MPa) to vaporize in droplet form; but their stability is greater than PFB or PFP and thus they are easy to characterize. With this in mind, we chose PFH for most of our studies. PFH NDs are especially promising for enhancing the efficacy of HIFU-mediated ablation of cancerous tissue[41].

While numerous studies have been performed to determine the effect of the shell on microbubble stability, gas exchange, oscillation, cavitation, and general behavior under ultrasound, few such reports exist for NDs. It is generally known that vaporization threshold of PFC NDs is roughly inversely proportional to size and directly to core boiling point. The effect of interfacial structure and phase behavior on vaporization threshold have not been explored in detail, nor have the effects of aggregation and protein interaction. To be able to carry out these experiments, we have sought inspiration from previous reports on MBs[42] and vesicles[43]. Until a few years ago, the mechanism of droplet vaporization was unknown, as pressures required to vaporize droplets were much larger than predicted by existing theory. Pioneering work by Shpak et al.[44] elucidated that non-linear acoustic waves focus at a point inside a droplet due to i)the curvature of the droplet causing wave refraction, and ii) the mismatch in acoustic impedance between the droplet core and

the surrounding medium. This superharmonic focusing was shown to be responsible for nucleation events occurring inside the droplet. A corollary of this explanation was that larger droplets would vaporize more easily owing to their ability to focus more superharmonics. In our study with droplet aggregation, we extrapolated this observation to hypothesize that aggregates would also lead to increased constructive interference of the incident ultrasound waves, making vaporization easier.

Part of the allure for studying PFC emulsions, of course, is their potential as *in vivo* biosensors. Previously, microbubbles have been used to detect thrombin activity in non-occlusive blood clots by crosslinking (hence, stiffening) the microbubble shell, followed by decrosslinking by thrombin to generate a higher acoustic contrast[45]. Gas vesicles are also currently being explored for their capabilities in biomolecular sensing and bacterial/mammalian cell tracking[46]. Both microbubbles and phase-shift nanodroplets have been examined for their abilities in monitoring local temperatures, since ultrasound contrast usually increases with temperature[47,48]. We hope that these and our studies will spur increasing future work on UCAs as *in vivo* biosensors.

1.4.3. Liquid Crystals. Liquid crystals (LCs), specifically thermotropic LCs, are a class of materials that have unique properties in their nematic state, which is the state they exist at temperatures between crystalline (solid) and isotropic (liquid). LC molecules, or "mesogens" as they are often called, align themselves in the nematic state in different kinds of anisotropic arrangements in a confining aqueous medium depending on the composition and geometry of the aqueous-LC interface. The orientation of the mesogens affects LC molecules at distances from the interface much greater than that for isotropic liquids[49]. The short and long-range ordering of mesogens are affected chiefly by the interfacial free energy and bulk elasticity, and on occasion by defects formed in the LC bulk.

The orientational phases of LC alignment can be visualized under cross polarized light as various patterns, which may be used to deduce interactions that are occurring at the aqueous-LC interface, thus making them excellent platforms for surface-based detection of interfering molecules[50]. In traditional systems containing surface-anchored LCs, there are three major orientations: *planar* (where, the mesogens near the surface are aligned mostly parallel to the surface), *hometropic* (where, the mesogens are aligned perpendicular to the surface), and *tilted* (which represents an ordering of the mesogens somewhere between planar and homeotropic). Between crossed polarizers, homeotropic arrangement of mesogens produces a dark image relative to a planar arrangement. Different kinds of patterns in between may provide details about tilted alignments. In the case of emulsions, one can simply imagine the surface as a hollow sphere, from which mesogens either align axially (*bipolar,* analogous to *planar*) or radially (*radial,* analogous to *homeotropic*). Naked LC-in-water droplets are usually bipolar, whereas addition of surfactants/amphiphiles to the interface often leads to a radial orientation. This change may be predicted from the free energy *F* of the LC droplets[51].

$$F \approx \int W dA + \frac{K}{2}\int (\nabla n)^2 dV \quad \text{.....(1.2)}$$

where, *W* is the surface anchoring energy per unit area, *A* is the droplet surface area, *K* is the strain elastic modulus of the LC, and *V* is the droplet volume. Addition of surfactants at the interface to a near-saturation coverage changes *W* sufficiently to overcome the second elastic strain energy term of **Equation 1.2**, causing a realignment of LC mesogens.

The most widely known utility of LCs is of course in the displays of certain televisions or monitors. However, in the last decade or so, a case has been strongly made for biological applications of LCs chiefly due to the following reasons: i) Long range ordering of LC mesogens

translate the surface interactions to changes in the bulk; ii) High mobility of LC molecules at the interface; iii) Responsiveness to the magnitude of forces similar to those produced by human cells (in the order of pN)[52]. These properties have enabled surface-anchored LC surfaces and emulsions to work as promising platforms for biomolecular assays, as described in extensive detail in **Chapter 5.**

1.5. Formulation and Size-Isolation of Nanodroplets.

It is imperative while characterizing and utilizing nanodroplet formulations to minimize dispersity because nanodroplet response to a stimulus is often influenced by droplet size to some degree. Several well-established methods exist for formulating micro- and nanodroplets, including ultrasonication, vortexing, homogenization, condensation, nanoprecipitation, phase-inversion etc., all of which generate a polydisperse population[10,53,54]. More precise methods of emulsion formulation include microfluidics and polymer templates, each capable of producing samples with a less than 5% coefficient of variation[54,55]. The drawbacks of these techniques however include low yield, complex apparatus/expertise, and high production times[56].

Probe sonication of a mixture of the dispersed and continuous phases is perhaps the quickest and easiest way to generate a high yield of droplets ranging from tens of nanometers to several microns in size. To narrow the size distribution to obtain sub-micron droplets larger than 100 nm, we have employed the process of *differential centrifugation* (DC) extensively. Feshitan et al.[57] had previously shown how to formulate 1-2 and 4-5 μm microbubbles by DC. Our group was the first to employ a similar method for generating perfluorocarbon nanodroplets of mean sizes 300-400, 400-500, and >600 nm based on centrifugation speed variation. Briefly, this method involves

centrifuging the droplet sample produced by sonication at some low centrifuge speed, followed by centrifuging the supernatant at a higher specified speed, and so on: the pellet from the desired centrifugation step yields the sample of the corresponding size-range. Details can be found in **Chapter 3**. More recently, Guo et al.[58] prepared 1-3.1 and 2-4.6 μm PFC droplets employing DC, as predicted by an empirical mathematical model. Droplets with internal phase heavier than water (PFC, LC) can be isolated by pelleting them out, while droplets with vegetable oils are lighter than water and require a centrifugal filter to be isolated. We have used differentially centrifuged PFC, oil, and LC droplets throughout this work to improve the predictability of droplet stimulus-response.

1.6. Mechanism of Droplet Response to Stimulus.

For droplets to be useful in biosensing, they have to elicit a specific signal when challenged by a corresponding stimulus. For the three kinds of droplets mentioned above and studies in this work, the o/w interface consists of a stabilizing monolayer of phospholipids. Consequently, this work focuses on tuning/functionalizing the phospholipid monolayer so as to adjust droplet behavior in the presence of a stimulus. For the purposes of this report, we have concentrated on two ways to bring about a change in emulsion response: monolayer functionalization for droplet aggregation and reorganization/disruption of droplet monolayer.

1.6.1. Droplet Aggregation. A common technique underlying the design of biomolecular assays is aggregation of nanoparticles by analyte binding. For example, gold nanoparticles possess different optoelectronic properties in different functionalized and aggregated states[59]. Such properties have perhaps been most famously used by Mirkin and coworkers to design colorimetric

assays to detect polynucleotides based on aggregation of oligonucleotide-functionalized gold nanoparticles[60]. Similar strategies have been utilized for detecting DNA, proteins, small molecules and metal ions by aggregation of gold and silver nanoparticles[61]. Recently, gas vesicles were found to enhance acoustic response as a function of aggregation, which could make them viable candidates for molecular biosensors[46]. However, there is a surprising dearth of research on using similar concepts with nanodroplets, which could have different optical, electronic, acoustic, or magnetic properties based on the state of aggregation.

Chapters 2 and 3 describe our attempts to generate a unique signal based on the aggregation of lipid-stabilized nanodroplets. For example, droplet aggregation can lead to mixing of their internal phases, an idea that was applied to oil and PFC droplets. **Chapter 2** explores the case of vegetable oil droplets, where the internal droplet phase incorporated either a deactivated fluorescent dye or an activating molecule. On aggregation, content mixing occurs, and the dye was reactivated to generate a fluorescent response indicating analyte presence. **Chapter 3** reports the analyte-induced specific aggregation of perfluorohexane droplets, which increased the ultrasound response of the sample and allowed analyte detection. The mechanism of droplet aggregation based molecular detection was validated initially with *streptavidin* as a model analyte for proof-of-concept studies, followed by the detection of vascular endothelial growth factor (VEGF), a biomarker for cancer metastasis.

1.6.2. Reorganization/Disruption of Monolayer. The organization of lipids in the stabilizing monolayer of droplets in a gel, liquid, or mixed phase dictates the interaction of the shell with the internal phase. In certain cases, changes in the internal phase behavior may be observable, providing a basis for analyte detection. In the context of this report, tuning the lipid organization in the monolayer has been seen to result in varying acoustic response for PFC droplets, and varying

mesogen orientation for LC droplets. **Chapter 4** explores the lateral phase separation and domain formation of one or more saturated and unsaturated phospholipids in the perfluorohexane droplet shell and the consequent effects on ease of droplet boiling (in other words, ultrasound response). Structural variation in the monolayer on the nanoscale, including coexistence of different phases, indicated a heterogeneous and dynamic shell, capable of creating increased nucleation sites based on the shell composition. Finally, **Chapter 5** examines liquid crystal droplets, specifically the effect of increasing lipid acyl chain length on lipid interactions with liquid crystal mesogens in the core and on ambient protein interactions with the lipid molecules. Changes in droplet internal phase behavior due to reorganization/disruption of the lipid monolayer was utilized to detect a lipolytic enzyme, phospholipase A_2, which is present in insect and snake venom and can be a marker for certain kinds of cancer, pancreatitis and rheumatoid arthritis[62–64].

1.7. Specific Aims.

As discussed above, there are few studies investigating the potential of nanodroplets as biosensors. This work presents comprehensive preliminary insight into nanodroplet response to biological stimuli as a function of emulsion internal phase. Specifically, we set out to do the following:

1. Generate a fluorescent signal through specific aggregation of lipid-coated vegetable oil nanodroplets, as a way to detect biomarkers *in solution.*

2. Investigate the effects of aggregation, shell composition, and non-specific protein interactions on the acoustic response of lipid-coated perfluorocarbon nanodroplets, and apply the results to biomarker detection.

3. Examine the effect of lipid chain length and specific protein interactions on liquid crystal orientation in lipid-coated nanodroplets.

With respect to these specific aims, the following hypotheses were made:

- Aggregation of vegetable oil nanodroplets would lead to content mixing of the internal phase.
- Aggregation of perfluorohexane (PFH) nanodroplets would result in a lowering of acoustic intensity required to produce a discernible ultrasound response.
- A mixture of saturated and unsaturated lipids in the perfluorocarbon droplet monolayer would cause lateral phase separation and domain formation.
- Disruption of the lipid monolayer would lead to a higher ultrasound response from PFH nanodroplets.
- Presence of serum proteins would lower the vaporization threshold of PFH nanodroplets.
- Monolayer fluidity would directly affect the radial orientation of liquid crystals in lipid-coated nanodroplets.

1.8. References.

1. Sanchez-Dominguez, M., and Rodriguez-Abreu, C. (2016) *Nanocolloids: A Meeting Point for Scientists and Technologists*, Elsevier.

2. Immordino, M.L., Dosio, F., and Cattel, L. (2006) Stealth liposomes: review of the basic science, rationale, and clinical applications, existing and potential. *Int. J. Nanomedicine*, **1** (3), 297–315.

3. Julian McClements, D. (2012) Nanoemulsions versus microemulsions: terminology, differences, and similarities. *Soft Matter*, **8** (6), 1719–1729.

4. Choi, C.-H., Kim, J., Nam, J.-O., Kang, S.-M., Jeong, S.-G., and Lee, C.-S. (2014) Microfluidic Design of Complex Emulsions. *ChemPhysChem*, **15** (1), 21–29.

5. Mountford, P.A., Smith, W.S., and Borden, M.A. (2015) Fluorocarbon Nanodrops as Acoustic Temperature Probes. *Langmuir*, **31** (39), 10656–10663.

6. Liu, F., Lin, S., Zhang, Z., Hu, J., Liu, G., Tu, Y., Yang, Y., Zou, H., Mo, Y., and Miao, L. (2014) pH-Responsive Nanoemulsions for Controlled Drug Release. *Biomacromolecules*, **15** (3), 968–977.

7. Perrin, P., Porcar, I., and Tribet, C. (2003) Stimuli-responsive emulsions stabilized by polymeric surfactants. *Polym. Int.*, **52** (4), 465–470.

8. Rapoport, N. (2012) Phase-shift, stimuli-responsive perfluorocarbon nanodroplets for drug delivery to cancer. *WIREs Nanomed. Nanobiotechnol.*, **4** (5), 492–510.

9. Mahendran, V., and Philip, J. (2013) A methanol sensor based on stimulus-responsive magnetic nanoemulsions. *Sens. Actuators B Chem.*, **185**, 488–495.

10. Chime, S.A., Kenechukwu, F.C., and Attama, A.A. (2014) Nanoemulsions — Advances in Formulation, Characterization and Applications in Drug Delivery.

11. Burgess, M.T., and Porter, T.M. (2015) Acoustic Cavitation-Mediated Delivery of Small Interfering Ribonucleic Acids with Phase-Shift Nano-Emulsions. *Ultrasound Med. Biol.*, **41** (8), 2191–2201.

12. Mura, S., Nicolas, J., and Couvreur, P. (2013) Stimuli-responsive nanocarriers for drug delivery. *Nat. Mater.*, **12** (11), 991–1003.

13. Sheeran, P.S., Wong, V.P., Luois, S., McFarland, R.J., Ross, W.D., Feingold, S., Matsunaga, T.O., and Dayton, P.A. (2011) Decafluorobutane as a Phase-Change Contrast Agent for Low-Energy Extravascular Ultrasonic Imaging. *Ultrasound Med. Biol.*, **37** (9), 1518–1530.

14. Wilson, K., Homan, K., and Emelianov, S. (2012) Biomedical photoacoustics beyond thermal expansion using triggered nanodroplet vaporization for contrast-enhanced imaging. *Nat. Commun.*, **3**, 618.

15. Moyer, L.C., Timbie, K.F., Sheeran, P.S., Price, R.J., Miller, G.W., and Dayton, P.A. (2015) High-intensity focused ultrasound ablation enhancement in vivo via phase-shift nanodroplets compared to microbubbles. *J. Ther. Ultrasound*, **3**, 7.

16. Hannah, A.S., VanderLaan, D., Chen, Y.-S., and Emelianov, S.Y. (2014) Photoacoustic and ultrasound imaging using dual contrast perfluorocarbon nanodroplets triggered by laser pulses at 1064 nm. *Biomed. Opt. Express*, **5** (9), 3042–3052.

17. Kasoji, S.K., Pattenden, S.G., Malc, E.P., Jayakody, C.N., Tsuruta, J.K., Mieczkowski, P.A., Janzen, W.P., and Dayton, P.A. (2015) Cavitation Enhancing Nanodroplets Mediate Efficient DNA Fragmentation in a Bench Top Ultrasonic Water Bath. *PLOS ONE*, **10** (7), e0133014.

18. Ławicki, S., Zajkowska, M., Głażewska, E.K., Będkowska, G.E., and Szmitkowski, M. (2017) Plasma levels and diagnostic utility of VEGF, MMP-2 and TIMP-2 in the diagnostics of breast cancer patients. *Biomarkers*, **22** (2), 157–164.

19. Idris, A., Ghazali, N.B., and Koh, D. (2015) Interleukin 1β—A Potential Salivary Biomarker for Cancer Progression? *Biomark. Cancer*, **7**, 25–29.

20. Dijkstra, S., Mulders, P.F.A., and Schalken, J.A. (2014) Clinical use of novel urine and blood based prostate cancer biomarkers: A review. *Clin. Biochem.*, **47** (10), 889–896.

21. Cheng, Y.-S.L., Rees, T., and Wright, J. (2014) A review of research on salivary biomarkers for oral cancer detection. *Clin. Transl. Med.*, **3** (1), 3.

22. Tighe, P.J., Ryder, R.R., Todd, I., and Fairclough, L.C. (2015) ELISA in the multiplex era: Potentials and pitfalls. *PROTEOMICS – Clin. Appl.*, **9** (3–4), 406–422.

23. Chinen, A.B., Guan, C.M., Ferrer, J.R., Barnaby, S.N., Merkel, T.J., and Mirkin, C.A. (2015) Nanoparticle Probes for the Detection of Cancer Biomarkers, Cells, and Tissues by Fluorescence. *Chem. Rev.*, **115** (19), 10530–10574.

24. Kundu, K., Knight, S.F., Willett, N., Lee, S., Taylor, W.R., and Murthy, N. (2009) Hydrocyanines: A Class of Fluorescent Sensors That Can Image Reactive Oxygen Species in Cell Culture, Tissue, and In Vivo. *Angew. Chem. Int. Ed.*, **48** (2), 299–303.

25. Webb, B.A., Chimenti, M., Jacobson, M.P., and Barber, D.L. (2011) Dysregulated pH: a perfect storm for cancer progression. *Nat. Rev. Cancer*, **11** (9), 671–677.

26. Zarzar, L.D., Sresht, V., Sletten, E.M., Kalow, J.A., Blankschtein, D., and Swager, T.M. (2015) Dynamically reconfigurable complex emulsions via tunable interfacial tensions. *Nature*, **518** (7540), 520–524.

27. Mandal, S.K., Lequeux, N., Rotenberg, B., Tramier, M., Fattaccioli, J., Bibette, J., and Dubertret, B. (2005) Encapsulation of magnetic and fluorescent nanoparticles in emulsion droplets. *Langmuir*, **21** (9), 4175–4179.

28. Klymchenko, A.S., Roger, E., Anton, N., Anton, H., Shulov, I., Vermot, J., Mely, Y., and Vandamme, T.F. (2012) Highly lipophilic fluorescent dyes in nano-emulsions: towards bright non-leaking nano-droplets. *RSC Adv.*, **2** (31), 11876–11886.

29. Ferrara, K., Pollard, R., and Borden, M. (2007) Ultrasound Microbubble Contrast Agents: Fundamentals and Application to Gene and Drug Delivery. *Annu. Rev. Biomed. Eng.*, **9** (1), 415–447.

30. Liu, H.-L., Fan, C.-H., Ting, C.-Y., and Yeh, C.-K. (2014) Combining Microbubbles and Ultrasound for Drug Delivery to Brain Tumors: Current Progress and Overview. *Theranostics*, **4** (4), 432–444.

31. Fix, S.M., Borden, M.A., and Dayton, P.A. (2015) Therapeutic gas delivery via microbubbles and liposomes. *J. Controlled Release*, **209**, 139–149.

32. Pellow, C., Goertz, D.E., and Zheng, G. Breaking free from vascular confinement: status and prospects for submicron ultrasound contrast agents. (2017) *WIREs Nanomed. Nanobiotechnol*.

33. Kripfgans, O.D., Fowlkes, J.B., Miller, D.L., Eldevik, O.P., and Carson, P.L. (2000) Acoustic droplet vaporization for therapeutic and diagnostic applications. *Ultrasound Med. Biol.*, **26** (7), 1177–1189.

34. F.R.S, L.R.O.M. (1917) VIII. On the pressure developed in a liquid during the collapse of a spherical cavity. *Lond. Edinb. Dublin Philos. Mag. J. Sci.*, **34** (200), 94–98.

35. Leighton, T. (2012) *The Acoustic Bubble*, Academic Press.

36. Kwan, J.J., and Borden, M.A. (2012) Lipid monolayer collapse and microbubble stability. *Adv. Colloid Interface Sci.*, **183**–**184**, 82–99.

37. Hoff, L., Sontum, P.C., and Hovem, J.M. (2000) Oscillations of polymeric microbubbles: Effect of the encapsulating shell. *J. Acoust. Soc. Am.*, **107** (4), 2272–2280.

38. Sheeran, P.S., and Dayton, P.A. (2012) Phase-Change Contrast Agents for Imaging and Therapy. *Curr. Pharm. Des.*, **18** (15), 2152–2165.

39. Zhang, P., and Porter, T. (2010) An in vitro Study of a Phase-Shift Nanoemulsion: A Potential Nucleation Agent for Bubble-Enhanced HIFU Tumor Ablation. *Ultrasound Med. Biol.*, **36** (11), 1856–1866.

40. Sheeran, P.S., Luois, S., Dayton, P.A., and Matsunaga, T.O. (2011) Formulation and Acoustic Studies of a New Phase-Shift Agent for Diagnostic and Therapeutic Ultrasound. *Langmuir*, **27** (17), 10412–10420.

41. Zhou, Y., Wang, Z., Chen, Y., Shen, H., Luo, Z., Li, A., Wang, Q., Ran, H., Li, P., Song, W., Yang, Z., Chen, H., Wang, Z., Lu, G., and Zheng, Y. (2013) Microbubbles from Gas-Generating Perfluorohexane Nanoemulsions for Targeted Temperature-Sensitive Ultrasonography and Synergistic HIFU Ablation of Tumors. *Adv. Mater.*, **25** (30), 4123–4130.

42. Borden, M.A., Martinez, G.V., Ricker, J., Tsvetkova, N., Longo, M., Gillies, R.J., Dayton, P.A., and Ferrara, K.W. (2006) Lateral Phase Separation in Lipid-Coated Microbubbles. *Langmuir*, **22** (9), 4291–4297.

43. Veatch, S.L., and Keller, S.L. (2003) Separation of Liquid Phases in Giant Vesicles of Ternary Mixtures of Phospholipids and Cholesterol. *Biophys. J.*, **85** (5), 3074–3083.

44. Shpak, O., Verweij, M., Vos, H.J., Jong, N. de, Lohse, D., and Versluis, M. (2014) Acoustic droplet vaporization is initiated by superharmonic focusing. *Proc. Natl. Acad. Sci.*, **111** (5), 1697–1702.

45. Nakatsuka, M.A., Barback, C.V., Fitch, K.R., Farwell, A.R., Esener, S.C., Mattrey, R.F., Cha, J.N., and Goodwin, A.P. (2013) In vivo ultrasound visualization of non-occlusive blood clots with thrombin-sensitive contrast agents. *Biomaterials*, **34** (37), 9559–9565.

46. Shapiro, M.G., Goodwill, P.W., Neogy, A., Yin, M., Foster, F.S., Schaffer, D.V., and Conolly, S.M. (2014) Biogenic gas nanostructures as ultrasonic molecular reporters. *Nat. Nanotechnol.*, **9** (4), 311–316.

47. Guiot, C., Cavalli, R., Gaglioti, P., Danelon, D., Musacchio, C., Trotta, M., and Todros, T. (2004) Temperature monitoring using ultrasound contrast agents: in vitro investigation on thermal stability. *Ultrasonics*, **42** (1), 927–930.

48. Mountford, P.A., Smith, W.S., and Borden, M.A. (2015) Fluorocarbon Nanodrops as Acoustic Temperature Probes. *Langmuir*, **31** (39), 10656–10663.

49. Bai, Y., and Abbott, N.L. (2011) Recent Advances in Colloidal and Interfacial Phenomena Involving Liquid Crystals. *Langmuir*, **27** (10), 5719–5738.

50. Brake, J.M., Daschner, M.K., Luk, Y.-Y., and Abbott, N.L. (2003) Biomolecular Interactions at Phospholipid-Decorated Surfaces of Liquid Crystals. *Science*, **302** (5653), 2094–2097.

51. Lin, I.-H., Miller, D.S., Bertics, P.J., Murphy, C.J., Pablo, J.J. de, and Abbott, N.L. (2011) Endotoxin-Induced Structural Transformations in Liquid Crystalline Droplets. *Science*, **332** (6035), 1297–1300.

52. Lowe, A.M., and Abbott, N.L. (2012) Liquid Crystalline Materials for Biological Applications. *Chem. Mater.*, **24** (5), 746–758.

53. Solans, C., and Solé, I. (2012) Nano-emulsions: Formation by low-energy methods. *Curr. Opin. Colloid Interface Sci.*, **17** (5), 246–254.

54. Sheeran, P.S., Matsuura, N., Borden, M.A., Williams, R., Matsunaga, T.O., Burns, P.N., and Dayton, P.A. (2017) Methods of Generating Submicrometer Phase-Shift Perfluorocarbon Droplets for Applications in Medical Ultrasonography. *IEEE Trans. Ultrason. Ferroelectr. Freq. Control*, **64** (1), 252–263.

55. Mashaghi, S., Abbaspourrad, A., Weitz, D.A., and van Oijen, A.M. (2016) Droplet microfluidics: A tool for biology, chemistry and nanotechnology. *TrAC Trends Anal. Chem.*, **82**, 118–125.

56. Wang, X., Bukusoglu, E., and Abbott, N.L. (2017) A Practical Guide to the Preparation of Liquid Crystal-Templated Microparticles. *Chem. Mater.*, **29** (1), 53–61.

57. Feshitan, J.A., Chen, C.C., Kwan, J.J., and Borden, M.A. (2009) Microbubble size isolation by differential centrifugation. *J. Colloid Interface Sci.*, **329** (2), 316–324.

58. Mercado, K.P., Radhakrishnan, K., Stewart, K., Snider, L., Ryan, D., and Haworth, K.J. (2016) Size-isolation of ultrasound-mediated phase change perfluorocarbon droplets using differential centrifugation. *J. Acoust. Soc. Am.*, **139** (5), EL142-EL148.

59. Saha, K., Agasti, S.S., Kim, C., Li, X., and Rotello, V.M. (2012) Gold Nanoparticles in Chemical and Biological Sensing. *Chem. Rev.*, **112** (5), 2739–2779.

60. Elghanian, R., Storhoff, J.J., Mucic, R.C., Letsinger, R.L., and Mirkin, C.A. (1997) Selective Colorimetric Detection of Polynucleotides Based on the Distance-Dependent Optical Properties of Gold Nanoparticles. *Science*, **277** (5329), 1078–1081.

61. Vilela, D., González, M.C., and Escarpa, A. (2012) Sensing colorimetric approaches based on gold and silver nanoparticles aggregation: Chemical creativity behind the assay. A review. *Anal. Chim. Acta*, **751**, 24–43.

62. Chapman, R., Lin, Y., Burnapp, M., Bentham, A., Hillier, D., Zabron, A., Khan, S., Tyreman, M., and Stevens, M.M. (2015) Multivalent Nanoparticle Networks Enable Point-of-Care Detection of Human Phospholipase-A2 in Serum. *ACS Nano*, **9** (3), 2565–2573.

63. Liu, N.J., Chapman, R., Lin, Y., Bentham, A., Tyreman, M., Philips, N., Khan, S.A., and Stevens, M.M. (2016) Phospholipase A2 as a point of care alternative to serum amylase and pancreatic lipase. *Nanoscale*, **8** (23), 11834–11839.

64. Liu, N.J., Chapman, R., Lin, Y., Mmesi, J., Bentham, A., Tyreman, M., Abraham, S., and Stevens, M.M. (2016) Point of care testing of phospholipase A2 group IIA for serological diagnosis of rheumatoid arthritis. *Nanoscale*, **8** (8), 4482–4485.

Chapter 2. Aggregation of Hydrocyanine/Quinone Containing Vegetable Oil Nanodroplets as a Method for Sensing of Vascular Endothelial Growth Factor

A similar version of this chapter first appeared in the article: Chattaraj, R., Mohan, P., Besmer, J.D., and Goodwin, A.P. (2015) Selective Vaporization of Superheated Nanodroplets for Rapid, Sensitive, Acoustic Biosensing. Adv. Healthc. Mater., 4 (12), 1790–1795.

2.1. Abstract

Mutually-reactive, fluorogenic molecules are presented as a simple and novel technique for in-solution biosensing. The hypothesis behind this work was that aggregating droplets into close proximity would cause rapid mixing of their contents. To take advantage of this effect, a novel pair of fluorogenic redox molecules were designed to remain in lipid-stabilized oil droplets but mix once aggregated. First, the hydrophobic cyanine dye DiI was reduced with sodium borohydride to form a non-fluorescent analog (HDiI). Hydrophobic quinone derivatives were then screened as oxidizing agents, and it was found that p-fluoranil oxidized non-fluorescent HDiI back to fluorescent DiI. Next, HDiI and p-fluoranil were loaded into NEOBEE oil nanodroplets of average diameter 600 nm that were stabilized by a monolayer of DPPC, DSPE-PEG, and DSPE-PEG-biotin. Addition of streptavidin caused aggregation of droplets and the appearance of red fluorescent aggregates within 30 min. Next, Nanoparticle Tracking Analysis was used to record the fluorescence of the droplets and their aggregates. By integrating the fluorescence emission of the tracked droplets, streptavidin could be detected down to 100 fM. Finally, the droplets were

reformulated to sense for Vascular Endothelial Growth Factor (VEGF), a biomarker for tumor metastasis. Using anti-VEGF aptamers attached to DSPE-PEG incorporated into the nanodroplet monolayer, VEGF could also be detected down to 100 fM.

2.2. Introduction

Rapid, inexpensive detection of specific biomolecules is of tremendous importance for improving patient health, identifying infectious disease transmission patterns, and many other health-related goals. While ELISA is the gold standard of biomarker detection and quantification, its high cost and lengthy operation times inhibit wider utilization for routine assays. Detection of soluble analytes via sandwich assay has generally been achieved through the binding of an antibody bearing an additional moiety that can either serve as a label or amplify generation of detectable small molecules. In order to remove background signal, extensive washing steps are often required, increasing assay time and increasing the chances of operator error. A method that could provide a specific, detectable signal on a shorter time scale using inexpensive reagents would help to lower the barriers for more widespread assay development.

An alternative to a sandwich assay would be the generation of signal as a direct result of interaction with a specific biomarker in solution while minimizing background. Thus, signal must remain dark prior to mixing but become active once induced to do so during the detection phase. This method lends itself well to detection of enzymes that can naturally amplify activatable peptide-fluorophores[1,2]. Molecular beacons have also been designed to modulate their fluorescence intensity in response to nucleic acid or aptamer-bound analytes[3–5]. For more general analytes, aggregation is a highly customizable method of detection because it can be

induced with antibodies. Examples include shifts in plasmon resonance for metal nanoparticles and antibody-tagged iron oxide nanoparticles that change their magnetic relaxivity upon aggregation[6–9]. However, in each of these cases, background signal can hinder specificity. For example, typical molecular beacon quenching or energy transfer ON-OFF ratios are usually 5-30 (85-97% quenching/transfer efficiency)[10–12]. If instead the aggregation process were to cause the creation of signal rather than simply modulating it, a far greater specificity would be expected.

This paper presents an alternate strategy in which the aggregation of two oil droplets causes the mixing of two chemicals that react to produce an active fluorescent dye, thus creating fluorescence emission rather than shifting or modulating an existing signal. Previously, our lab developed oil droplets that could be induced to fuse together and mix their contents via DNA-mediated interactions inspired by the SNARE complex[13,14]. In the course of performing these studies, we found that simple aggregation could also allow contents to pass across the lipid monolayer, leading to content mixing even without fusion. Thus, droplets bearing reactive payloads could potentially be used as in-solution biosensors via analyte-induced aggregation. In this work, this aggregation-based detection scheme was validated against streptavidin as a model analyte and against VEGF-165 as a biomarker for metastatic cancer.

2.3. Experimental Section.

2.3.1. General Information. Fluorimetry studies were performed on a Photon Technology International fluorimeter with lamp power supply model LPS-220B, motor driver model MD-5020, and shutter control model SC-500. ^{1}H-NMR studies were performed on a Bruker AV-III 400 MHz NMR spectrometer with ICON NMR in automation, while ^{13}C NMR studies were run at 100 MHz. $CDCl_3$ was used as solvent, chemical shifts are reported in ppm, while coupling

constants, *J*, are reported in Hertz. Multiplicities in the spectra are represented by d (doublet), t (triplet), m (multiplet), and b (broad). High-resolution mass spectra (HRMS) were recorded using a Waters Synapt G2; spectra are reported as m/z (relative intensity). 1 µL of saturated LiCl in acetonitrile was added to 50 µL of sample, masses are reported for either [M+] or [$M+H^+$] ion. Millipore water was obtained from a Milli-Q Advantage A-10 water purification system (MilliPore, USA). Microscopy images were captured using a Zeiss Axio Imager A2. Nanoparticle Tracking Analysis was performed on a Malvern NanoSight LM10.

2.3.2. Synthesis of Reduced Dye. 2.5 mg (2.1 µmol) of 1,1'-dioctadecyl-3,3,3'3'-tetramethylindocarbocyanine perchlorate (DiIC_{18}(3), Molecular Probes) was dissolved in 1 mL 200 proof ethanol. 0.24 mg (6.3 µmol) of sodium borohydride (Acros Organics) in 100 µL in ethanol was added dropwise to the DiI solution with continuous stirring, followed by another 5-10 min stirring at RT to make a colorless solution. The ethanol was removed by rotary evaporator, followed by addition of 3 mL of chloroform. The chloroform was washed twice with 1 mL Millipore water and once with 1 mL brine, followed by drying over anhydrous magnesium sulfate, filtering through silica, and concentration by rotary evaporator. For storage, 1 mL of NEOBEE oil (Spectrum Chemical Mfg. Corp.) or soybean oil (MP Biomedicals, LLC) was then added to the flask and mixed in the rotary evaporator without vacuum for 10 min. The solution of reduced DiI in oil was stored in a glass vial wrapped with aluminum foil at 2-8 °C. ^{1}H NMR (400 MHz, $CDCl_3$): δ 7.17-7.07 (m, 4H, Ar-H), 7.03-7.01 (m, 2H, Ar-H), 6.83-6.75 (m, 2H, Ar-H), 6.68 (t, 1H, -C<u>H</u>=C<u>H</u>-C<u>H</u>=, *J* = 7.3 Hz), 6.55 (d, 1H, -C<u>H</u>=C<u>H</u>-C<u>H</u>=, *J* = 7.8 Hz) 6.47 (d, 1H, -C<u>H</u>=C<u>H</u>-C<u>H</u>=, *J* = 7.7 Hz), 5.41-5.32 (m, 2H, -C<u>H</u>=C<u>H</u>-C<u>H</u>=), 3.80-3.55 (m, 2H, N-C<u>H_2</u>-CH_2), 3.22-2.99 (m, 2H, N-C<u>H_2</u>-CH_2), 1.95-0.85 (82H, aliphatic region); ^{13}C NMR (100 MHz, $CDCl_3$): δ 154.34, 150.34,

145.29, 139.09, 138.59, 130.27, 127.58, 127.27, 121.68, 121.57, 121.40, 118.54, 116.98, 106.73, 105.48, 94.81, 78.42, 45.69, 45.03, 44.08, 42.26, 31.94, 29.71, 29.68, 29.63, 29.56, 29.48, 29.37, 28.33, 28.07, 27.40, 27.23, 26.31, 25.96, 25.89, 24.14, 22.70, 14.13. HRMS (ESI+) for $C_{59}H_{98}N_2$ [M+H$^+$]: calculated: 835.7808, experimental: 835.7792.

2.3.3. Activation Studies of Reduced Rye. The following quinones were used for re-oxidation studies: p-fluoranil (Alfa Aesar), p-chloranil (Merck KGaA), 2,3-dichloro-5,6-dicyano-1,4-benzoquinone (DDQ, Acros Organics), 1,4-dihydroxyanthraquinone, (DHAQ, Acros Organics), 9,10-phenanthrenequinone (Chem-Impex Int'l Inc.), and 3,3',5,5'-tetra-*tert*-butyldiphenoquinone (DPQ, TCI Co., Ltd.). For each study, a 2.14 mM solution of each of these reagents was made in NEOBEE oil to match the ~2.14 mM solution of HDiI in NEOBEE oil. Equal volumes of reduced DiI and the respective oxidizing agent were mixed for 5 min. Next, each solution was diluted 2000X in NEOBEE oil, and fluorescence measurements were recorded (λ_{exc} = 532 nm). Analogous experiments were also performed in soybean oil for HDiI and p-fluoranil. The fluorescence spectra of 1.07 mM solution of commercial DiI and HDiI alone were taken as a positive and negative control, respectively. Since a 1:4 molar ratio of reduced DiI:p-fluoranil proved optimal, NMR spectra for the reactivated DiI was recorded using this ratio. ^{1}H-NMR (400MHz, $CDCl_3$): δ 8.42 (b, 1H, -C<u>H</u>=C<u>H</u>-C<u>H</u>=), 7.39 (b, 2H, Ar-H), 7.27 (b, 2H, -C<u>H</u>=CH-C<u>H</u>=), 7.14 (b, 1H, Ar-H), 6.85 (b, 1H, Ar-H), 4.18 (b, 4H, N-C<u>H$_2$</u>-CH$_2$-), 1.88-0.85 (82H, aliphatic region); ^{13}C NMR (100 MHz, $CDCl_3$): δ 173.98, 142.14, 140.63, 128.87, 125.42, 122.13, 111.07, 103.36, 53.43, 49.16, 44.54, 31.93, 29.71, 29.66, 29.62, 29.46, 29.43, 29.37, 28.06, 27.53, 26.79, 22.69, 14.12. HRMS (ESI+) for $C_{59}H_{97}N_2$ [M+]: calculated: 833.7652, experimental: 833.7659.

2.3.4. Synthesis of Anti-VEGF Aptamer-Maleimide Conjugate. Prior to all experiments, Tris-buffered saline (TBS) was prepared to a final concentration of 10 nM Tris base (Fisher Scientific) and 100 mM NaCl (Fisher Scientific), adjusted to a pH of 7.4 with dilute HCl. A di-thiol modified version of an anti-VEGF aptamer (5'-/5ThioMC6-D/TTTTCCCGTCTTCCAGACAAGAGTGCAGGG-3') was purchased from Integrated DNA Technologies. Modifying a literature procedure[15], 100 μL of a 100 μM aptamer stock solution was mixed with 100 μL of 10mM aqueous solution (pH adjusted to 7.4) of Tris(2-carboxyethyl) phosphine hydrochloride (TCEP, Strem Chemicals Inc.), and reacted at 350rpm for 45 mins. Purification was carried out through a centrifugal filter (MWCO 3000 Da) at 4000 rcf for 20 mins, followed by washing twice with milipore water. 100 μL of the re-suspended final product containing the activated aptamer was mixed with 250 μL of a 2mg/mL DSPE-PEG2000-Maleimide (Avanti Polar Lipids, Inc.) solution in 1x PBS (Fisher Scientific), and reacted at 75^0C for 1 hr. The product solution was then centrifuged under the same conditions mentioned previously, followed by washing in water, and then in TBS. The aptamer-maleimide product was re-suspended in TBS to form a final aptamer concentration of 100 μM.

2.3.5. Formulation of Nanodroplets. For droplet formulation, a stock solution of DPPC (Avanti Polar Lipids, Inc.) was prepared as described previously[13]. DSPE-PEG2000 and DPSE-PEG2000-Biotin (both from Avanti Polar Lipids, Inc.) were individually dissolved in TBS and added to the stock DPPC solution to make a final concentration of 1.3 mM DPPC/40 μM DSPE-PEG2000/15 μM DSPE-PEG2000-Biotin. To make anti-VEGF aptamer coated nanodroplets, DSPE-PEG2000-Biotin was replaced by the aptamer-maleimide conjugate to a final concentration of 150 nM. This lipid-PEG-biotin (or lipid-PEG-aptamer) mixture was then stirred at 75°C for 30-

40 min and allowed to cool to RT. Two NEOBEE oil solutions were prepared: one with 2.14 mM HDiI (**A**), and one with 8.56 mM p-fluoranil (**B**). 40 μL of either solution **A** or solution **B** was added per mL of the lipid-PEG-biotin (or lipid-PEG-aptamer) stock to make a 4 v/v% mixture, and probe-sonicated (Branson SLPe, 40 kHz) for two 1min cycles – 1s on, 9s off – at 70% amplitude. The emulsion was then centrifuged at 1500 *g* for 1 min, followed by drawing ~0.5 mL of the supernatant, making sure to avoid the pellet at the bottom and the flotsam on top; the supernatant was then centrifuged using a 0.45 μm centrifugal filter (VWR International) at 12,000 *g* for 4.5 min, followed by washing with TBS under the same conditions. The droplet pellet in the filter was resuspended in 150 μL TBS per mL emulsion centrifuged. Plain NEOBEE oil droplets (without either dye or p-fluoranil) were also prepared in the same way for characterizing droplet size distribution. Droplet size distribution and concentration was measured by Nanoparticle Tracking Analysis (NTA).

2.3.6. Aggregation of Nanodroplets. Stock analyte solutions of streptavidin (Pierce) of varying concentrations were prepared in TBS (or HyClone-characterized Fetal Bovine Serum (FBS) or Bovine Plasma (Sodium Citrate) as required; FBS and Bovine Plasma were purchased from ThermoFisher Scientific and Pel-Freez Biologicals respectively). Stock solutions of Human VEGF-165 (Shenandoah Biotechnology Inc.) were also prepared in TBS. Next, 10 μL (or approximately 7.5×10^9 droplets, as determined by NTA) each of HDiI and p-fluoranil droplets in TBS were mixed together. Additional 30 μL TBS was added, followed by 50 μL of an appropriate analyte stock solution to attain the analyte concentrations mentioned in the text and a total volume to 100 μL. (Biotinylated droplets were incubated with streptavidin, while aptamer-coated droplets were incubated with VEGF dimer) The mixture was shaken in a thermomixer (Eppendorf) at 37°C

for 30 min. The samples were then imaged in epifluorescence mode in a red channel (Zeiss). 10 µL of each sample was taken and diluted to 1 mL in TBS for NTA characterization. For time-dependent studies of biotinylated droplet sample in the absence of streptavidin (Control), 10 µL of the same sample was characterized using the NTA setup after 0, 15, 30, 60, and 120 min after mixing and incubation.

2.3.7. Nanoparticle Tracking Analysis and Fluorescence Studies. Size distribution and concentration of NEOBEE oil droplets were determined using Nanoparticle Tracking Analysis. To determine fluorescent intensity of aggregated versus non-aggregated droplets, a push-pull fluorescence filter in the NanoSight setup was used, which allowed for visualization of fluorescent droplets/aggregates only, eliminating contribution to the response from the rest. Three 60 s videos were recorded for each sample: in order to compare samples, criteria such as camera exposure level (maximum, at 16) and threshold detection level (18) were kept same for all experiments. The intensity vs. size data was analyzed by the NTA 3.0 software (Malvern). A one-tailed Student's t-test, where P-values were obtained using against the null hypothesis that the means were equal, confirmed the statistical significance of the data.

2.4. Results and Discussion.

2.4.1. Synthesis and Evaluation of Cyanine-based Switchable Fluorophore. To obtain efficient and rapid signal generation, redox reactions were chosen as a method of activation that could be made specific to droplet aggregation with some simple design rules. Redox reactions leading to unmasking of fluorescent dyes has been a highly successful approach for the sensing of

Reactive Oxygen Species (ROS)[16–20]. We theorized that the same effect might be obtained using oil-soluble oxidants. For the dye structure, we were directly inspired by hydride-reduced cyanine dyes developed by Murthy and coworkers[21,22] and Nagano and coworkers[23]. Here, 1,1'-dioctadecyl-3,3,3'3'-tetramethylindocarbocyanine perchlorate (DiI), a common membrane stain based on Cy5, was used instead because of its strong partitioning to an oil phase due to its two C_{18} chains. Reduced DiI (HDiI) was prepared by reacting with sodium borohydride in ethanol, followed by extraction and filtration through a silica plug (**Figure 2.1.A**)[21,22]. The resulting molecule was completely colorless and easily dispersible in different organic solvents (**Figure 2.1.B**).

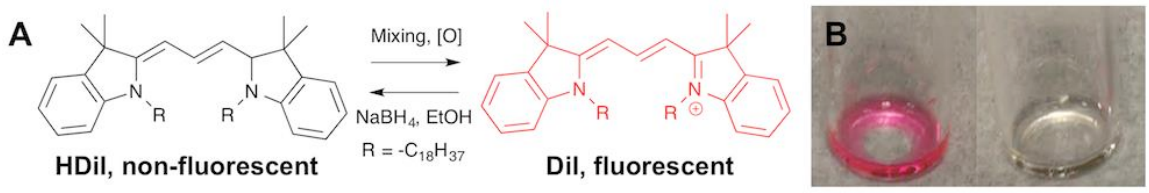

Figure 2.1. A: Scheme of reduction of DiI by NaBH4 and reactivation by oxidants. B: HDiI (right) and HDiI reactivated with 1 molar equivalent of p-fluoranil (left) in NEOBEE oil.

Next, the expected dye reactivation studies were tested in bulk. Initial studies showed that vegetable oils provided greater droplet stability than small molecule oils with less optical interference (data not shown). Thus, soybean oil and NEOBEE oil, a triglyceride extract of coconut oil, were examined as potential oil phases. For reagents, quinones were screened due to their oxidative reactivity and because many derivatives can be found as oil-soluble reagents. To screen reagents, equimolar amounts of HDiI and hydrophobic quinones were mixed in NEOBEE oil for 5 min, followed by recording of fluorescence emission spectra (λ_{exc} = 532 nm) (**Figure 2.2A**). Surprisingly, only some of the quinones reoxidized the HDiI effectively. Quinones with electron donating groups and additional ring structures such as 1,4-dihydroxyanthraquinone, 9,10-

phenanthrenequinone, and 3,3',5,5'-tetra-tert-butyldiphenoquinone yielded no appreciable change as compared to HDiI. All three benzoquinones with electron-withdrawing groups tested -- p-fluoranil (tetrafluoro-1,4-benzoquinone), p-chloranil, and DDQ -- yielded increase in signal, with p-fluoranil as the best, which also corresponded with the quinone possessing the highest oxidation potential[24]. Further optimization of p-fluoranil loading indicated that a 1:4 molar ratio of HDiI:p-fluoranil provided the greatest increase in fluorescence (51%); this formulation was utilized for all subsequent experiments (**Figure 2.2B**). To confirm that reaction proceeded as intended, ^{1}H-NMR spectra were obtained of commercial DiI alone, HDiI alone, and 1:4 HDiI:p-fluoranil. The spectra show that mixing HDiI and p-fluoranil results in a clear reappearance of the original peaks found in the commercial DiI sample, albeit with some broadening (**Figure 2.3**). The formation of DiI was confirmed by both ^{1}H-NMR spectra and ESI-MS (see Experimental Section). The incomplete recovery of fluorescence is thus most likely due to side bleaching reactions caused by the presence of strong oxidizers.

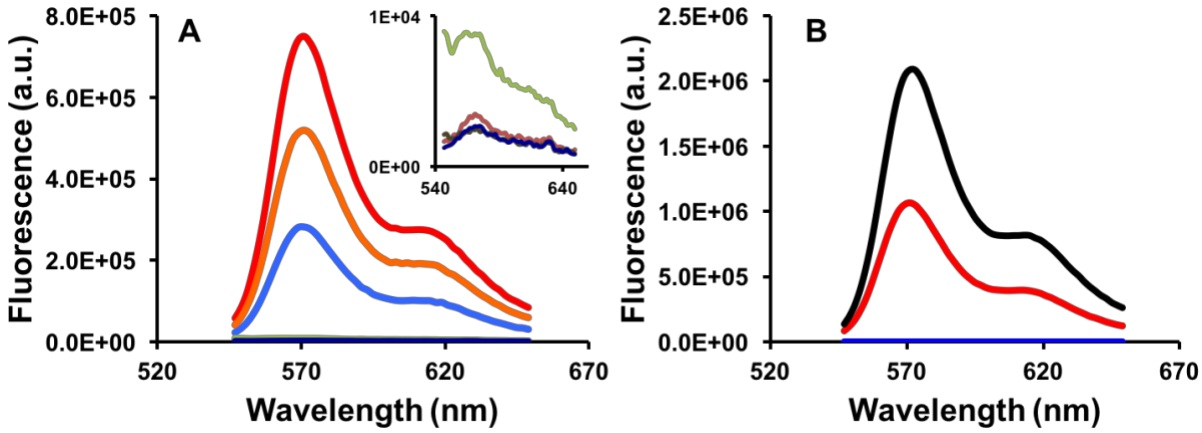

Figure 2.2. Fluorescence emission spectra (λ_{exc} = 532 nm) of mixtures of HDiI and various oxidants. **A**: Spectra of 1:1 mixtures of HDiI and p-fluoranil (red), p-chloranil (orange), DDQ (light blue), DHAQ (light green), 9,10-phenanthrenequinone (light red), DPQ (dark green), and

HDiI only (dark blue); the latter four are shown magnified in the *inset*. B: Commercial DiI only (black), 1:4 HDiI:p-fluoranil (dark red), and HDiI only (blue).

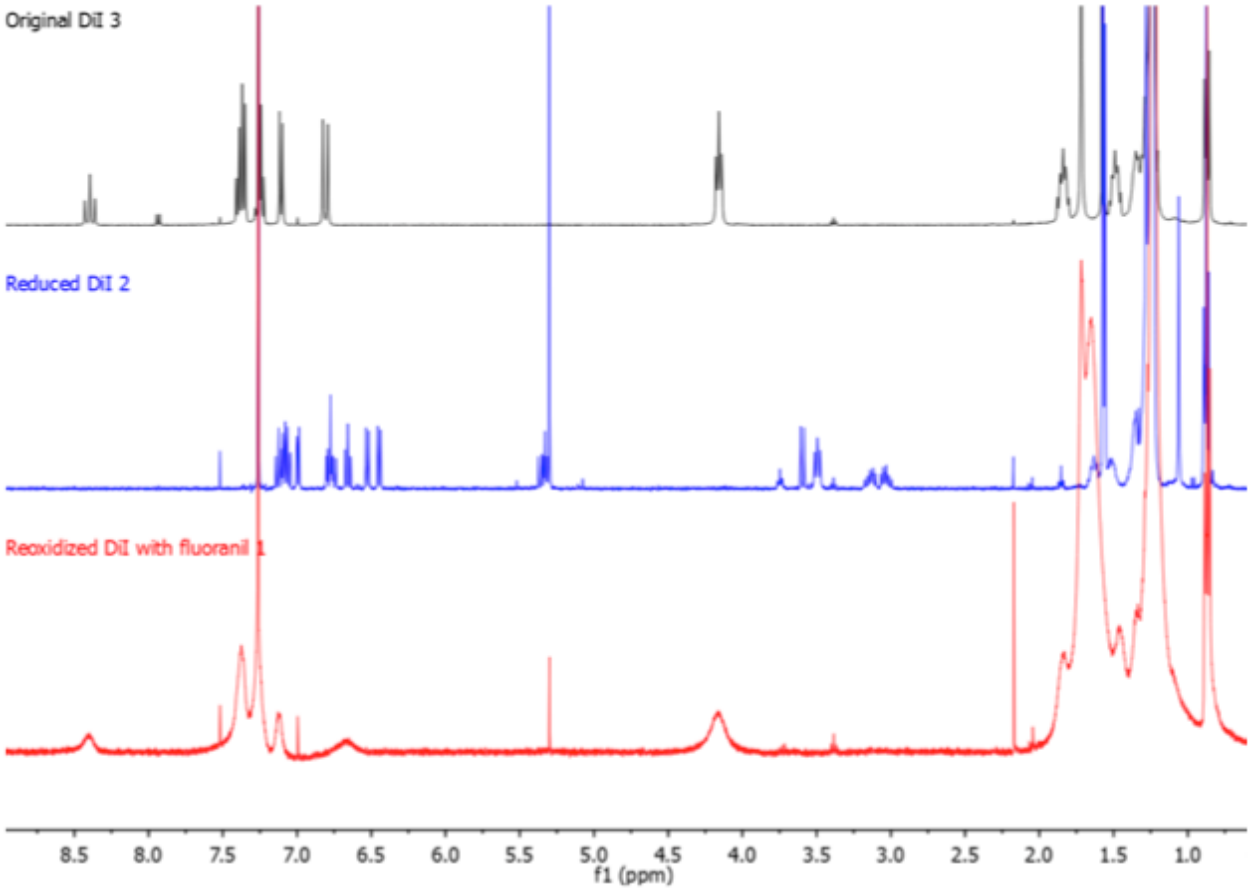

Figure 2.3. ^{1}H-NMR spectra ($CDCl_3$) of DiI (*black*), HDiI(*blue*), and HDiI mixed with 4 molar equivalents of p-fluoranil (*red*).

2.4.2. Nanodroplet Formulation and Aggregation. For proof-of-concept sensing experiments, nanodroplets containing either HDiI or p-fluoranil in NEOBEE oil were stabilized by a monolayer of lipid and polymer-lipids containing biotin (**Figure 2.4A**). Addition of streptavidin to these

biotin-containing droplets would cause the formation of aggregates and activation of fluorescence (**Figure 2.4B**). To make the droplets, a lipid film containing DPPC, DSPE-PEG2000, and DSPE-PEG2000-Biotin was first hydrated in Tris Buffered Saline (TBS) to form liposomes. To this, a 4 v/v% solution of NEOBEE oil containing either HDiI or p-fluoranil was added, and the mixture was probe sonicated to obtain an emulsion suspension, which was then centrifuged through a 0.45 μm filter to reduce size polydispersity. Measurements by Nanoparticle Tracking Analysis (NTA) determined both the concentration and the size (mean diameter 575.5 ± 203.5 nm) of the nanodroplets (**Figure 2.5**)[25]. To show that aggregation led to fluorescence activation, equal concentrations of droplets were mixed with varying concentrations of streptavidin and the resultant aggregates were imaged by fluorescence microscopy. For mixed droplets without streptavidin, a small amount of signal was observed by microscopy (**Figure 2.4C**). However, addition of 25 nM (**Figure 2.4D**) and 1 μM (**Figure 2.4E**) streptavidin caused the formation of aggregates that were clearly visible by fluorescence microscopy. Since increased fluorescence should primarily arise from mixing of reagents, one question is the mechanism by which the reagents encounter one another. While small amounts of droplet fusion are certainly possible, the appearance of some signal in the absence of streptavidin – and hence, aggregation – indicates that the internal phase may diffuse through one monolayer and into another droplet. Thus, while the probability of a molecule diffusing out of one droplet and into another is much higher when the droplets are aggregated, a small amount of reagent, probably p-fluoranil rather than HDiI, is likely able to diffuse through the aqueous media as well. Nevertheless, the fluorescent signal is clearly greater for aggregated droplets than unaggregated as a direct result of streptavidin addition.

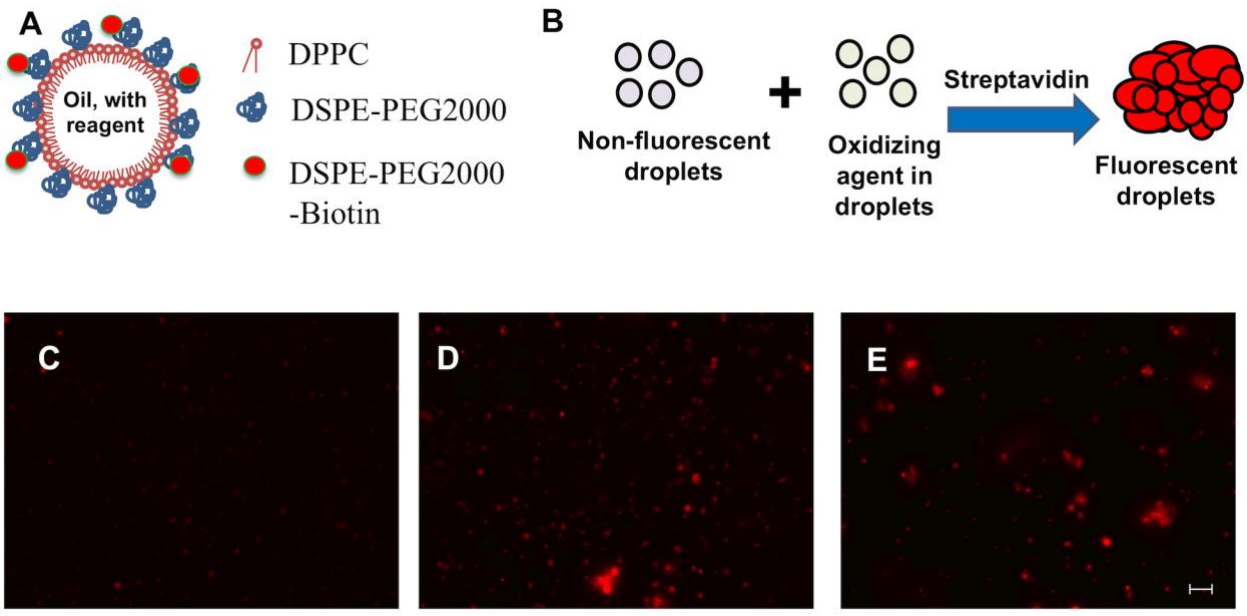

Figure 2.4. A: Schematic of droplet structure. B: Schematic of nanodroplet composition and aggregation scheme. C-E: False-colored fluorescence microscopy images of mixed HDiI droplets and p-fluoranil droplets with 0 (C), 25 nM (D), and 1 μM (E) streptavidin. Scale bar: 5 μm

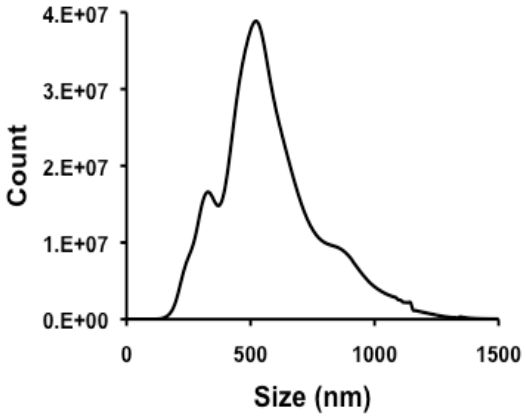

Figure 2.5. Size distribution of droplets containing NEOBEE oil as measured by NTA. Mean droplet diameter: 575.5 nm; SD = 203.5 nm.

2.4.3. Sensing of Streptavidin via Droplet Association. Studies were performed to illustrate the ability of this system to perform biosensing. One complication was that the nanodroplets scatter light, which interfered with bulk fluorescence measurements. However, a method that could specifically select fluorescent droplets would be able to overcome this limitation. The NTA instrument records video of particle suspensions, records Brownian motion of the particles, and calculates particle size via the Stokes-Einstein equation. By irradiating the particles at 532 nm and applying a red fluorescence emission filter, the NTA could specifically select for droplets that contained red fluorescence only, thereby reducing background from non-fluorescent droplets. No additional thresholding was necessary.

In a typical experiment, suspensions of HDiI droplets and p-fluoranil droplets were combined as above with a series of streptavidin concentrations from 100 fM-25 nM at 37^{o}C for 30 min. Droplets were then excited at 532 nm while monitoring their motion and fluorescence emission for 60 s, thus both recording droplet diffusivity and fluorescence intensity simultaneously. The emission of each fluorescent droplet was integrated over the 60 s of video acquisition (example stills in **Figure 2.6**). The resultant scatter-plots show that droplet samples containing streptavidin have larger sizes and fluorescence intensities than those without (**Figure 2.7A-B, Figure 2.8)**. To quantify the relative responses between the samples, the integration of intensities of all fluorescent droplets and aggregates detected by the NTA was plotted as a function of streptavidin concentration (**Figure 2.7C**). This method showed a clear differentiation between the integrated signals between the control sample and an analyte concentration as low as 100 fM. At this concentration and the others tested the p-value for a one-tailed t-test was < 0.05. Interestingly, the dynamic range of this study also has a theoretical upper limit as defined by the size of the resultant aggregates. As shown in our previous work with fluorocarbon droplets, above a certain streptavidin

concentration droplets tend to form higher order aggregates rather than smaller clusters, but their slow diffusion restricts the maximum detectable size to 2 μm[26].

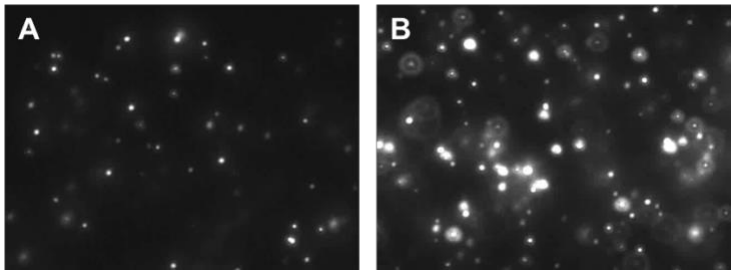

Figure 2.6. Representative frames of videos captured through a fluorescence filter under a 532 nm excitation laser, by the Malvern NanoSight LM10, for subsequent analysis by the NTA 3.0 software. Figures show fluorescence for biotinylated mixed HDiI droplets and p-Fluoranil droplets incubated without (**A**) and with (**B**) 1nM streptavidin.

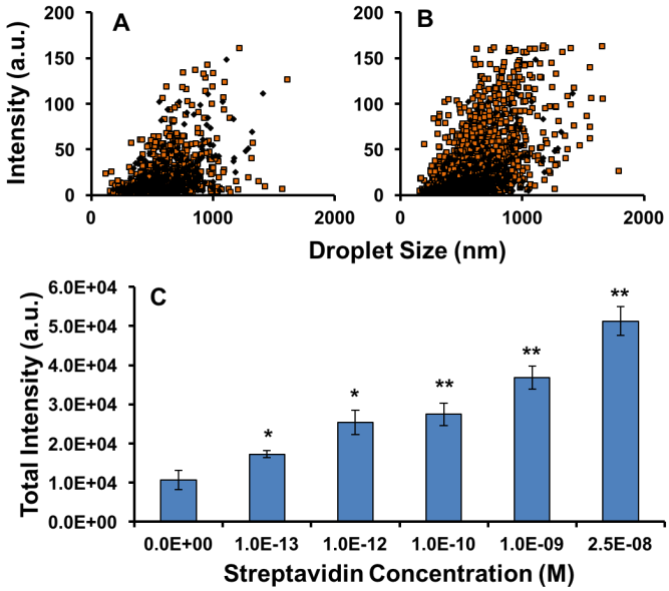

Figure 2.7. A-B: Representative NTA fluorescence scatter plots of biotinylated HDiI droplets and p-fluoranil droplets mixed without (black diamonds) or with (orange squares) a respective

concentration of streptavidin (**A**: 100 fM; **B**: 25 nM); **C**: Dose response of mixed HDiI droplets and p-fluoranil droplets as a function of streptavidin concentration. Integrated intensity is the summation of intensity of each detected droplet aggregate. Error bars represent standard deviation of at least three trials. *p<0.05, **p<0.005 as compared to sample without streptavidin.

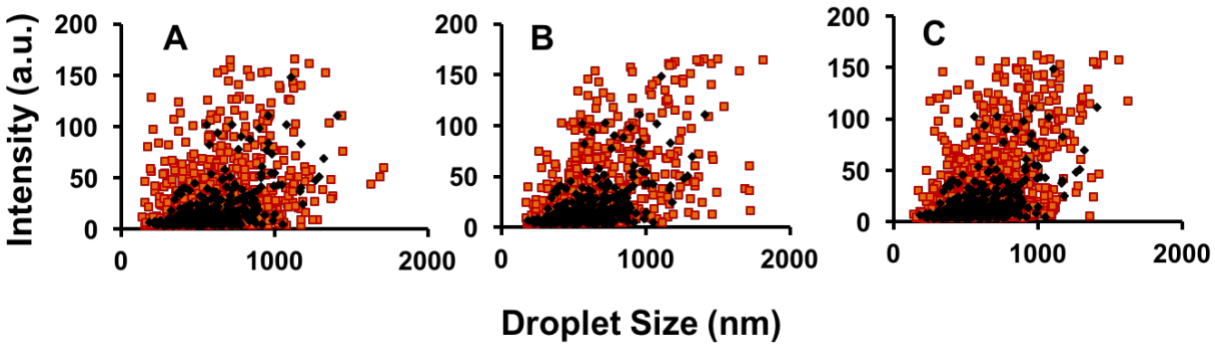

Figure 2.8. Representative NTA fluorescence scatter plots of biotinylated HDiI droplets and p-fluoranil droplets mixed without (black diamonds) or with (orange squares) a respective concentration of streptavidin (**A**: 1 pM; **B**: 100 pM; **C**: 1 nM)

As discussed above, the background signal in the absence of streptavidin was probably caused due to some amount of diffusion of the p-fluoranil first into the aqueous solution and then into a HDiI-loaded droplet. To measure the effect of this process on background signal generation, HDiI and p-fluoranil loaded droplets were incubated at 37°C and the resulting response was measured by NTA. As expected, simply mixing the droplets caused some increase in integrated signal over time, but the signal reached only to a level corresponding to close to 1 pM streptavidin even after 2 hrs of agitation (**Figure 2.9A**). Another potential complication was sensing capability in more complex media. HDiI and p-fluoranil loaded droplets were incubated with and without 1 nM streptavidin in either 50% Fetal Bovine Serum (FBS) and in 50% Sodium Citrate-stabilized bovine

plasma. Based on the response, streptavidin-mediated aggregation clearly occurred in both FBS and plasma (**Figure 2.9B**). Little change was observed for the samples without streptavidin, supporting the specificity of response and the stability of the HDiI to complex media. For samples with streptavidin, signal was overall less intense and more variable for serum and plasma than for buffer, which indicates that specificity of sensing is governed by the analyte capture agents (e.g. aptamers and antibodies) rather than the droplets themselves. For comparison, previous research in our labs showed that fluorocarbon droplets with similar lipid compositions showed little nonspecific activation by off-target analytes[26]. Most likely, the serum proteins bind nonspecifically to the lipid shell, reducing diffusion of p-fluoranil from the droplets. Another possibility is the consumption of p-fluoranil via side reaction with a serum protein, which has been observed previously[27,28]. Nevertheless, the presence of complex media only reduces overall signal by about 25%.

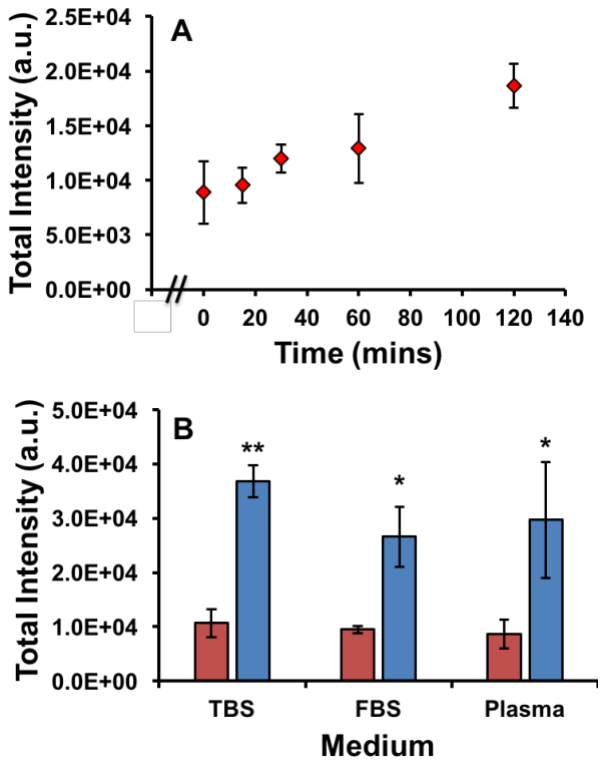

Figure 2.9. A: Time-dependent response of mixed biotinylated HDiI droplets and p-fluoranil droplets in the absence of streptavidin. **B**: Response of the mixed droplets without (*red*) or with (*blue*) 1 nM streptavidin in TBS, 50% FBS, or 50% Bovine Plasma. *p<0.05, **p<0.005 as compared to sample without streptavidin.

2.4.4. Aptamer-VEGF binding and Droplet Aggregation. To validate the nanodroplet sensors with a more biomedically relevant analyte, we next reformulated the droplets to sense for Vascular Endothelial Growth Factor A (VEGF). VEGF has been sensed previously using ELISA, microfluidic chips, and microarray techniques[29–32]. The crystal structure has shown that VEGF exists as an antiparallel homodimer, and thus containing two binding sites that will allow association of droplets on other side of the dimer[33]. While VEGF antibodies are commercially

available, we sought to decrease the distance between bound droplets by using VEGF aptamers, thereby improving content transfer[34,35]. The reported anti-VEGF aptamer was utilized here with the following modifications: (1) both 5'-CCC and GGG-3' were incorporated at the termini to stabilize the folded conformation for improved association[34,35], (2) an additional 5'-TTTT spacer to provide flexibility for binding to VEGF dimer, and (3) the 5' end was thiolated for conjugation (see Experimental for full sequence). The thiolated anti-VEGF aptamer was then reacted with DSPE-PEG2000-Maleimide in the presence of Tris(2-carboxyethyl)phosphine hydrochloride) (TCEP) to allow incorporation of the aptamer into the droplet monolayer as a conjugate (DSPE-PEG2000-Mal-Apt).

In-solution detection of VEGF dimer was performed analogously to the streptavidin sensing studies. Nanodroplets loaded with HDiI and p-fluoranil were formulated using a lipid-PEG stock solution, but with the DSPE-PEG2000-Mal-Apt in place of the DSPE-PEG2000-Biotin. Fluorescence microscopy images of these droplets without and with 100 nM VEGF are shown in **Figure 2.10A** and **Figure 2.10B** respectively. As with streptavidin, aggregation of droplets led to mixing of HDiI and p-fluoranil diffusion through the droplet monolayers, generating a fluorescence signal. In the absence of VEGF, apparent fluorescence was low by microscopy (**Figure 2.10A**). Next, HDiI and p-fluoranil droplets were incubated with varying concentrations of VEGF in TBS to determine a dose response trend. NTA was once again performed on the droplets under a 532 nm excitation laser through a fluorescence filter. A similar trend of integrated signal vs. analyte concentration was observed as for streptavidin (**Figure 2.10C**). The integrated signal leveled at higher concentrations, probably due to formation of larger aggregates and the limitation of NTA to detect aggregates greater than 2 μm in size as described above. Without VEGF there was more background signal than for streptavidin, possibly due to increased non-

specific aggregation caused by non-complementary association of aptamer strands. However, these results show that VEGF-165 homodimers can be detected by this technique down to 100 fM (~ 4 pg/mL), with the greatest dynamic range between 100 fM to 10 pM (~400 pg/mL). These levels correspond well with an ability to differentiate serum VEGF levels from normal baseline (150 pg/mL) to elevated levels associated with metastatic breast cancer (320 pg/mL)[32]. For comparison, commercial ELISA assays such as the Human VEGF Immunoassay (R&D Systems) are able to obtain greater difference in signal between these levels and with a linear signal-concentration dependence. However, the reported fluorogenic system is able to obtain results within 30 min as compared to >4 h for solid-phase ELISA assays such as these (R&D Systems). Interestingly, the detection limit for VEGF-165 was similar to that of streptavidin, even though the dissociation constants of VEGF-165/aptamer and streptavidin/biotin are quite different (~50 nM[34] and 10 fM, respectively). We attribute this finding to diffusion of p-fluoranil from the droplets, which generates background signal that reduces sensitivity for the streptavidin/biotin assay. Future studies will thus focus on designing other reactive pairs that will partition more effectively into the droplets with the aim of reducing background and improving limit of detection.

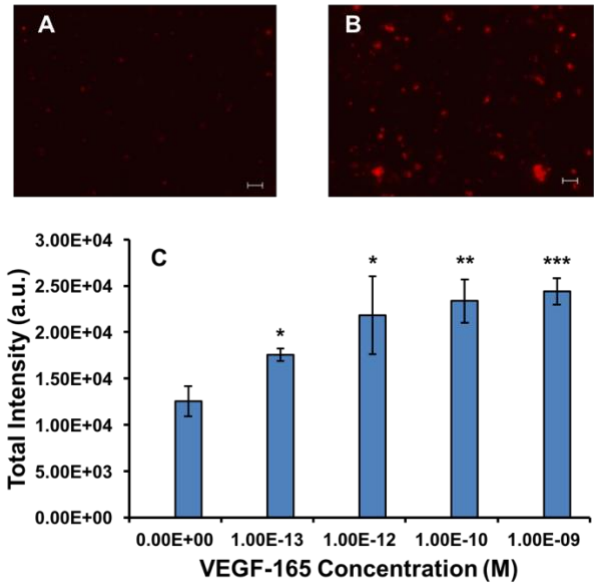

Figure 2.10. A-B: False-colored fluorescence microscopy images of anti-VEGF aptamer coated mixed HDiI droplets and p-fluoranil droplets incubated with 0 (A) and 100 nM (B) VEGF-165. Scale bar: 5 μm; **C**: Dose response of the mixed droplets as a function of VEGF-165 concentration. **P*<0.05, ***P*<0.005, ****P*<0.0005, Student's *t*-test compared to sample without VEGF.

2.5. Conclusion

In summary, a novel fluorogenic system was developed as an in-solution biosensor. Oil-soluble DiI, a hydrophobic cyanine derivative, was reduced into a non-fluorescent molecule. A series of quinones were found to be able to partially restore the reduced DiI to fluorescence. Biosensing was performed by placing HDiI and p-fluoranil in separate biotinylated droplets, followed by addition of varying concentrations of streptavidin. Droplet aggregates were found to become fluorescent as observed by microscopy. By counting the total fluorescence of the droplets by Nanoparticle Tracking Analysis, streptavidin could be sensed down to 100 fM. The background oxidation of the HDiI was found to be slow enough to allow detection in 30 min, and the signal

was found to activation with about 25% less activity in serum and plasma. Finally, this same system was able to detect Vascular Endothelial Growth Factor A down to 100 fM using aptamer-analyte interactions. In future studies, the work described here will be expanded to sense for more complex analytes via antibody interactions.

2.6. Acknowledgment

This work was supported by NIH grants DP2EB020401, R21EB018034, and R00CA153935. The authors thank Dr. Omer Yehekzeli and Prof. Jennifer Cha for helpful discussions and Mr. Diego Chimendes for help with reagent synthesis. The authors would also like to thank the Central Analytical Lab at CU Boulder for their help with mass spectroscopy, which was supported by NIH grant S10RR026641.

2.7. Abbreviations

DiI: 1,1'-dioctadecyl-3,3,3'3'-tetramethylindocarbocyanine perchlorate; HDiI: DiI reduced with $NaBH_4$; p-Fluoranil: tetrafluoro-1,4-benzoquinone; p-Chloranil: tetrachloro-1,4-benzoquinone; DDQ: 2,3-Dichloro-5,6-dicyano-1,4-benzoquinone; DHAQ: 1,4-Dihydroxyanthraquinone; DPPC: 1,2-dipalmitoyl-sn-glycero-3-phosphocholine; DPQ: 3,3',5,5'-tetra-tert-butyldiphenoquinone; DSPE-PEG2000:1,2-distearoyl-sn-glycero-3-phosphoethanolamine-N-[amino(polyethylene glycol)-2000]; DSPE-PEG2000-Biotin:1,2-distearoyl-sn-glycero-3-phosphoethanolamine-N-[biotinyl(polyethylene glycol)-2000].

2.8. References

1. Weissleder, R., Tung, C.-H., Mahmood, U., and Jr, A.B. (1999) In vivo imaging of tumors with protease-activated near-infrared fluorescent probes. *Nat. Biotechnol.*, **17** (4), 375–378.

2. Jiang, T., Olson, E.S., Nguyen, Q.T., Roy, M., Jennings, P.A., and Tsien, R.Y. (2004) Tumor imaging by means of proteolytic activation of cell-penetrating peptides. *Proc. Natl. Acad. Sci.*, **101** (51), 17867–17872.

3. Santangelo, P.J., Nix, B., Tsourkas, A., and Bao, G. (2004) Dual FRET molecular beacons for mRNA detection in living cells. *Nucleic Acids Res.*, **32** (6), e57–e57.

4. Li, J.J., Chu, Y., Lee, B.Y.-H., and Xie, X.S. (2008) Enzymatic signal amplification of molecular beacons for sensitive DNA detection. *Nucleic Acids Res.*, **36** (6), e36–e36.

5. Tyagi, S., and Kramer, F.R. (1996) Molecular Beacons: Probes that Fluoresce upon Hybridization. *Nat. Biotechnol.*, **14** (3), 303–308.

6. Elghanian, R., Storhoff, J.J., Mucic, R.C., Letsinger, R.L., and Mirkin, C.A. (1997) Selective Colorimetric Detection of Polynucleotides Based on the Distance-Dependent Optical Properties of Gold Nanoparticles. *Science*, **277** (5329), 1078–1081.

7. Min, C., Shao, H., Liong, M., Yoon, T.-J., Weissleder, R., and Lee, H. (2012) Mechanism of Magnetic Relaxation Switching Sensing. *ACS Nano*, **6** (8), 6821–6828.

8. Nam, J.-M., Thaxton, C.S., and Mirkin, C.A. (2003) Nanoparticle-Based Bio-Bar Codes for the Ultrasensitive Detection of Proteins. *Science*, **301** (5641), 1884–1886.

9. Lee, J.H., Domaille, D.W., and Cha, J.N. (2012) Amplified Protein Detection and Identification through DNA-Conjugated M13 Bacteriophage. *ACS Nano*, **6** (6), 5621–5626.

10. Hamaguchi, N., Ellington, A., and Stanton, M. (2001) Aptamer Beacons for the Direct Detection of Proteins. *Anal. Biochem.*, **294** (2), 126–131.

11. Wang, K., Tang, Z., Yang, C.J., Kim, Y., Fang, X., Li, W., Wu, Y., Medley, C.D., Cao, Z., Li, J., Colon, P., Lin, H., and Tan, W. (2009) Molecular Engineering of DNA: Molecular Beacons. *Angew. Chem. Int. Ed.*, **48** (5), 856–870.

12. Chen, A.K., Behlke, M.A., and Tsourkas, A. (2007) Avoiding false-positive signals with nuclease-vulnerable molecular beacons in single living cells. *Nucleic Acids Res.*, **35** (16), e105–e105.

13. Mohan, P., Noonan, P.S., Nakatsuka, M.A., and Goodwin, A.P. (2014) On-Demand Droplet Fusion: A Strategy for Stimulus-Responsive Biosensing in Solution. *Langmuir*, **30** (41), 12321–12327.

14. Noonan, P.S., Mohan, P., Goodwin, A.P., and Schwartz, D.K. (2014) DNA Hybridization-Mediated Liposome Fusion at the Aqueous Liquid Crystal Interface. *Adv. Funct. Mater.*, **24** (21), 3206–3212.

15. Wang, C.-H., Kang, S.-T., Lee, Y.-H., Luo, Y.-L., Huang, Y.-F., and Yeh, C.-K. (2012) Aptamer-conjugated and drug-loaded acoustic droplets for ultrasound theranosis. *Biomaterials*, **33** (6), 1939–1947.

16. Miller, E.W., Tulyathan, O., Isacoff, E.Y., and Chang, C.J. (2007) Molecular imaging of hydrogen peroxide produced for cell signaling. *Nat. Chem. Biol.*, **3** (5), 263–267.

17. Miller, E.W., Albers, A.E., Pralle, A., Isacoff, E.Y., and Chang, C.J. (2005) Boronate-Based Fluorescent Probes for Imaging Cellular Hydrogen Peroxide. *J. Am. Chem. Soc.*, **127** (47), 16652–16659.

18. Terai, T., and Nagano, T. (2008) Fluorescent probes for bioimaging applications. *Curr. Opin. Chem. Biol.*, **12** (5), 515–521.

19. Setsukinai, K., Urano, Y., Kakinuma, K., Majima, H.J., and Nagano, T. (2003) Development of Novel Fluorescence Probes That Can Reliably Detect Reactive Oxygen Species and Distinguish Specific Species. *J. Biol. Chem.*, **278** (5), 3170–3175.

20. Fitch, K.R., and Goodwin, A.P. (2014) Mechanochemical Reaction Cascade for Sensitive Detection of Covalent Bond Breakage in Hydrogels. *Chem. Mater.*, **26** (23), 6771–6776.
21. Kundu, K., Knight, S.F., Willett, N., Lee, S., Taylor, W.R., and Murthy, N. (2009) Hydrocyanines: A Class of Fluorescent Sensors That Can Image Reactive Oxygen Species in Cell Culture, Tissue, and In Vivo. *Angew. Chem. Int. Ed.*, **48** (2), 299–303.

22. Kundu, K., Knight, S.F., Lee, S., Taylor, W.R., and Murthy, N. (2010) A Significant Improvement of the Efficacy of Radical Oxidant Probes by the Kinetic Isotope Effect. *Angew. Chem. Int. Ed.*, **49** (35), 6134–6138.

23. Oushiki, D., Kojima, H., Terai, T., Arita, M., Hanaoka, K., Urano, Y., and Nagano, T. (2010) Development and Application of a Near-Infrared Fluorescence Probe for Oxidative Stress Based on Differential Reactivity of Linked Cyanine Dyes. *J. Am. Chem. Soc.*, **132** (8), 2795–2801.

24. Zhu, X.-Q., Wang, C.-H., and Liang, H. (2010) Scales of Oxidation Potentials, pKa, and BDE of Various Hydroquinones and Catechols in DMSO. *J. Org. Chem.*, **75** (21), 7240–7257.
25. Filipe, V., Hawe, A., and Jiskoot, W. (2010) Critical Evaluation of Nanoparticle Tracking Analysis (NTA) by NanoSight for the Measurement of Nanoparticles and Protein Aggregates. *Pharm. Res. N. Y.*, **27** (5), 796–810.

26. Chattaraj, R., Mohan, P., Besmer, J.D., and Goodwin, A.P. (2015) Selective Vaporization of Superheated Nanodroplets for Rapid, Sensitive, Acoustic Biosensing. *Adv. Healthc. Mater.*, **4** (12), 1790–1795.

27. Mason, H.S. (1955) Reactions between Quinones and Proteins. *Nature*, **175** (4461), 771–772.

28. Li, W.-W., Heinze, J., and Haehnel, W. (2005) Site-Specific Binding of Quinones to Proteins through Thiol Addition and Addition−Elimination Reactions. *J. Am. Chem. Soc.*, **127** (17), 6140–6141.

29. Freeman, R., Girsh, J., Fang-ju Jou, A., Ho, J.A., Hug, T., Dernedde, J., and Willner, I. (2012) Optical Aptasensors for the Analysis of the Vascular Endothelial Growth Factor (VEGF). *Anal. Chem.*, **84** (14), 6192–6198.

30. Zhao, Z., Al-Ameen, M.A., Duan, K., Ghosh, G., and Fujiou Lo, J. (2015) On-chip porous microgel generation for microfluidic enhanced VEGF detection. *Biosens. Bioelectron.*, **74**, 305–312.

31. Jin Lee, H., W. Wark, A., and M. Corn, R. (2008) Microarray methods for protein biomarker detection. *Analyst*, **133** (8), 975–983.

32. Xu, X., Wang, B., Ye, C., Yao, C., Lin, Y., Huang, X., Zhang, Y., and Wang, S. (2008) Overexpression of macrophage migration inhibitory factor induces angiogenesis in human breast cancer. *Cancer Lett.*, **261** (2), 147–157.

33. Muller, Y.A., Li, B., Christinger, H.W., Wells, J.A., Cunningham, B.C., and Vos, A.M. de (1997) Vascular endothelial growth factor: Crystal structure and functional mapping of the kinase domain receptor binding site. *Proc. Natl. Acad. Sci.*, **94** (14), 7192–7197.

34. Potty, A.S.R., Kourentzi, K., Fang, H., Jackson, G.W., Zhang, X., Legge, G.B., and Willson, R.C. (2009) Biophysical characterization of DNA aptamer interactions with vascular endothelial growth factor. *Biopolymers*, **91** (2), 145–156.

35. Zhang, X., and Yadavalli, V.K. (2011) Surface immobilization of DNA aptamers for biosensing and protein interaction analysis. *Biosens. Bioelectron.*, **26** (7), 3142–3147.

Chapter 3. Lowering the Acoustic Droplet Vaporization Threshold of Perfluorohexane Nanodroplets via Aggregation and Non-Specific Protein Interactions: Applications in Biomarker Sensing

A similar version of this chapter first appeared in the article: Chattaraj, R., Mohan, P., Besmer, J.D., and Goodwin, A.P. (2015) Selective Vaporization of Superheated Nanodroplets for Rapid, Sensitive, Acoustic Biosensing. Adv. Healthc. Mater., 4 (12), 1790–1795.

3.1. Abstract

Perfluorocarbon nanodroplets exhibit promise as sensitive acoustic biosensors. Aggregation of biotin-decorated lipid-shelled droplets with a volatile liquid perfluorohexane core by streptavidin greatly increased the yield of bubbles formed by ultrasound-induced vaporization. Streptavidin and VEGF-165 were sensed down to 100 fM-1pM in saline, with differentiable signal appearing in as little as two minutes, using a scalable assay without washing, processing, or development steps. Sensitivity was relatively lower in serum due to non-specific protein adsorption. Furthermore, it was found that the acoustic droplet vaporization threshold for perfluorohexane droplets is markedly lower in physiological media than in saline.

3.2. Introduction

The development of new materials that can sense or quantify levels of biomarkers within specific regions of interest in vivo would represent a substantial advance in applications of personalized medicine such as monitoring the aggressiveness of solid tumors or growth of arterial plaque. While many contrast agents can be functionalized with ligands that bind membrane-bound targets, fewer

agents are able to sense soluble biomarkers such as Prostate Specific Antigen or Vascular Endothelial Growth Factor. Some profluorophores have been designed to react with endogenous enzymes or reactive oxygen species to induce a chemical or conformational change that increases photoluminescence[1–7]. Other examples include iron oxide nanoparticles that change their magnetic relaxivity upon self-assembly, which can be used for both in vivo imaging and in vitro biosensing[8–10]. In each of these cases, the modest difference between signal generated by activated contrast agents and background limits their ability to sense small concentrations of nonreactive or enzymatic biomarkers.

This work instead utilizes the specific acoustic signature of stable gas bodies in aqueous media that allows microbubbles to act as extremely potent contrast agents for ultrasound imaging. While sound is scattered elastically at the interface of most materials, a gas bubble in resonance with an ultrasound wave will undergo nonlinear expansion and contraction to generate harmonic and subharmonic frequencies[11,12]. Specific ultrasound imaging pulse programs such as cadence contrast pulse sequencing (CPS, Siemens) have been designed to accentuate nonlinear signal while essentially removing elastic scatter[13], resulting in microbubble detection limits of 10 aM[14] or less[15] with spatial resolution of ~0.1-1 mm. This property has led to development of polymer and lipid-stabilized microbubbles as ultrasound contrast agents for intravascular imaging[16–19]. Since size oscillations by the bubble are crucial for generating the highly-specific nonlinear echoes[12], biosensing capabilities can be conferred onto a bubble by tuning its compressibility in response to challenge with a biomolecular analyte. In previous research, for example, we designed microbubbles that could change the mechanical properties of their encapsulating shell, which allowed sensing of thrombin in the vicinity of acute blood clots[14,20–22]. Other examples include

use of bubbles as labels for surface-mediated assays, incorporation of alkaline phosphatase and lysozyme into nanoparticle-shelled bubbles, and labeling of stem cells or bacteria[23–26].

Thus, an even greater change in ultrasound contrast may be obtained by converting an incompressible liquid droplet into a compressible microbubble. For this reason, "phase-shift emulsions," or superheated liquid nanodroplets that can be converted into gas bodies in vivo, represent a potentially more powerful development in ultrasound contrast technology[27,28]. Prior to vaporization, liquid nanodroplets exhibit far greater stability in vivo than bubbles and can be formulated down to less than 400 nm in diameter for improved extravasation into tissue. While in their liquid form droplets possess poor acoustic contrast properties owing to their incompressibility, droplets with an internal phase of sufficiently high vapor pressure may be vaporized in situ using High Intensity Focused Ultrasound (HIFU), resulting in the generation of high-contrast microbubbles in situ[29–34]. The effect of HIFU parameters and nanodroplet properties on acoustic nanodroplet vaporization has been the subject of several studies, and generally as mean nanodroplet size increases the peak HIFU pressure required to vaporize the nanodroplets decreases[28,35–37]. Thus, we hypothesized that aggregating nanodroplets through biomolecular interactions might result in a decrease in HIFU vaporization threshold as well, thereby enhancing signal specifically after interaction with a biomarker of interest (**Figure 3.1a**).

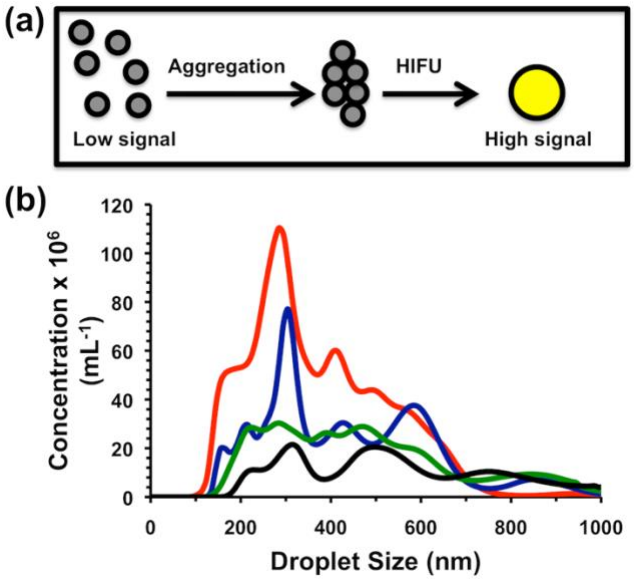

Figure 3.1. (a) Schematic of low-contrast droplet aggregation allowing vaporization to high contrast bubbles. (b) Size histogram of droplet diameter as measured by Nanoparticle Tracking Analysis. Shown are as-made (black), 200*g*-fractionated (green), 300g-fractionated (blue), and 400g-fractionated (red) droplets.

3.3. Experimental Section

3.3.1. Formulation of Nanodroplets. Prior to droplet formulation, Tris-buffered saline (TBS) was prepared to a final concentration of 10 nM Tris base (Fisher Scientific) and 100 mM NaCl (Fisher Scientific), adjusted to a pH of 8.0 with dilute HCl. A stock suspension of hydrated DPPC (Avanti Polar Lipids, Inc.) was prepared as described previously in **Chapter 2.3.5**[38]. The stock DPPC suspension was mixed with DSPE-PEG2000 (Avanti Polar Lipids, Inc.) and DSPE-PEG2000-Biotin (Avanti Polar Lipids, Inc.) to make a final concentration of 1.3 mM/40 µM/15 µM, respectively, in TBS, and stirred at 75^0C for 30 min. The lipid-PEG-biotin suspension was then allowed to cool to RT. 40 µL of perfluorohexane (PFH) (Strem Chemicals) was added per mL of the lipid suspension using pre-cooled pipette tips to make a 4 v/v % mixture. To obtain droplets,

the mixture was probe sonicated (Branson SLPe), 1 mL at a time, with two 1 min cycles of 1s on-9s off bursts at 70% amplitude while immersing the suspension in an ice bath. To formulate anti-VEGF aptamer coated droplets, a similar procedure was followed with specific aptamers instead of biotin (see **Chapter 2.3.5**). Droplets with Neobee oil (Spectrum Chemical Mfg. Corp.) as the internal phase instead of PFH were formulated following the same procedure described above, without the requirement of having to cool the pipette tips or immersion in an ice-bath.

3.3.2. Size Separation of Nanodroplets. To fractionate the droplets to a specific size range, the emulsions were first centrifuged at a lower speed (400, 300, 200 *g*, or not at all, as indicated in the text) for 1.5 min. The supernatant was then recovered and further centrifuged at 1000 *g* for 2.5 min to pellet the droplets. Each pellet was resuspended in an amount of TBS required to obtain an optimal droplet concentration for NTA analysis; for instance, pellets from 400 *g* were resuspended in 40 µL TBS per mL pelleted while 0 *g* pellets were resuspended in 500 µL TBS per mL pelleted. The concentration and size distribution of these droplets were measured via Nanoparticle Tracking Analysis using a NanoSight LM10 setup (Malvern) (**Table 3.1**). Following initial experiments optimizing centrifugation speed, all subsequent droplet samples were prepared using the 400 *g*-then-1000 *g* double centrifugation procedure. Droplets containing Neobee oil were centrifuged at 1600 *g* for 1 min, and the supernatant was then centrifuged in a 0.45 µm centrifugal filter tube at 12,000 *g* for 4 min. The pellet of the Neobee oil droplets was resuspended in TBS to obtain a droplet suspension.

3.3.3. Aggregation and Imaging of Nanodroplets: Resuspended PFH droplets were diluted, as necessary, in TBS buffer to a final concentration of $5x10^{12}$ droplets L^{-1} (NTA), followed by

addition of streptavidin (Pierce) to the concentration indicated in the text. The mixture was then incubated in a glass vial at 4-8 ^{0}C for 30-40 min. Bright-field images were taken of both aggregated and non-aggregated droplets using a microscope (Zeiss). Images were processed by MATLAB (Mathworks, Inc.), using code developed in our labs.

3.3.4. Ultrasound Contrast Imaging and Analysis. Prior to imaging studies, a spherically focused, single-element, High Intensity Focused Ultrasound transducer (Sonic Concepts H101, 64.0 mm Active Diameter x 63.2 mm Radius of Curvature) was equipped with a coupling cone (Sonic Concepts C101) filled with degassed and deionized water; the transducer and core were submerged in a water tank. The HIFU transducer was connected to a 30 MHz Function/Arbitrary Waveform Generator (Agilent Technologies) via an AG Series Amplifier (T&C Power Conversion, Inc.), the latter operating at 100% output throughout the study, the peak pressure of which was measured to be 9.8 MPa via needle hydrophone calibration (Onda Corp.).

In a typical experiment, PFH nanodroplets were diluted to a concentration of approximately $5x10^{12}$ droplets L^{-1} in TBS to a final volume of 1 mL per sample. The sample was mixed with streptavidin (or VEGF-165; see **Chapter 2.3.6 and 2.4.4** for details) at the indicated concentration and immediately transferred to the bulb of a plastic transfer pipette. The bulb was positioned on top of the coupling cone to ensure proper HIFU focusing into the center of the sample. A 4V1 (Acuson) transducer was aligned to acquire horizontal cross-sectional images of the sample while minimizing direct exposure of the transducer to HIFU pulses. For each sample, a low intensity clearing pulse was first applied by the 4V1 to destroy the few isolated microbubbles formed during incubation. Next, HIFU was applied with the following function generator settings: 1 Vpp, 1.1 MHz center frequency, 0.1 s pulse interval (burst period), and a number of cycles indicated in the

main text; after initial optimization studies, the cycle number was set to 12. Real-time videos were then recorded by a Siemens Acuson Sequoia™ C512 scanner operating in cadence pulse sequencing (CPS) mode at 1.5 MHz and a mechanical index (MI) of 0.19; a total HIFU application time of about 15 s was used for each sample. For data analysis, the recorded videos were deconstructed into separate binary images, with each frame corresponding to 1 s. The mean pixel intensity within the bulb phantom was measured using ImageJ (NIH). To achieve this, a grayscale pixel threshold level of 23±1 % – in a range of 0 (white) to 255 (black) – was applied to the region of interest inside the phantom, and the intensity was measured as the difference in contrast between the signal and the white background (**Figure 3.2).** The signal obtained prior to HIFU pulsing was negligible. The total mean intensity generated from each video, calculated as the sum of the intensities from each 1s frame over 15 s of HIFU application, was depicted as a representation of the strength of the signal obtained from the corresponding sample.

For specificity studies, the following biomolecules were utilized: α-amylase from human saliva (Sigma-Aldrich), bovine serum albumin (US Biological), lysozyme from egg white (Fisher Scientific), mouse anti-HSA (Pierce), and thrombin aptamer (Integrated DNA Technologies). In order to study the affinity of a biotinylated droplet to its specific analyte, a fixed concentration (1 nM) of each analyte was incubated 30-40 min with 400 *g* fractionated droplets prepared as described above. The acoustic response of the droplets for each sample was measured as described above. In a separate competition experiment, the same concentration of analyte was co-incubated with 1 nM streptavidin for 30-40 min, and acoustic response was measured as described.

For the time-resolved imaging experiments, the signal was recorded first, as indicated above, for non-aggregated droplets. Streptavidin of appropriate concentration was then added to the plastic

bulb containing the sample, and the signal was recorded again after 2, 5, 8, and 10 min, while mildly and intermittently shaking the sample between readings.

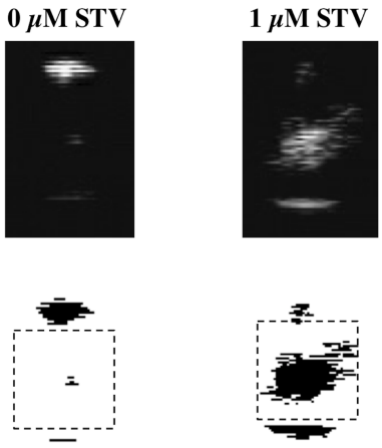

Figure 3.2: Examples of image processing using ImageJ. Top: still image from video file. Bottom: image after ImageJ processing; dashed rectangle indicates ROI.

3.4. Results and Discussion

3.4.1. Nanodroplet Formulation and Size Separation. Because these nanodroplets were intended to sense small concentrations of analyte, initial studies focused on reducing background signal by non-aggregated nanodroplets. To prepare the nanodroplets, a lipid film consisting of DPPC, DSPE-PEG2000, and DSPE-PEG2000-biotin was reconstituted in tris-buffered saline (TBS) to form liposomes. The liposomes were mixed at 4 v/v% perfluorocarbon and probe sonicated to form the droplets. Anticipated sources of background signal would be from either (a) nanodroplets of insufficient stability that would vaporize in a sample holder, or (b) nanodroplets of size large enough to be vaporized prior to aggregation. For example, although perfluoropentane (PFP, $T_{bp} \sim 29^{o}C$) is commonly used as a nanodroplet internal phase, the nanodroplets tended to form bubbles on the side of sample holders by eye, which increased background signal.

Perfluorohexane (PFH, T_{bp} ~ 56°C) instead gave nanodroplets that were stable over the course of the experiments. To reduce the size dispersity of the nanodroplets, the as-made suspension was subjected to various centrifuge speeds from 200*g* to 400*g* to pellet and remove the largest fraction of nanodroplets, followed by characterization of the supernatants by Nanoparticle Tracking Analysis (Malvern)[39]. Centrifugation of the as-made droplets at 400*g* gave the best reduction in mean diameter, from 609 nm to 368 nm (**Table 3.1**). Notably, the concentration of nanodroplets >800 nm in diameter were removed from the suspension almost entirely (**Figure 3.1b**).

Centrifuge fractionation speed (x *g*)	Mean droplet size (nm)	Approximate droplet concentration (mL^{-1})
400	367.6±2	$2.8x10^{11}$
300	435.3±20	$3.5x10^{11}$
200	485.6±20	$6.0x10^{11}$
0	609.1±8	$12.8x10^{11}$

Table 3.1. Mean size and droplet stock concentration as measured by Nanoparticle Tracking Analysis vs. droplet centrifuge fractionation speed.

3.4.2. Aggregation and Ultrasound Response of Nanodroplets. The ultrasound response of the nanodroplets was measured through continuous scanning at 1.5 MHz in CPS mode to highlight nonlinear, bubble-specific response[13]. Samples were placed in a plastic tube and submerged in a water tank containing a phased array scanning probe; movies were recorded and the integrated brightness in the sample was measured as captured signal (**Figure 3.3a, Figure 3.4**). Prior to exposure to HIFU, the sample was essentially dark within the walls of the tube. A HIFU transducer was aligned so that pulses would be focused into the center of the sample. Nanodroplets containing either 1 μM streptavidin or plain TBS buffer were subjected to different HIFU conditions in which a pulse packet of several sine waves was administered at a rate of 10 Hz. Non-aggregated nanodroplets showed little signal as expected, but after adding 1 μM streptavidin, administration of HIFU caused bright spots to appear in the image as a direct result of the vaporization (**Figure 3.3b**). While unfractionated droplets (0*g*) with 1 μM streptavidin exhibited a strong signal, the signal was also prominent with streptavidin as well; thus these samples only exhibited about a 2-fold enhancement (**Figure 3.3c**). By comparison, nanodroplets fractionated at 400*g* exhibited lower signal than unfractionated droplets; this decrease in signal may be explained by the disappearance of droplets greater than 800 nm, which are expected to provide a greater overall signal. However, the background signal dropped dramatically, producing a streptavidin-induced signal enhancement of about 77, and thus nanodroplets that had been fractionated at 400*g* were utilized for further experiments. As a control, nanodroplets with the same exterior composition but an interior phase of Neobee oil were subjected to the same conditions but showed no change in signal over baseline (**Figure 3.5**). Interestingly, the number of sine waves in each pulse packet had a profound effect on the vaporization of the nanodroplets. For non-aggregated nanodroplets, increasing the number of sine waves per pulse increased the output signal, though only slightly.

For streptavidin-aggregated nanodroplets, a large difference in signal was observed between 10 cycles and 12 cycles, with a gradual decrease thereafter (**Figure 3.3d**). While we do not know why 12 cycles was specifically required for vaporization of PFH, additional HIFU pulses should destroy the bubbles that have been formed, leading to decreased signal.

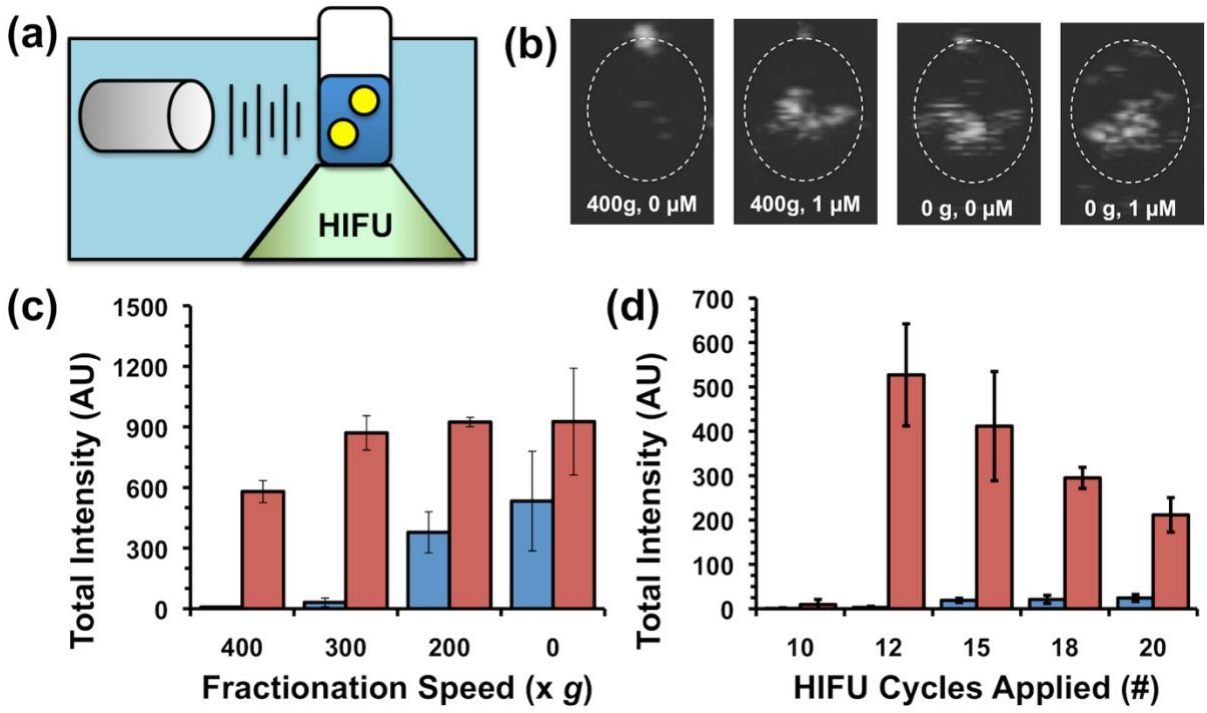

Figure 3.3. (a) Schematic of setup for measuring ultrasound signal from HIFU-vaporized droplets. (b) Representative still images taken from movies acquired during HIFU pulsing of droplet samples. From left to right: 400*g*-fractionated droplets with no streptavidin, 400*g*-fractionated droplets with 1 µM streptavidin, as-made droplets with no streptavidin, and as-made droplets with 1 µM streptavidin. (c,d) Integrated brightness from HIFU pulsing of droplet samples. Blue bars (left) indicate without streptavidin, red bars (right) indicate 1 µM streptavidin. Error bars = 1 SD; studies were run in at least triplicate. (c) Integrated brightness as function of fractionation conditions. (d) Integrated brightness as function of number of sine waves per pulse packet.

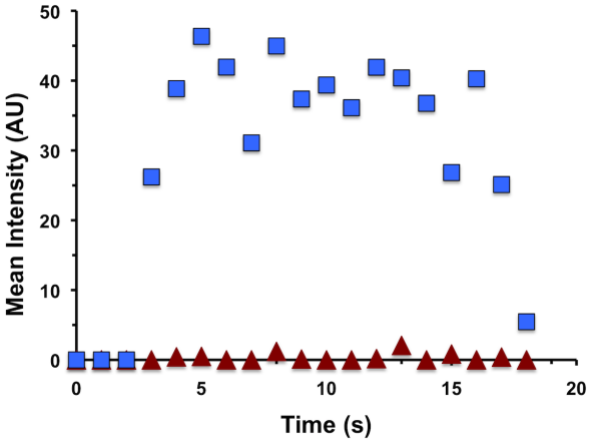

Figure 3.4. Mean brightness vs. time from HIFU pulsing of droplets as function of time. HIFU is pulsed from 3-17 s. Blue squares indicate 1 μM streptavidin loading; red triangles indicate no streptavidin loading.

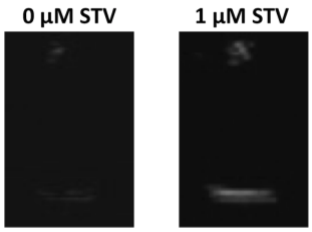

Figure 3.5. Still images of Neobee oil droplets after HIFU pulsing with either no or 1 μM streptavidin.

3.4.2.1. Dose response of aggregated droplets. Next, 400*g*-fractionated PFH biotinylated nanodroplets were incubated with different concentrations of streptavidin from 1 μM down to 100 fM, as well as no streptavidin (**Figure 3.6a**). The signal response curve showed three major regions of response. At the highest streptavidin concentrations, from 1 μM to 100 nM, the signal appeared to be saturated. Bright field microscopy studies comparing 0 and 1 μM streptavidin concentrations

showed the appearance of larger, higher order aggregates that most likely served as nucleation sites for the appearance of signal. Since these droplets would most likely vaporize together to produce very large bubbles, the resultant signal at these streptavidin concentrations was quite high. Concentrations in the range of 100 nM to 1 nM appear to correspond to the center of the S-curve. Using the measured nanodroplet concentration of $5x10^{12}$ L^{-1} (NTA), the mean radius of the droplets as 200 nm, the area per lipid as 0.5 nm^2, and the ratio of biotin to lipid as 1:100, each droplet has an average of about 10,000 biotin molecules per droplet and the total biotin concentration is approximately 100 nM. Thus the greatest difference in signal was observed at concentrations near and below 100 nM, which corresponded to the greatest difference in aggregate structure as a function of streptavidin concentration. Finally, at concentrations between 1 nM and 100 fM, the number of biotin molecules exceeds the number of streptavidin molecules, and so fewer numbers of smaller order aggregates (dimers or trimers) are formed. This reasoning would explain the observation that the two lowest concentrations tested, 1 pM and 100 fM show essentially the same signal. However, the measured mean signal at 100 fM is still distinguishably larger than the noise floor. Moreover, the increased signal appears to be specific to streptavidin. A panel of other blood proteins, DNA, and enzymes at 1 nM was incubated with droplets with and without streptavidin (**Figure 3.6b**). Without streptavidin, the other analytes did not raise the signal to a level greater than 10, in accordance with the 100 fM streptavidin sample in Figure 3a. Similarly, co-incubation of molecules did not significantly change the activation of droplets, with the exception of thrombin aptamer, which appeared to reduce signal (**Figure 3.6b**). In future studies, the experimental imaging setup will be optimized to better distinguish small numbers of aggregates and reduce signal variance between samples.

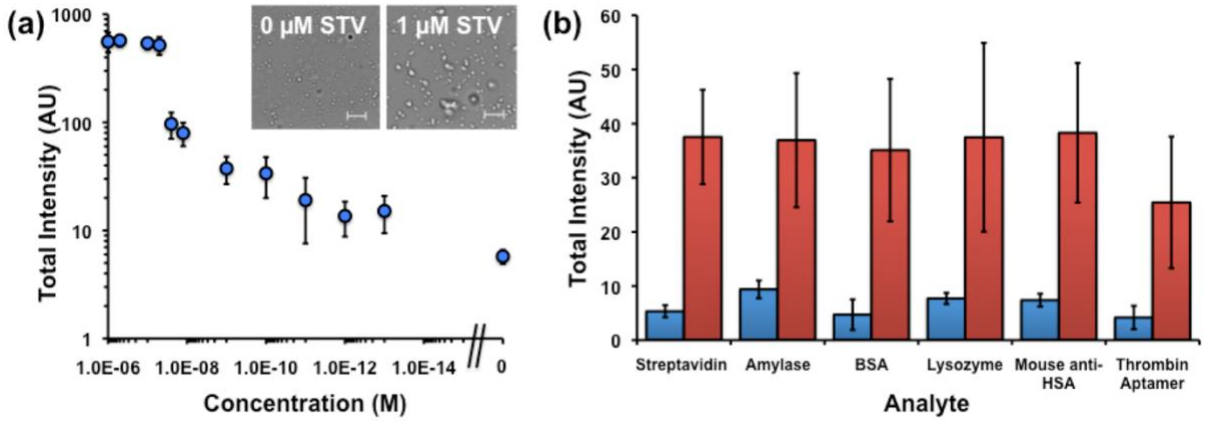

Figure 3.6. Integrated brightness from HIFU pulsing of droplet samples. (a) Brightness as function of streptavidin concentration. Right-most data point indicates no streptavidin addition. Inset: Bright field microscopy images of droplets at indicated streptavidin loading. Scale bar = 5 µm. (b) Brightness for various analytes at 1 nM each. Blue bar indicates brightness without 1 nM streptavidin, red bar indicates brightness with both stretptavidin and indicated analyte co-mixed.

3.4.3. Mechanism of aggregated droplet vaporization. The acquired data also provided evidence as to the mechanism of droplet vaporization. First, the aggregation of droplets may lead to fusion[38] and formation of nuclei for enhanced vaporization, but this was ruled out by the lack of any significant signal found in the highly aggregated 1 µM streptavidin samples prior to introduction of HIFU (**Figure 3.4**). Second, aggregation of droplets may lead to decreased Laplace pressure[35], but this is an unlikely explanation because the agglomerates appear to be intact by microscopy, so each of the droplets in the aggregate should still have the same surface area and thus the same Laplace pressure. In addition, this theory would not explain the low limit of detection of small order aggregates, for which a potential change in surface area would be small. Another explanation was recently posited by Shpak, *et al.,* who found that droplets could refract planar acoustic waves into focal zones of constructive interference that could lead to nucleation sites

typically positioned outside the walls of the droplet.[36] While their study only considered the case in which interference was focused into the confined volume of a single droplet, the focal zone in our studies may actually be present within an adjacent droplet instead. Aggregation may also cause the refraction to change, which in turn may cause enhanced or more localized focusing. This observation indicates promise for future in vivo studies, in which nanodroplet accumulation at a specific site (e. g. a tumor) may be limited and thus only smaller order aggregates are likely to form.

Finally, because the mechanism of detection is based on dispersed nanodroplets, the time required to achieve a positive result is greatly reduced as compared to conventional surface-bound sandwich assays. Typical ELISA assays require about four hours from initial sample incubation to development, partly due to the time required for sample to diffuse from the droplet down to the capture antibodies on the walls of the well. In addition, analyte incubation time must be optimized to allow sufficient sensitivity while ensuring that the signal does not saturate at high analyte concentrations (**Figure 3.7a-b**). Since the mechanism of sensing requires aggregation of droplets, and since the protein analytes will diffuse faster than the droplets, the limiting step is simply two droplets finding one another. Initially, the mean interdroplet distance can be estimated for a concentration N of $5x10^{15}$ as measured by NTA as being approximately 6 μm:

$$r = N^{-\frac{1}{3}} \quad (3.1)$$

Using Swift and Friedlander's treatment of the Smoluchowski and Stokes-Einstein equations, the half-life of nanodroplet aggregation found from **Equation 3.2**, where η is the viscosity of the buffer ($8.9x10^{-4}$ Pa-s), k_B is Boltzmann's constant ($1.38x10^{-23}$ J K^{-1}), T is the absolute temperature

(298 K), and N is concentration ($5x10^{15}$ m^{-3} as measured by NTA). This was calculated to be approximately 30 s for two droplets aggregating[40–42]. For larger analyte concentrations the aggregation rate is expected to slow as the particle agglomerate diffuse more slowly through solution. To test this theory, a suspension of nanodroplets was mixed with 1 pM, 1 nM, and 1 μM streptavidin, and their responses to HIFU were measured at various time intervals up to 10 min (**Figure 3.7c**). In the case of 1 pM and 1 nM, the corresponding full signal response was seen in only 2 min, relating nicely to the predicted aggregation halflife. For 1 μM streptavidin, the signal appears to increase further after 5 min, which is consistent with the formation of higher-order aggregates, as formation of initial aggregates slows diffusion speed. For the 1 μM streptavidin sample, full signal was still achieved in only 10 min. These results indicate that nanodroplet-based ultrasound detection may be utilized for rapid analyte sensing.

$$t_{1/2} = \frac{3h}{4kTN} \quad \text{.....(3.2)}$$

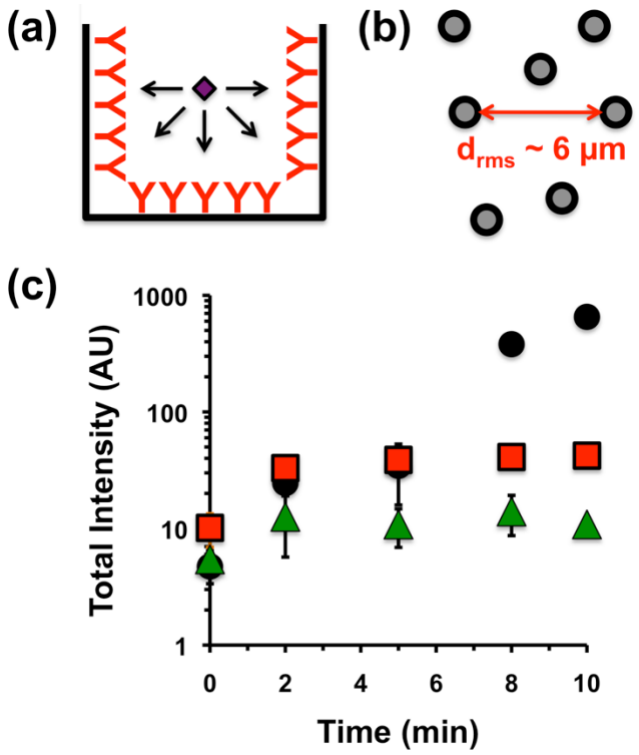

Figure 3.7. (a) Schematic of analyte diffusion onto walls of well during sandwich assay. (b) Schematic of interdroplet distance as measured from droplet concentration of $5x10^{15}$ m^{-3}. (c) Integrated brightness vs. time from HIFU pulsing of droplets with 1 µM (black circles), 1 nM (red squares), or 1 pM (green triangles) streptavidin added at time 0. Error bar = 1 SD, study was run in triplicate.

3.4.4. Sensing of Vascular Endothelial Growth Factor in saline and physiological media. As detailed in **Chapter 2.4.4**, Vascular Endothelial Growth factor is an important diagnostic marker for the presence cancerous tissue. To validate the utility of PFH droplets as practical biosensors, anti-VEGF aptamer-coated droplets were incubated with or without different amounts of VEGF-165 in TBS. The formulation of lipid-PEG-aptamer stock as a precursor to making droplets is detailed in **Chapter 2.3.5** and **2.4.4.** As can be seen from **Figure 3.8**, VEGF-induced aggregation (**Figure 3.8a-b**) causes a lowering of vaporization threshold of PFH droplets, allowing for the

sensing of the analyte down to 100 fM, with 1 nM showing a massive increase in signal (**Figure 3.8c**). However, preliminary experiments showed that, on incubation of the same droplets with VEGF dimer in 50% Fetal Bovine Serum (FBS), the sensitivity of the system was markedly decreased, with only >1nM VEGF being capable of being detected with clarity (**Figure 3.8d**). An interesting observation was, that unlike the vaporization of only aggregated droplets at 12 cycles in TBS, both control and aggregated droplets vaporized completely at 12 cycles. The vaporization threshold of droplets were found to decrease to 6 cycles in the presence of FBS, possibly due to non-specific protein adsorption by the droplets resulting in a disruption of the droplets shell. Addition of longer-chained lipids or PEG-30000 did not seem to significantly change this reduced threshold (data not shown). Thus it should be remembered that, for PFH droplets, the vaporization properties *in vivo* or simply in physiological media will not follow the same trends as that in saline.

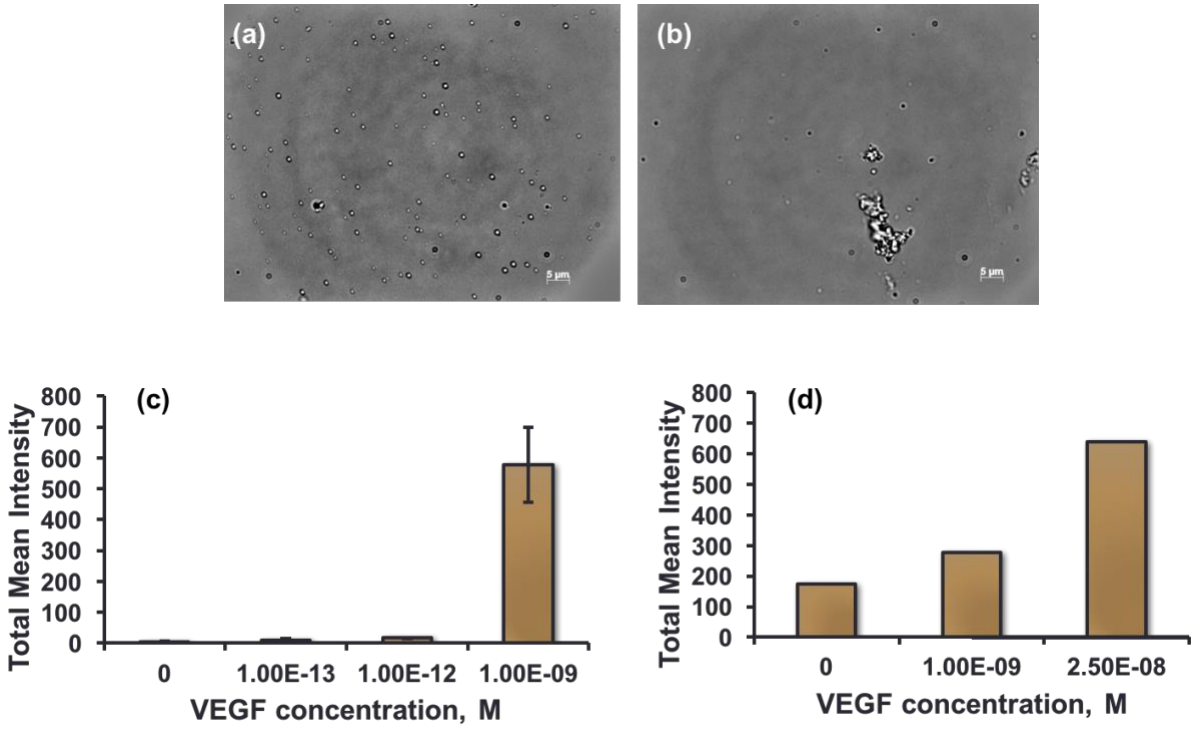

Figure 3.8. a-b. Bright field microscopy images of anti-VEGF aptamer coated PFH droplets without (**a**) and with (**b**) 100 nM VEGF-165 in TBS. **c-d.** Integrated brightness from HIFU pulsing of droplet samples in TBS (*at 12 cycles*) (**c**) and 50 vol% FBS (*at 6 cycles*) (**d**) at different VEGF-165 concentrations.

3.5. Conclusion

This report describes superheated liquid nanodroplets capable of acting as acoustic biosensors via a novel aggregation mechanism. It was found that biomolecules could induce aggregation of the nanodroplets, which in turn changed their to be vaporized into bubbles by High Intensity Focused Ultrasound. Nanodroplets were induced to form aggregates via biotin-streptavidin interactions, allowing detection of streptavidin and VEGF-165 by ultrasound scanning with concentrations as little as 100 fM and times under 10 min. Owing to the innate sensitivity of the detection process and low background for CPS imaging in vivo, these nanodroplets have substantial potential to be in vivo imaging agents capable of sensing small of quantities of prognostic biomarkers in localized areas within deep tissue. As of now, the sensitivity of the system was found to be lowered in physiological media due to interference by non-specific serum proteins. It was also reported for the first time that the acoustic intensity required to vaporize PFH nanodroplets is drastically reduced when droplets are placed in physiological media as opposed to saline. Such observations should allow for better design of perfluorocarbon droplets for performance *in vivo*.

3.6. Acknowledgement

This work was supported by NIH grants R00CA153935, DP2EB020401, and R21EB018034.

The authors would like to thank Prof. Mark Borden for use of his Sequoia Acuson C512

ultrasound imager. The authors would also like to thank Prof. Mark Borden, Prof. Todd Murray, and Prof. Jennifer Cha helpful discussions.

3.7. References

1. Weissleder, R., Tung, C.-H., Mahmood, U., and Jr, A.B. (1999) In vivo imaging of tumors with protease-activated near-infrared fluorescent probes. *Nat. Biotechnol.*, **17** (4), 375–378.

2. Olson, E.S., Jiang, T., Aguilera, T.A., Nguyen, Q.T., Ellies, L.G., Scadeng, M., and Tsien, R.Y. (2010) Activatable cell penetrating peptides linked to nanoparticles as dual probes for in vivo fluorescence and MR imaging of proteases. *Proc. Natl. Acad. Sci.*, **107** (9), 4311–4316.

3. Razgulin, A., Ma, N., and Rao, J. (2011) Strategies for in vivo imaging of enzyme activity: an overview and recent advances. *Chem. Soc. Rev.*, **40** (7), 4186–4216.

4. Guo, Z., Park, S., Yoon, J., and Shin, I. (2014) Recent progress in the development of near-infrared fluorescent probes for bioimaging applications. *Chem. Soc. Rev.*, **43** (1), 16–29.

5. Terai, T., and Nagano, T. (2008) Fluorescent probes for bioimaging applications. *Curr. Opin. Chem. Biol.*, **12** (5), 515–521.

6. Kobayashi, H., and Choyke, P.L. (2011) Target-cancer cell specific activatable fluorescence imaging Probes: Rational Design and in vivo Applications. *Acc. Chem. Res.*, **44** (2), 83–90.

7. Jiang, T., Olson, E.S., Nguyen, Q.T., Roy, M., Jennings, P.A., and Tsien, R.Y. (2004) Tumor imaging by means of proteolytic activation of cell-penetrating peptides. *Proc. Natl. Acad. Sci.*, **101** (51), 17867–17872.

8. Min, C., Shao, H., Liong, M., Yoon, T.-J., Weissleder, R., and Lee, H. (2012) Mechanism of Magnetic Relaxation Switching Sensing. *ACS Nano*, **6** (8), 6821–6828.

9. von Maltzahn, G., Park, J.-H., Lin, K.Y., Singh, N., Schwöppe, C., Mesters, R., Berdel, W.E., Ruoslahti, E., Sailor, M.J., and Bhatia, S.N. (2011) Nanoparticles that communicate *in vivo* to amplify tumour targeting. *Nat. Mater.*, **10** (7), 545–552.

10. Park, J.-H., von Maltzahn, G., Zhang, L., Schwartz, M.P., Ruoslahti, E., Bhatia, S.N., and Sailor, M.J. (2008) Magnetic Iron Oxide Nanoworms for Tumor Targeting and Imaging. *Adv. Mater.*, **20** (9), 1630–1635.

11. Sboros, V. (2008) Response of contrast agents to ultrasound. *Adv. Drug Deliv. Rev.*, **60** (10), 1117–1136.

12. Schutt, E.G., Klein, D.H., Mattrey, R.M., and Riess, J.G. (2003) Injectable Microbubbles as Contrast Agents for Diagnostic Ultrasound Imaging: The Key Role of Perfluorochemicals. *Angew. Chem. Int. Ed.*, **42** (28), 3218–3235.

13. Phillips, P. and Gardner, E. (2004) Contrast–agent detection and quantification. *Eur. Radiol. Suppl.*, **14** (8), P4–P10.

14. Nakatsuka, M.A., Hsu, M.J., Esener, S.C., Cha, J.N., and Goodwin, A.P. (2011) DNA-Coated Microbubbles with Biochemically Tunable Ultrasound Contrast Activity. *Adv. Mater.*, **23** (42), 4908–4912.

15. Klibanov, A.L., Rasche, P.T., Hughes, M.S., Wojdyla, J.K., Galen, K.P., Wible, J.H., and Brandenburger, G.H. (2002) Detection of individual microbubbles of an ultrasound contrast agent: fundamental and pulse inversion imaging. *Acad. Radiol.*, **9 Suppl 2**, S279-281.

16. Grinstaff, M.W., and Suslick, K.S. (1991) Air-filled proteinaceous microbubbles: synthesis of an echo-contrast agent. *Proc. Natl. Acad. Sci.*, **88** (17), 7708–7710.

17. Coley, B.D., Trambert, M.A., and Mattrey, R.F. (1994) Perfluorocarbon-enhanced sonography: value in detecting acute venous thrombosis in rabbits. *Am. J. Roentgenol.*, **163** (4), 961–964.

18. Porter, T.R., Iversen, P.L., Li, S., and Xie, F. (1996) Interaction of diagnostic ultrasound with synthetic oligonucleotide-labeled perfluorocarbon-exposed sonicated dextrose albumin microbubbles. *J. Ultrasound Med.*, **15** (8), 577–584.

19. Forsberg, F., Roy, R., Merton, D.A., Rawool, N.M., Liu, J.-B., Huang, M., Kessler, D., and Goldberg, B.B. (1998) Conventional and hypobaric activation of an ultrasound contrast agent. *Ultrasound Med. Biol.*, **24** (8), 1143–1150.

20. Nakatsuka, M.A., Mattrey, R.F., Esener, S.C., Cha, J.N., and Goodwin, A.P. (2012) Aptamer-Crosslinked Microbubbles: Smart Contrast Agents for Thrombin-Activated Ultrasound Imaging. *Adv. Mater.*, **24** (45), 6010–6016.

21. Nakatsuka, M.A., Barback, C.V., Fitch, K.R., Farwell, A.R., Esener, S.C., Mattrey, R.F., Cha, J.N., and Goodwin, A.P. (2013) In vivo ultrasound visualization of non-occlusive blood clots with thrombin-sensitive contrast agents. *Biomaterials*, **34** (37), 9559–9565.

22. Goodwin, A.P., Nakatsuka, M.A., and Mattrey, R.F. (2015) Stimulus–responsive ultrasound contrast agents for clinical imaging: motivations, demonstrations, and future directions. *WIREs Nanomed. Nanobiotechnol.*, **7** (1), 111–123.

23. Shapiro, M.G., Goodwill, P.W., Neogy, A., Yin, M., Foster, F.S., Schaffer, D.V., and Conolly, S.M. (2014) Biogenic gas nanostructures as ultrasonic molecular reporters. *Nat. Nanotechnol.*, **9** (4), 311–316.

24. Jokerst, J.V., Khademi, C., and Gambhir, S.S. (2013) Intracellular Aggregation of Multimodal Silica Nanoparticles for Ultrasound-Guided Stem Cell Implantation. *Sci. Transl. Med.*, **5** (177), 177ra35-177ra35.

25. Cavalieri, F., Micheli, L., Kaliappan, S., Teo, B.M., Zhou, M., Palleschi, G., and Ashokkumar, M. (2013) Antimicrobial and Biosensing Ultrasound-Responsive Lysozyme-Shelled Microbubbles. *ACS Appl. Mater. Interfaces*, **5** (2), 464–471.

26. Hettiarachchi, K., and Lee, A.P. (2010) Polymer–lipid microbubbles for biosensing and the formation of porous structures. *J. Colloid Interface Sci.*, **344** (2), 521–527.

27. Kopechek, J.A., Park, E., Mei, C.-S., McDannold, N.J., and Porter, T.M. (2013) Accumulation of Phase-Shift Nanoemulsions to Enhance MR-Guided Ultrasound-Mediated Tumor Ablation In Vivo. *J. Healthc. Eng.*

28. Zhang, P., and Porter, T. (2010) An in vitro Study of a Phase-Shift Nanoemulsion: A Potential Nucleation Agent for Bubble-Enhanced HIFU Tumor Ablation. *Ultrasound Med. Biol.*, **36** (11), 1856–1866.

29. Giesecke, T., and Hynynen, K. (2003) Ultrasound-mediated cavitation thresholds of liquid perfluorocarbon droplets in vitro. *Ultrasound Med. Biol.*, **29** (9), 1359–1365.
30. Gao, Z., Kennedy, A.M., Christensen, D.A., and Rapoport, N.Y. (2008) Drug-loaded nano/microbubbles for combining ultrasonography and targeted chemotherapy. *Ultrasonics*, **48** (4), 260–270.

31. Wang, C.-H., Kang, S.-T., Lee, Y.-H., Luo, Y.-L., Huang, Y.-F., and Yeh, C.-K. (2012) Aptamer-conjugated and drug-loaded acoustic droplets for ultrasound theranosis. *Biomaterials*, **33** (6), 1939–1947.

32. Sheeran, P.S., Luois, S., Dayton, P.A., and Matsunaga, T.O. (2011) Formulation and Acoustic Studies of a New Phase-Shift Agent for Diagnostic and Therapeutic Ultrasound. *Langmuir*, **27** (17), 10412–10420.

33. Fabiilli, M.L., Haworth, K.J., Sebastian, I.E., Kripfgans, O.D., Carson, P.L., and Fowlkes, J.B. (2010) Delivery of Chlorambucil Using an Acoustically-Triggered Perfluoropentane Emulsion. *Ultrasound Med. Biol.*, **36** (8), 1364–1375.

34. Rapoport, N., Nam, K.-H., Gupta, R., Gao, Z., Mohan, P., Payne, A., Todd, N., Liu, X., Kim, T., Shea, J., Scaife, C., Parker, D.L., Jeong, E.-K., and Kennedy, A.M. (2011) Ultrasound-mediated tumor imaging and nanotherapy using drug loaded, block copolymer stabilized perfluorocarbon nanoemulsions. *J. Controlled Release*, **153** (1), 4–15.

35. Kripfgans, O.D., Fowlkes, J.B., Miller, D.L., Eldevik, O.P., and Carson, P.L. (2000) Acoustic droplet vaporization for therapeutic and diagnostic applications. *Ultrasound Med. Biol.*, **26** (7), 1177–1189.

36. Shpak, O., Verweij, M., Vos, H.J., Jong, N. de, Lohse, D., and Versluis, M. (2014) Acoustic droplet vaporization is initiated by superharmonic focusing. *Proc. Natl. Acad. Sci.*, **111** (5), 1697–1702.

37. Xu, S., Zong, Y., Li, W., Zhang, S., and Wan, M. (2014) Bubble size distribution in acoustic droplet vaporization via dissolution using an ultrasound wide-beam method. *Ultrason. Sonochem.*, **21** (3), 975–983.

38. Mohan, P., Noonan, P.S., Nakatsuka, M.A., and Goodwin, A.P. (2014) On-Demand Droplet Fusion: A Strategy for Stimulus-Responsive Biosensing in Solution. *Langmuir*, **30** (41), 12321–12327.

39. Filipe, V., Hawe, A., and Jiskoot, W. (2010) Critical Evaluation of Nanoparticle Tracking Analysis (NTA) by NanoSight for the Measurement of Nanoparticles and Protein Aggregates. *Pharm. Res. N. Y.*, **27** (5), 796–810.

40. Swift, D.L., and Friedlander, S.K. (1964) The coagulation of hydrosols by brownian motion and laminar shear flow. *J. Colloid Sci.*, **19** (7), 621–647.

41. Lin, M.Y., Lindsay, H.M., Weitz, D.A., Klein, R., Ball, R.C., and Meakin, P. (1990) Universal diffusion-limited colloid aggregation. *J. Phys. Condens. Matter*, **2** (13), 3093.

42. Smoluchowski, M. v. (1918) Versuch einer mathematischen Theorie der Koagulationskinetik kolloider Lösungen. *Z. Für Phys. Chem.*, **92U** (1), 129–168.

Chapter 4. Phase Behavior of Mixed Lipid Monolayers on Perfluorocarbon Nanoemulsions and its Effect on Acoustic Contrast: Applications in Biomarker Sensing.

A similar version of this chapter first appeared in the article: Chattaraj, R., M. Goldscheitter, G., Yildirim, A., and P. Goodwin, A. (2016) Phase behavior of mixed lipid monolayers on perfluorocarbon nanoemulsions and its effect on acoustic contrast. RSC Adv., 6 (112), 111318–111325.

4.1. Abstract

Lipid-stabilized nanoemulsions containing a volatile liquid perfluorocarbon core have been studied as ultrasound contrast agents owing to their ability to transform into high-contrast microbubbles when subjected to high intensity focused ultrasound (HIFU). However, while there have been several studies on the effect of acoustic parameters on contrast, the effect of the droplet's stabilizing shell has not been studied as extensively. Inspired by previous studies showing lateral phase separation in microbubbles and vesicles, nanodroplets were formulated with a perfluorohexane core and a shell composed of varying amounts of saturated (DPPC) phospholipids, unsaturated (DOPC) phospholipids, and cholesterol, which were fractionated to obtain nanodroplets of mean diameter 300-400 nm and were stable over one week. When DOPC content was increased to 40 mol%, ultrasound contrast increased by about one order of magnitude over DPPC-only droplets. Based on fluorescence microscopy results of lateral lipid phase separation on the droplet surface, the various combinations of DPPC, DOPC, and cholesterol were assigned three regimes on the ternary phase diagram: solid-liquid ordered (low contrast), liquid ordered-liquid disordered (medium contrast), and solid-liquid disordered (high contrast). These

regimes were confirmed by TEM analysis of nanoscale droplets. Droplets containing mixed lipid monolayers were also found to produce a significantly greater yield than single-component droplets. Lastly, the increase of ultrasound contrast by creating a more disordered droplet monolayer was exploited in the detection of a model biomarker (phospholipase A_2) down to 0.1-1 nM in saline. The discovery of the dependence of acoustic response on lipid phase separation will help to understand the formulation, behavior, and vaporization mechanism of acoustically-responsive nanoemulsions.

4.2. Introduction

In recent decades, ultrasound contrast agents have been at the forefront of research in non-invasive medical imaging and therapy[1]. These agents are typically gas-filled bodies, or microbubbles, capable of resonating at clinical ultrasound frequencies while undergoing non-linear contraction and expansion[2]. While polymer and lipid-stabilized microbubbles have been adapted for wide-ranging applications in targeted molecular imaging,[3] cell sonoporation[4], and drug and gene delivery[5]. injected microbubbles are restricted to the intravascular areas in the body owing to their micron-range diameters. Instead, phase-shift nanoemulsions typically possess diameters on the order of hundreds of nanometers and thus are able to penetrate into extravascular spaces[6]. These nanoemulsions consist of a core of a volatile perfluorocarbon liquid encapsulated in a lipid/polymer shell. In their liquid state, the emulsions have negligible nonlinear acoustic contrast on account of the relatively incompressible liquid core. Application of high intensity focused ultrasound (HIFU) can cause the internal phase to vaporize and form metastable microbubbles, and thus creating significant ultrasound contrast in situ. However, vaporization must be well-controlled: although PFP nanoemulsions underwent Phase III clinical trials, one of the reasons

why the study was withdrawn was because of the increased occurrences of droplet growth due to Ostwald ripening and subsequent undesired “boiling” before injection[2].

While there have been numerous studies on the synthesis[7,8], applications[9], and mechanism of droplet vaporization[10,11], the phase behavior of the droplet shell structure and its potential effect on its contrast utility has to this date been largely unexamined. Most phase shift nanodroplets are stabilized by a either single type of phospholipid, doped with polymer-lipid conjugates for stability, or are formulated entirely from block copolymers[12], A recent study by Borden and coworkers suggested that the composition of the lipid monolayer, specifically the length of the lipid acyl chains, could play a role in temperature-dependent perfluorocarbon nanodroplet vaporization[13]. However, to the best of our knowledge, the effect of mixed lipids on droplet vaporization has not yet been studied.

Here, we hypothesized that introducing mixed lipid monolayers would facilitate perfluorocarbon nanodroplet vaporization by introducing surface roughness, decreasing monolayer rigidity, or both. To test the effects of mixed lipids on droplet vaporization, droplets were formulated with a monolayer consisting of saturated lipid (DPPC), unsaturated lipid (DOPC), and cholesterol. DPPC:DOPC:Cholesterol has been well studied in the past due to its ability to mimic cell membranes: such studies have identified a wide range of phase behavior associated with the lipid bilayer of mixed lipids, in which the lipids phase separate into domains with different tail packing densities[14]. Coexisting phases in a bilayer or monolayer can broadly be classified into ‘solid’ and ‘liquid’, the latter commonly sub-divided into liquid-crystalline (liquid-ordered, L_o) and liquid-expanded (liquid-disordered, L_d) phases[15–17]. In addition, cholesterol, which is associated with the formation of lipid rafts, provides access to numerous lateral phases for study[18–20]. Though most of these studies have been conducted on bilayers, it has been shown

that the liquid-liquid coexistence pattern of immiscible phases is similar in monolayers below the phase transition temperature of DPPC[21,22].

In the present study, we report the phase behavior of mixed lipid monolayers and its effect on the acoustic response of perfluorohexane (PFH) nanodroplets. While perfluoropentane (PFP, T_b = 29°C) is a more common nanodroplet internal phase due its lower vaporization threshold, we found that PFH droplets were not only more stable but also provided a greater variation of acoustic signal over a smaller range of incident intensities[23]. This combination of stability and control over vaporization has led to the increasing use of PFH nanodroplets for *in vitro* and *in vivo* applications, including conventional ultrasound theranostics[24,25], and photoacoustic imaging[26] and therapy[27]. Here, the variation of acoustic responses of droplets with varying monolayer compositions was correlated to the phase behavior on the droplet. The resulting observations were applied in the detection of a lipolytic biomarker (phospholipase A_2). This study provides a theoretical framework for explaining large increases in acoustic contrast for specific formulations, as presented below.

4.3. Experimental Section

4.3.1. Materials. 1,2-palmitoyl-*sn*-glycero-3-phosphocholine (DPPC), 1,2-dioleoyl-*sn*-glycero-3-phosphocholine (DOPC), 1,2-distearoyl-*sn*-glycero-3-phosphoethanolamine-N-[methoxy(polyethylene glycol)-2000] (ammonium salt) (DSPE-PEG2000), and 1,2-dioleoyl-*sn*-glycero-3-phosphoethanolamine-N-(lissamine rhodamine B sulfonyl) (ammonium salt) (RhB-DPPE) were purchased from Avanti Polar Lipids, Inc. (Alabaster, AL). Cholesterol was obtained from Alfa Aesar (Haverhill, MA), while perfluorohexane (PFH) was purchased from Strem Chemicals, Inc. (Newburyport, MA). Other materials used included chloroform, from Fisher

Scientific (Pittsburgh, PA), and Tris buffered saline (TBS) from Quality Biological Inc. (Gaithersburg, MD). Uranyl acetate was provided by Electron Microscopy Sciences (Hatfield, PA), while phospholipase A_2 from honey bee venom (*Apis mellifera*) and potassium permanganate were obtained from Sigma Aldrich (St. Louis, MO).

4.3.2. Formulation and Imaging of Nanodroplets. 400 *g* size-separated lipid-coated PFH nanodroplets were prepared as described previously in **Chapter 3.3.1 and 3.3.2**[23].

Droplet size distribution and concentration was determined through Nanoparticle Tracking Analysis using a NanoSight LM10 setup (Malvern Instruments Ltd., WR, United Kingdom). For long-term stability studies, resuspended droplets were stored in a glass vial purged with argon, and the size distributions were measured intermittently for seven days from preparation.

4.3.3. Ultrasound Contrast Imaging and Analysis. Ultrasound imaging studies were conducted as described previously in **Chapter 3.3.4**.

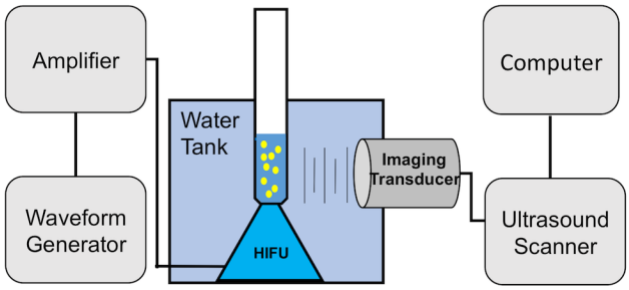

Figure 4.1. Schematic of ultrasound setup.

In a typical experiment, PFH nanodroplets were diluted to a concentration of approximately $(1.3\pm0.5)\text{x}10^{10}$ droplets mL^{-1} in TBS to a final volume of 1 mL per sample. Liposomes, when used, were diluted to 1 mL for a 10 µL probe-sonicated sample. For detection of phospholipase A_2

(PLA_2), droplets were incubated with different concentrations of the same in 1 mL TBS (at pH 8.9 with 5 mM Ca^{2+}) for 10 min at RT. The dilute sample was taken in a plastic pipette bulb positioned on top of the coupling cone to ensure proper HIFU focusing into the center of the sample, while a 4V1 transducer(Acuson) was aligned to acquire horizontal cross-sectional images of the sample while minimizing direct exposure to HIFU, as shown in **Figure 4.1.** The function generator was set to produce pulses at 1 Vpp, 1 MHz center frequency, 10 cycles with 0.1 s pulse interval (10 Hz). Videos were recorded in real time by a Siemens Acuson Sequoia™ C512 scanner operating in Cadence Pulse Sequencing mode at 1.5 MHz and a mechanical index (MI) of 0.19, which is consistent with non-destructive microbubble imaging at MI < 0.3[28,29]. Videos were captured about 10-15 min after droplet preparation.

Post-capture video analysis was performed via a code written in MATLAB (Mathworks, Inc.) For a given video, the code first selected a primary region of interest (ROI) from a frame in the video that displayed no sample signal, and the mean brightness value of this frame was set as the reference value for each successive frame brightness. A secondary ROI was selected upwards in the frame to eliminate frames containing signal contributions from HIFU pulse interference 'bands' within successive frames of the primary ROI. Each remaining frame was cropped to the primary ROI and converted to grayscale. The mean brightness values of all remaining frames were used to obtain an integrated intensity value over the entire span of the video.

4..3.4. Fluorescence Microscopy. For fluorescence microscopy, 1 mol% RhB-DPPE was added while preparing the original DPPC-DOPC-Cholesterol stock solution. Also, larger droplets (>2um) were necessary to discern the characteristics of the droplet shell. To obtain larger droplets, the original sonicated PFH emulsion was centrifuged at 50 *g*, following which the supernatant was

discarded and the pellet was resuspended in TBS for fluorescence imaging in an epifluorescence mode through a red channel using an Axio Imager A2 microscope (Zeiss). All images were captured approximately 10 min after droplet formulation. Images and videos were contrast-enhanced for better resolution of fluorescence distribution.

4.3.5. Transmission Electron Microscopy. To prepare samples for TEM imaging, diluted samples were reacted on a plasma-cleaned TEM grid with 1 w/v% potassium permanganate for 1 min. After washing with water, the sample was then stained with 1 w/v% uranyl acetate solution for 1 min, and air-dried thereafter. Images were taken using a CM 100 (Philips) microscope, operating at 80 kV.

4.4. Results and Discussion.

4.4.1. Variation of Shell Composition. Since the overall hypothesis of this work is that changes in lipid composition will produce differences in ultrasound contrast caused by the droplet, several ternary mixtures of DPPC, DOPC, and cholesterol were formulated along with 3 mol% DSPE-PEG2000 for steric stabilization. Larger compositions of cholesterol were avoided to maintain stability: above the solubility limit of cholesterol in lipid layers of around 40 mol%, crystallites may form that lead to irregularities in the shell[30]. Lipid films formed out of each formulation were reconstituted in TBS followed by the addition of 4 v/v% perfluorohexane (PFH) and subsequent probe sonication to form the emulsions.

Consistency in droplet size across different formulations was important for comparing vaporization of droplets because large droplets are expected to vaporize more easily due to reduced

Laplace pressure[23]. In order to obtain similar size ranges across different formulations, larger droplets were pelleted out at 400 *g*, and smaller droplets obtained within the supernatant were characterized using Nanoparticle Tracking Analysis (NTA, Malvern). Since the shell contributes negligibly to the total mass of a droplet compared to the perfluorohexane (PFH) internal phase, similar centrifugation conditions were expected to produce similar size distributions irrespective of the shell composition. NTA analysis of droplets prepared with all different shell compositions revealed that while the concentration yield was different for each composition, the mean diameter and size distributions were similar for all formulations (**Figure 4.2, Table 4.1**).

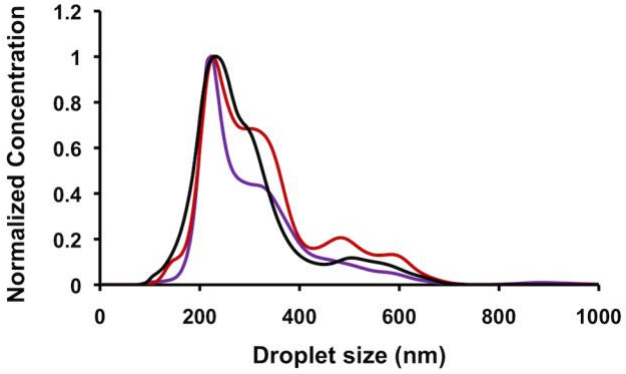

Figure 4.2. Normalized size distributions of 400 *g* fractionated PFH droplets for representative monolayer compositions (purple: 100:0:0; black: 60:30:10; red: 47.5:47.5:5).

Shell Composition	Mean Diameter (nm)	Std. Error (nm)	Std. Deviation (nm)
100:0:0	335.7	5.2	142.6
60:0:40	371.4	10.0	148.0

50:10:40	336.1	16.2	116.1
70:20:10	380.0	16.4	150.1
60:30:10	318.1	2.4	117.5
50:30:20	312.6	7.2	127.3
40:30:30	351.6	5.4	128.4
40:40:20	302.9	9.0	126.0
47.5:47.5:5	289.8	6.2	110.3
30:60:10	343.6	4.4	152.4

Table 4.1. Mean diameters, standard error, and standard deviation for droplets with different shell compositions.

4.4.2. HIFU Response for Ternary System. Based on our previous study, a concentration in the range of 10^9-10^{10} droplets per mL would be optimal for comparing droplet lipid compositions[23]. However, the variation in ultrasound signal was not linear with change in DOPC or cholesterol fractions **(Figure 4.3)**. For instance, 30 mol% or lower DOPC concentrations produced low-to-medium response, while 40-50 mol% DOPC enhanced the response by at least one order of magnitude (note: percentages are for lipids only and do not include DSPE-PEG2000). On the other hand, 40% cholesterol, even with 10 mol% DOPC, produced only an increase of ~2.5x in signal as compared to 100:0:0 DPPC:DOPC:Chol. For comparison, suspensions of 100:0:0 and

47.5:47.5:5 were sonicated without PFH in TBS and produced no detectable response (**Figure 4.4**). While a low response from 100:0:0 droplets might be expected due to their predominantly solid monolayer phase (see below), the effect of DOPC, cholesterol, and PEG-2000 composition required further exploration, which is detailed below.

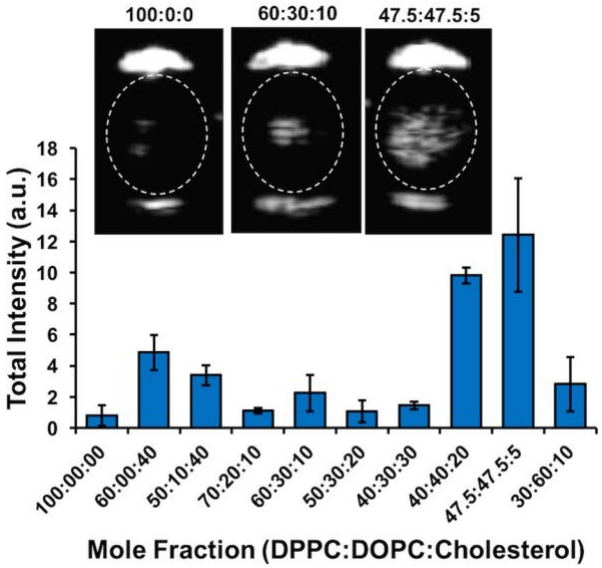

Figure 4.3. HIFU responses of 300-400 nm mean diameter PFH droplets with different monolayer compositions; Inset: ultrasound images of representative composition droplets (left to right: 100:0:0, 60:30:10, 47.5:47.5:5).

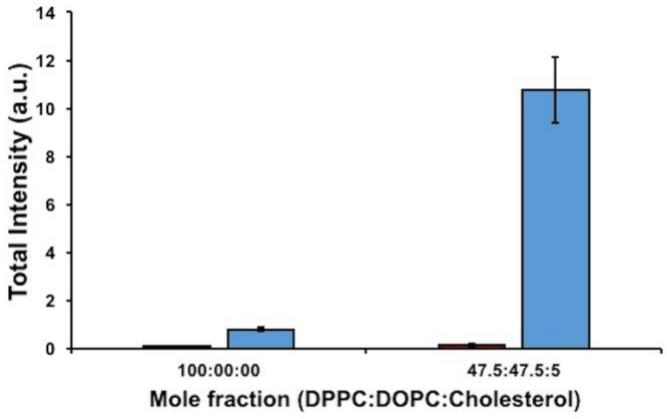

Figure 4.4. Comparison between HIFU responses of liposomes (*red*) and droplets (*blue*) for representative lipid-cholesterol compositions.

4.4.3. Fluorescent Microscopy of Droplets with Ternary Shell Compositions. Lateral phase behavior in the lipid monolayers surrounding the droplets was first examined by fluorescence microscopy of 1 mol% Lissamine rhodamine B-DPPE (RhB-DPPE) incorporated into the lipid film prior to hydration.[31] Although for clinical imaging droplets should be maintained at diameters smaller than 700 nm for potential penetration into an extravascular environment[9,32], lateral lipid phase separation cannot be observed optically in this size regime. Therefore, the droplets were pelleted and collected at 50 *g* instead of fractionated at 400 *g* to isolate the largest droplets. These droplets with diameters >1 μm were imaged for distribution of fluorescence. Representative images obtained for the majority droplet structure in each case are shown in **Figure 4.5(a-j).** Based on these results, we have classified the phase separation in these systems into roughly the following regions (**Figure 4.5k**):

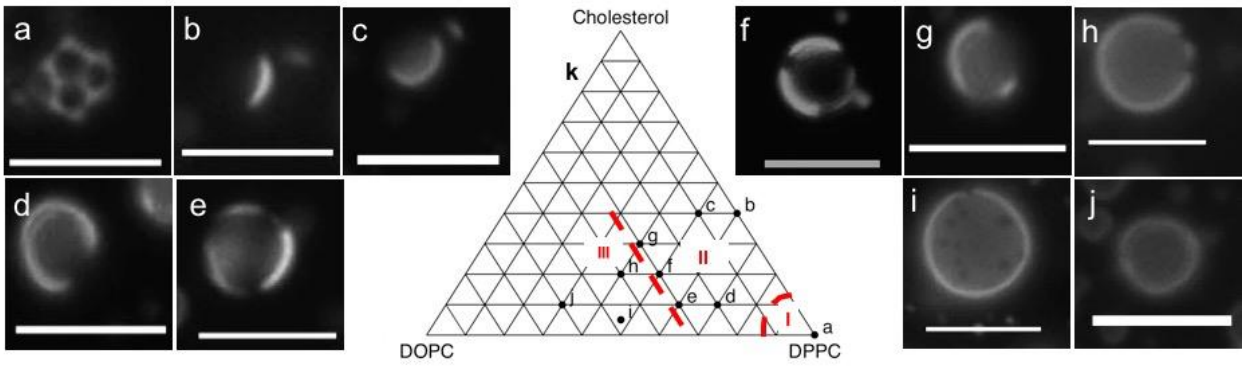

Figure 4.5. a-k: Fluorescence microscopy images of 50 *g* PFH droplets with shells of different compositions (mol% DPPC:DOPC:Cholesterol), 100:0:0 (a), 60:0:40 (b), 50:10:40 (c), 70:20:10

(d), 60:30:10 (e), 50:30:20 (f), 40:30:30 (g), 40:40:20 (h), 47.5:47.5:5 (i), and 30:60:10 (j). Scale bar: 5 μm; k: Sketch of ternary compositions of monolayers, showing S-L_o (I), L_o-L_d (II), and S-L_d (III) regions.

S-L_O (solid-liquid ordered phase coexistence): Absence of either DOPC or cholesterol causes the RhB-DPPE to be expelled from the solid DPPC phase and localize in the L_O DSPE-PEG2000 phase. A similar effect was previously observed for DPPC and DSPE-PEG2000 shell perfluorobutane microbubbles[22], in which the PEG2000 causes steric disruption in the DSPE layer, leading to a fluid but ordered phase. Because lipid-dye conjugates (such as Texas Red-DPPE) cannot adequately fit between the DPPC chains, it preferentially associates with the DSPE-PEG2000[31], As can be seen from **Figure 4.5a**, the domains obtained for 100:0:0 were almost consistently polygonal with equal 60^o angles at each vertex. This is represented in Figure 4k as Region I**.**

The effect of varying the concentration of DSPE-PEG2000 with respect to DPPC was studied as well. PEG-lipids are generally added to lipid-shelled agents for imaging and drug delivery to both provide steric stabilization and resist opsonization. To study the effect of PEG on phase separation in the monolayer, increasing PEG concentrations were added to the stock lipid solutions to formulate droplets. Previously, it was shown that increasing DSPE-PEG2000 concentration in a microbubble shell increases lateral phase separation[22], A similar trend was observed for the nanodroplets used in this study. In the aforementioned droplet samples, 3 mol% DSPE-PEG2000 was employed. Increasing DSPE-PEG2000 concentration to 10 mol% and 20 mol% led to a monolayer resembling a S-L_d coexistence region (as detailed later), with the RhB-DPPE dye being repelled by small, irregular, scattered, dark solid areas (**Figure 4.6**). These results support the assignment of the S-L_d coexistence in the 3 mol% DSPE-PEG2000 samples. Droplets formulated

without DSPE-PEG2000 were inherently unstable and settled down by forming aggregates (**Figure 4.7**).

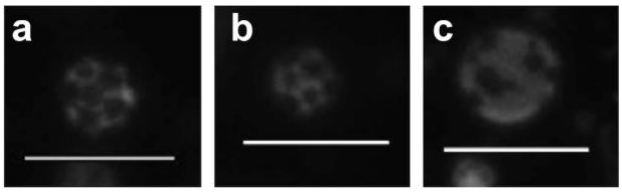

Figure 4.6. Phase behavior in 100:0:0 droplet monolayer as a function of increasing DSPE-PEG2000 concentration: 3 mo% (**a**), 10 mol% (**b**), and 20 mol% (**c**). Scale bar: 5 µm.

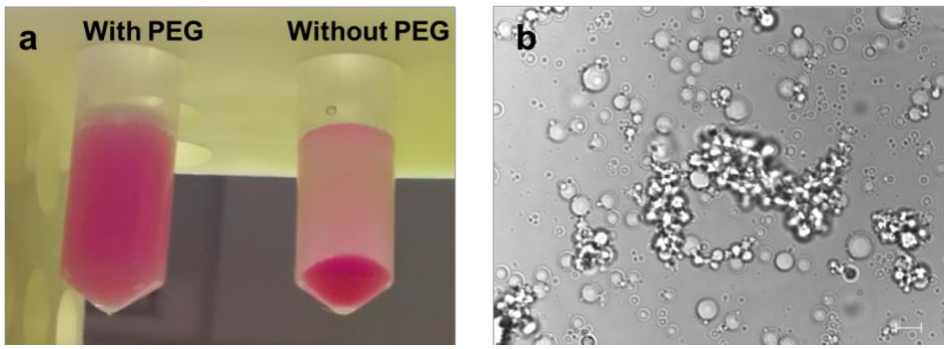

Figure 4.7. (a) 100:0:0 PFH emulsions formulated with and without DSPE-PEG2000; **(b)** Microscopy image of 100:0:0 PFH droplets without DSPE-PEG2000. Scale bar: 5 μm.

L_o-L_d (liquid ordered-liquid disordered phase coexistence): The majority of droplets for the compositions 70:20:10, 60:30:10, 40:30:30, and 50:30:20, or **Region II** (**Figure 4.5k)**, showed varying degrees of localization of dye at the droplet interface. The dye localization likely occurs within the unsaturated lipid-rich phase; this assignment is evident from the increasing bright area with increasing DOPC fraction. Since these images were captured 10-15 min after droplet preparation (similar to the timeline followed for recording HIFU responses), it is possible that the peripheral bright areas are a result of ripening of dark L_o domains as a result of mutual collisions,

leading to a larger dark region. High cholesterol concentrations (50:10:40 and 60:0:40) limit the L_o phase to highly concentrated regions, edging closer to a one-liquid phase.

S-L_d (solid-liquid disordered phase coexistence): As the concentration of the unsaturated lipid is increased further, the solid and liquid phases separate without mixing, resulting in the formation of scattered, dark solid domains. **Region III** (**Figure 4.5k**)**.** These domains are evident in the 47.5:47.5:5 and 40:40:20 mixtures as tiny dark spots visible under fluorescence surrounded by a uniform distribution of the dye indicating a relatively continuous liquid phase. Unlike the liquid-liquid coexistence region, these domains do not appear to ripen further after 10-20 min. Addition of excess DSPE-PEG2000 (20 mol%) resulted in a similar overarching distribution of the dye, albeit in a more diffuse manner, resulting in a more continuous liquid phase (**Figure 4.8**).

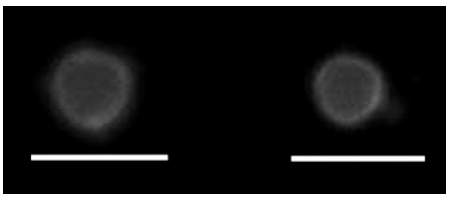

Figure 4.8. Fluorescence microscopy images of 50 *g* sample 47.5:47.5:5 PFH droplets with 20% (by mole) DSPE-PEG2000. Scale bar: 5 μm.

One-Liquid phase: At high unsaturated lipid concentrations (30:60:10, **Figure 4.5j**), and possibly at very high cholesterol compositions, the dye spreads uniformly throughout the monolayer, indicating the lack of domain formation and the presence of a single, continuous liquid phase.

The above phase classifications are given as the majority species for each sample; however, due to the dynamic nature of the shell formulation and existence, some droplets in each image exhibit a different apparent phase. For instance, a few droplets in the L_O-L_d coexistence region (Region II, **Figure 4.5j**) showed large dark domains on a bright background. These droplets are likely to be indicative of initial stages of domain ripening, in which the dark L_O phase areas collide with each

other**,** resulting in a final state as shown in **Figure 4.5(a-j).** Images of different single droplets representing different phases for a representative composition (60:30:10) are shown in **Figure 4.9**: these images likely denote the various stages of domain ripening for droplets exhibiting L_O-L_d coexistence. In contrast, droplets in the S-L_d coexistence region also contains highly mobile dark domains, but instead of ripening, these solid segments remain as isolated areas in an otherwise expanded liquid phase.

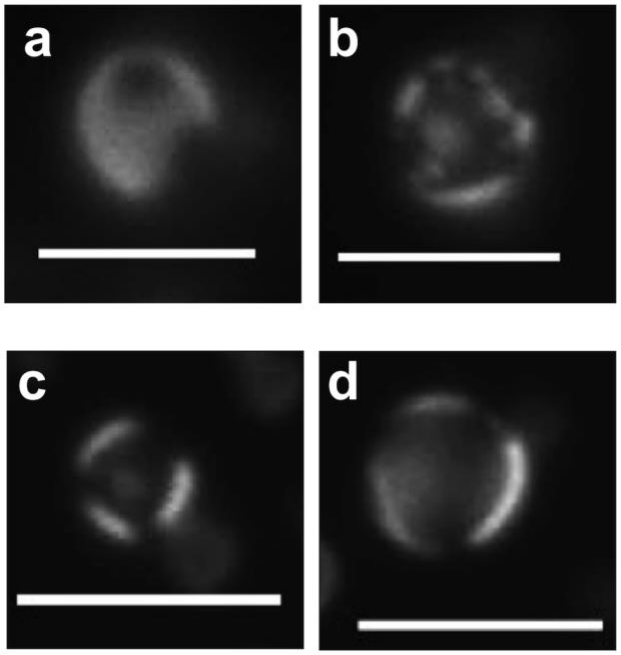

Figure 4.9. Different droplets depicting possible domain ripening (from **a-d**) in a representative liquid-liquid coexistence sample (60:30:10). Scale bar: 5 μm.

Also, to ascertain that small alterations of ambient temperature did not affect monolayer phase behavior, 100:0:0 droplets were either heated at 37^0C for 30 min or cooled in an ice-water bath for 15 min, followed by fluorescence microscopy. The presence of polygonal domains was much the same (**Figure 4.10**). While kinetics of domain formation may be affected in a time scale of seconds or a few minutes, the final dynamic state of the monolayer thus reached was seen to be independent

of temperature (below the phase-transition of the major lipid component), which would therefore not affect the HIFU response of the droplets.

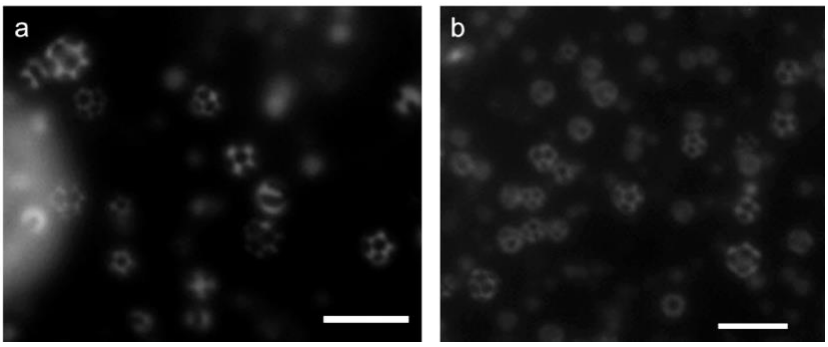

Figure 4.10. Fluorescence microscopy images of 50 *g* 100:0:0 PFH droplets after 30 min of heating at 37^0C **(a)** and 15 min of cooling in an ice-bath **(b)** immediately after droplet preparation. Scale bar: 5 μm.

4.4.4. TEM Analysis. While optical microscopy is instrumental for depicting phase behavior on the droplet shell, it is only able to resolve features on microdroplets, and thus it is not possible to distinguish lipid domains on a 300-400 nm diameter droplet. TEM was thus conducted to examine the shell properties of droplets on this scale. Droplets were prepared as for the ultrasound studies, then stained with both 1 w/v% $KMnO_4$ and 1 w/v% UOAc as an alkene stain and negative stain, respectively. Since droplets were imaged under standard high vacuum TEM conditions, the vacuum was expected to vaporize the PFH interior, leaving a hollow shell. Solid shells were expected to maintain their shape but liquid domains would not, leading to collapse of these lipid monolayers. Three compositions were tested to support this hypothesis: 100:0:0 (S-L_o), 60:30:10 (L_o-L_d), and 47.5:47.5:5 (S-L_d) (**Figure 4.11**). The S-L_o region, due to the overbearing presence of a solid phase, shows a uniform texture throughout, due to its relatively rigid shell avoiding a drastic collapse. The L_o-L_d droplet shells collapse in their entirety, leading to 'pancake'-like images,

showing a relatively faint difference in resolution. However, in the S-L_d regime the liquid phase in the monolayer appears to collapse selectively as compared with the solid phase. This liquid phase should be more rich in DOPC and cholesterol and thus appears darker accordingly due to selective staining by $KMnO_4$.

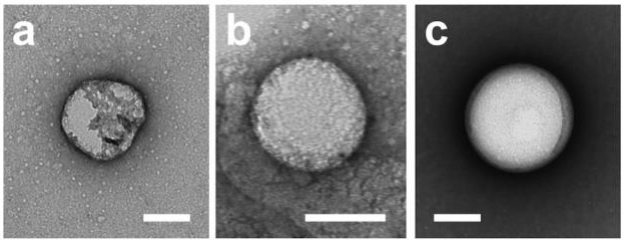

Figure 4.11. TEM images of PFH droplets of representative monolayer compositions (mol% DPPC:DOPC:Cholesterol): 47.5:47.5:5 (a), 60:30:10 (b), 100:0:0 (c). Scale bar = 100 nm.

4.4.5. Correlation of Phase Behavior with HIFU Response. The extent of phase separation observed in the droplet monolayer provides a correlation of lipid structure with HIFU response. The presence of solid areas in a S-L_d coexistence likely allows for presence of numerous nucleation sites of a combined high surface area for easier vaporization of the internal liquid phase. Similarly, an increased concentration of unsaturated lipid (40 mol% or more) contributes to a decrease in the overall rigidity of the shell monolayer. These two effects together may facilitate the easier vaporization of droplets with lipid compositions such as 47.5:47.5:5 and 40:40:20. However, a lower response from the 30:60:10 droplets would seem to indicate that solid heterogeneities in the monolayer is the predominant factor for easier boiling of the internal PFC phase. The relatively high response of the compositions 50:10:40 and 60:0:40 are outliers in this scheme. Formulations with high cholesterol content were found to create droplets with high size dispersity and low stability, and thus increased signal was likely due to spontaneous coalescence into larger droplets

(**Table 4.1**) rather than phase behavior. In addition, while high cholesterol concentrations produced a disordered phase, the line tension is also correspondingly lowered, leading to instability (lowering of concentration) over time. Similarly, increasing PEG concentrations also increased acoustic response. HIFU response for 100:0:0 droplets (with 3, 10, and 20 mol% PEG concentration) of similar size and concentration (**Figure 4.12a**), the signal was found to increase significantly for a 20 mol% DSPE-PEG2000 concentration, in keeping with what was expected for a S-L_d region sample (**Figure 4.12b, Figure 4.6c**).

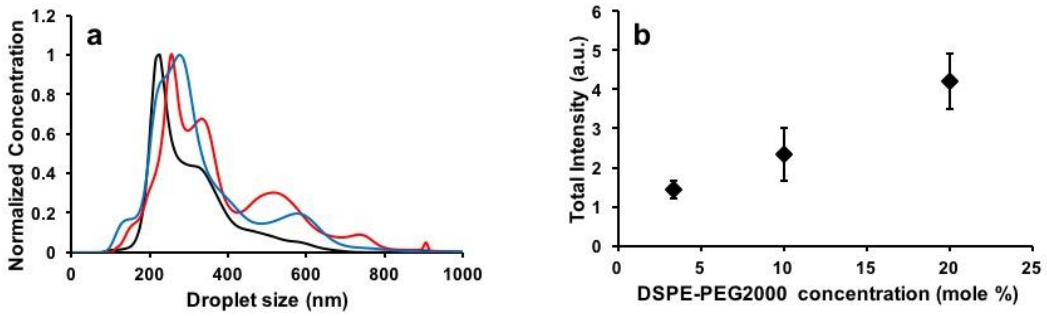

Figure 4.12. (a) Normalized size distributions of 400 *g* fractionated 100:0:0 droplets with 3.33% (*black*), 10% (*red*), and 20% (*blue*) DSPE-PEG2000 concentration; **(b)** HIFU response of 100:0:0 droplets of mean size 300-400 nm as a function of DSPE-PEG2000 concentration.

4.4.5.1. Utilization of Mixed Lipid Droplets as a More Efficient Ultrasound Contrast Agent. The above observations support the use of mixed-lipid nanodroplets as ultrasound contrast agents. A droplet shell consisting of a 1:1 ratio of saturated and unsaturated lipids along with a low amount of cholesterol appears to have several empirical advantages over a droplet shell composed mainly of lipid. For comparison, the 47.5:47.5:5 droplets had a similar size range as that of the 100:0:0 sample (**Figure 4.2**), but its HIFU response is about one order of magnitude higher (**Figure 4.3**)

at the same concentration. This difference in acoustic response is particularly pronounced at the perceived threshold of vaporization (9.8 MPa, 10 cycles) (**Figure 4.13**).

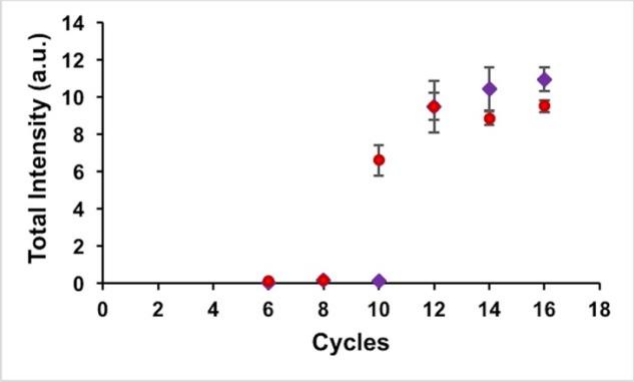

Figure 4.13. Variation of HIFU responses of 300-400 nm (mean diameter) PFH droplets, formulated out of 100:0:0 (*purple diamonds*) and 47.5:47.5:5 (*red circles*) compositions with number of HIFU cycles applied

It should be noted that HIFU response is concentration dependent, and an excess amount of droplets produces a high response regardless of the shell composition, while a low droplet number produces negligible signal. However, for these formulations there is a large window of about two orders of magnitude of concentration in which 47.5:47.5:5 droplets produce a greater response than 100:0:0 droplets (**Figure 4.14a**). In addition, samples containing unsaturated lipids produced a larger yield of fractionated droplets (300-400 nm) than samples with DPPC only (**Figure 4.14b**), which could be useful for scaling up nanodroplet production. We ascribe the increased yield to both increased lipid mobility and the heterogeneity of lipid tail packing motifs, which allows formation of a lower energy shell structure. DPPC packs tightly in the monolayer, causing the DSPE-PEG to phase-separate, but prefers a planar structure[33]. Addition of DOPC likely helps to break up the crystalline plane and domains, which reduces the energy required to induce

curvature in the monolayer.[34,35] Finally, 47.5:47.5:5 samples exhibit similar stability profiles as 100:0:0 droplets (**Figure 4.14c-d, Figure 4.15**): only a slight decrease in mean diameter and concentration were observed over a period of one week, most likely due to diffusion of the internal PFH phase from the droplet and evaporation from the sample.

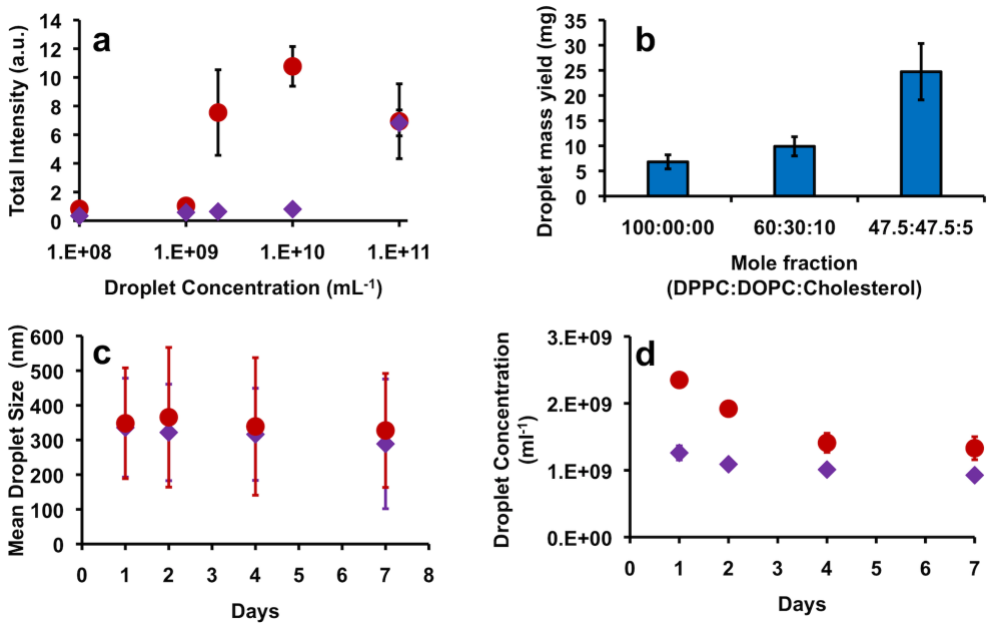

Figure 4.14. (a) HIFU responses of 300-400 nm (mean diameter) PFH droplets, formulated out of 100:0:0 (*purple diamonds*) and 47.5:47.5:5 (*red circles*) compositions; **(b)** Mass yield of 300-400 nm mean diameter droplets for representative shell compositions; **(c-d)**: Progression of mean size (**c**) and concentration (**d**) over time for fractionated PFH droplets stored at 2-8^{0}C – 100:0:0 (*purple diamonds*) and 47.5:47.5:5 (*red circles*). Error bars represent 1 SD.

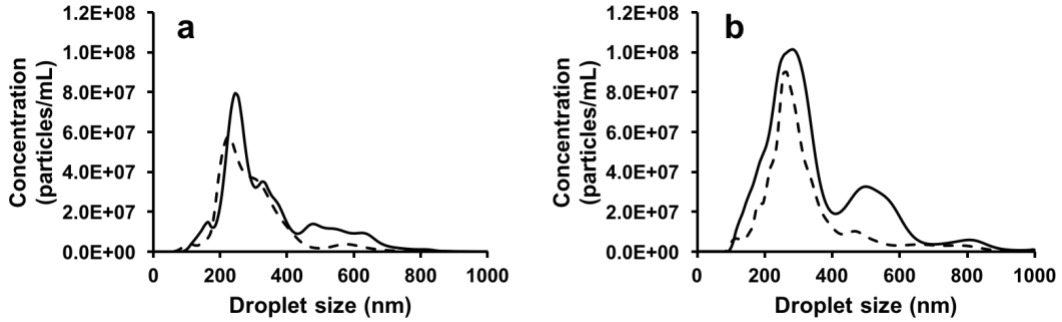

Figure 4.15. Size distributions of fractionated PFH droplets formulated out of 100:0:0 (a) and 47.5:47.5:5 (b) shell compositions; *solid line*: Day 1 of droplet preparation, *dashed line*: Day 7.

4.4.6. Sensing of phospholipase A_2. As we have observed, the organization of the lipid monolayer could significantly affect the HIFU response of PFH droplets. We wanted to apply this property to the sensing of an analyte which would act by disrupting/reorganizing the lipid spread in the droplet shell. One such biologically relevant analyte is phospholipase A_2. In terms of its utility as a biosensing analyte, PLA_2 is commonly found in the venom of snakes, arachnids, and insects,[36] in addition, it may also be upregulated in prostate[37] and lung cancers[38]. PLA_2 is an enzyme which catalyzes the *sn*2 position of the phospholipid glycerol backbone: this would 'fluidize' a gel-phase DPPC monolayer, for instance, by reducing the inter-chain cohesive forces and possibly reducing the residence time of lipid molecules in the shell. We hypothesized that, as with the more fluid mixed lipid monolayers, this would decrease the vaporization threshold of the droplets.

Incubation of DPPC-only PFH droplets with PLA_2 (at pH 8.9 with 5 mM Ca^{2+}, which are the optimum conditions for PLA_2 activity) showed signal initiation at as low as 6 cycles, whereas the difference was most pronounced at 8 cycles compared to droplets without any of the lipase (**Figure 4.16**); the dose response revealed that 1 nM and possibly 100 pM PLA_2 can be detected in as little as 10-15 min using PFH droplets and HIFU. Clinical levels of PLA_2 range from 1-10 nM[39]: hence this is a promising method for rapid, sensitive detection of the analyte.

The mechanism of the lowering of vaporization threshold by PLA_2 to 6 cycles instead of 10-12 can be two-fold. One, as with mixed lipids, PLA_2 cleavage of the DPPC molecules might be creating a solid-liquid disordered phase monolayer, thereby creating nucleation sites. Secondly, the possible loss of cleaved lipid molecules to the ambient solution might cause some of the PFH to leak out and thus lowering the boiling point of the liquid causing easier vaporization.

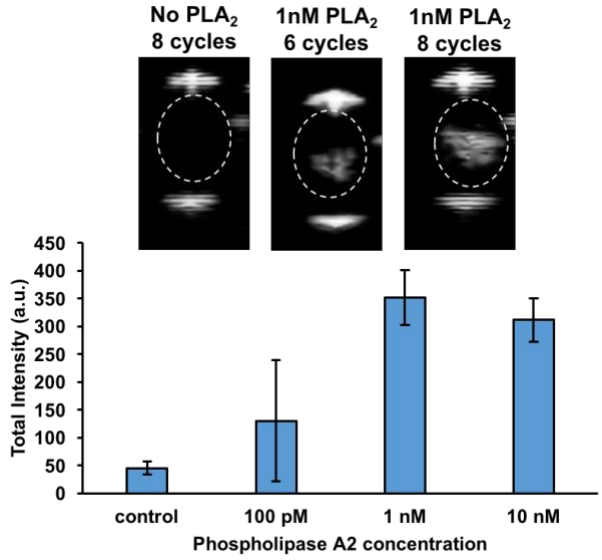

Figure 4.16. HIFU responses of DPPC (100:0:0) droplets incubated with varying concentrations of PLA_2. *Inset*: Ultrasound images of representative samples.

4.5. Conclusion

This work studied the effect of lateral lipid phase separation on vaporization of superheated liquid perfluorocarbon droplets. Droplets stabilized by a mixture of DPPC, DOPC, and cholesterol possessed higher ultrasound contrast in general than DPPC-only droplets; 1:1 molar ratio of DPPC:DOPC with 20 mol% or less cholesterol enhanced contrast by about an order of magnitude. A combination of fluorescence microscopy and TEM found that the range of lipid concentrations tested corresponded to three regimes in the ternary phase diagram: solid-liquid ordered (low

contrast), liquid ordered-liquid disordered (medium contrast), and solid-liquid disordered (high contrast). This property of PFH droplets to vaporize easier with a more liquid or more disorganized shell was used to detect 100pM-1nM phospholipase A_2 in a matter of 10-15 min. Future studies will focus on adapting mixed lipid droplets and detection of other lipolytic molecules under physiological conditions.

4.6. Acknowledgement

This work was supported by NIH grants DP2EB020401, R21EB018034, and R00CA153935. The authors thank Profs. Jennifer Cha and Mark Borden for helpful discussions. The authors thank Dr. Joseph Dragavon of the CU Biofrontiers Advanced Microscopy Core for help with fluorescence microscopy, and Dr. Thomas Giddings for help with TEM imaging and sample staining.

4.7. References

1. Deshpande, N., Needles, A., and Willmann, J.K. (2010) Molecular ultrasound imaging: current status and future directions. *Clin. Radiol.*, **65** (7), 567–581.

2. Schutt, E.G., Klein, D.H., Mattrey, R.M., and Riess, J.G. (2003) Injectable Microbubbles as Contrast Agents for Diagnostic Ultrasound Imaging: The Key Role of Perfluorochemicals. *Angew. Chem. Int. Ed.*, **42** (28), 3218–3235.

3. Klibanov, A.L. (2007) Ultrasound molecular imaging with targeted microbubble contrast agents. *J. Nucl. Cardiol.*, **14** (6), 876.

4. Karshafian, R., Bevan, P.D., Williams, R., Samac, S., and Burns, P.N. (2009) Sonoporation by Ultrasound-Activated Microbubble Contrast Agents: Effect of Acoustic Exposure Parameters on Cell Membrane Permeability and Cell Viability. *Ultrasound Med. Biol.*, **35** (5), 847–860.

5. Sirsi, S.R., and Borden, M.A. (2014) State-of-the-art materials for ultrasound-triggered drug delivery. *Adv. Drug Deliv. Rev.*, **72**, 3–14.

6. Rapoport, N. (2012) Phase-shift, stimuli-responsive perfluorocarbon nanodroplets for drug delivery to cancer. *WIREs Nanomed. Nanobiotechnol.*, **4** (5), 492–510.

7. Sheeran, P.S., Luois, S., Dayton, P.A., and Matsunaga, T.O. (2011) Formulation and Acoustic Studies of a New Phase-Shift Agent for Diagnostic and Therapeutic Ultrasound. *Langmuir*, **27** (17), 10412–10420.

8. Kopechek, J.A., Zhang, P., Burgess, M.T., and Porter, T.M. (2012) Synthesis of Phase-shift Nanoemulsions with Narrow Size Distributions for Acoustic Droplet Vaporization and Bubble-enhanced Ultrasound-mediated Ablation. *J. Vis. Exp. JoVE*, (67).

9. Matsunaga, T.O., Sheeran, P.S., Luois, S., Streeter, J.E., Mullin, L.B., Banerjee, B., and Dayton, P.A. (2012) Phase-Change Nanoparticles Using Highly Volatile Perfluorocarbons: Toward a Platform for Extravascular Ultrasound Imaging. *Theranostics*, **2** (12), 1185–1198.

10. Pitt, W.G., Singh, R.N., Perez, K.X., Husseini, G.A., and Jack, D.R. (2014) Phase transitions of perfluorocarbon nanoemulsion induced with ultrasound: A mathematical model. *Ultrason. Sonochem.*, **21** (2), 879–891.

11. Shpak, O., Verweij, M., Vos, H.J., Jong, N. de, Lohse, D., and Versluis, M. (2014) Acoustic droplet vaporization is initiated by superharmonic focusing. *Proc. Natl. Acad. Sci.*, **111** (5), 1697–1702.

12. Rapoport, N.Y., Kennedy, A.M., Shea, J.E., Scaife, C.L., and Nam, K.-H. (2009) Controlled and targeted tumor chemotherapy by ultrasound-activated nanoemulsions/microbubbles. *J. Controlled Release*, **138** (3), 268–276.

13. Mountford, P.A., Thomas, A.N., and Borden, M.A. (2015) Thermal activation of superheated lipid-coated perfluorocarbon drops. *Langmuir*, **31** (16), 4627–4634.

14. Veatch, S.L., and Keller, S.L. (2005) Seeing spots: Complex phase behavior in simple membranes. *Biochim. Biophys. Acta BBA - Mol. Cell Res.*, **1746** (3), 172–185.

15. McMullen, T.P.W., Lewis, R.N.A.H., and McElhaney, R.N. (2004) Cholesterol–phospholipid interactions, the liquid-ordered phase and lipid rafts in model and biological membranes. *Curr. Opin. Colloid Interface Sci.*, **8** (6), 459–468.

16. Quinn, P.J., and Wolf, C. (2009) The liquid-ordered phase in membranes. *Biochim. Biophys. Acta BBA - Biomembr.*, **1788** (1), 33–46.

17. Baoukina, S., Mendez-Villuendas, E., and Tieleman, D.P. (2012) Molecular view of phase coexistence in lipid monolayers. *J. Am. Chem. Soc.*, **134** (42), 17543–17553.

18. Hancock, J.F. (2006) Lipid rafts: contentious only from simplistic standpoints. *Nat. Rev. Mol. Cell Biol.*, **7** (6), 456–462.

19. Lingwood, D., and Simons, K. (2010) Lipid Rafts As a Membrane-Organizing Principle. *Science*, **327** (5961), 46–50.

20. Edidin, M. (2003) The State of Lipid Rafts: From Model Membranes to Cells. *Annu. Rev. Biophys. Biomol. Struct.*, **32** (1), 257–283.

21. Veatch, S.L., and Keller, S.L. (2002) Organization in Lipid Membranes Containing Cholesterol. *Phys. Rev. Lett.*, **89** (26), 268101.

22. Borden, M.A., Martinez, G.V., Ricker, J., Tsvetkova, N., Longo, M., Gillies, R.J., Dayton, P.A., and Ferrara, K.W. (2006) Lateral phase separation in lipid-coated microbubbles. *Langmuir*, **22** (9), 4291–4297.

23. Chattaraj, R., Mohan, P., Besmer, J.D., and Goodwin, A.P. (2015) Selective Vaporization of Superheated Nanodroplets for Rapid, Sensitive, Acoustic Biosensing. *Adv. Healthc. Mater.*, **4** (12), 1790–1795.

24. Dayton, P.A., Zhao, S., Bloch, S.H., Schumann, P., Penrose, K., Matsunaga, T.O., Zutshi, R., Doinikov, A., and Ferrara, K.W. (2006) Application of Ultrasound to Selectively Localize Nanodroplets for Targeted Imaging and Therapy. *Mol. Imaging*, **5** (3), 7290.2006.00019.

25. Zhou, Y., Wang, Z., Chen, Y., Shen, H., Luo, Z., Li, A., Wang, Q., Ran, H., Li, P., Song, W., Yang, Z., Chen, H., Wang, Z., Lu, G., and Zheng, Y. (2013) Microbubbles from Gas-Generating Perfluorohexane Nanoemulsions for Targeted Temperature-Sensitive Ultrasonography and Synergistic HIFU Ablation of Tumors. *Adv. Mater.*, **25** (30), 4123–4130.

26. Luke, G.P., Hannah, A.S., and Emelianov, S.Y. (2016) Super-Resolution Ultrasound Imaging in Vivo with Transient Laser-Activated Nanodroplets. *Nano Lett.*, **16** (4), 2556–2559.

27. Jian, J., Liu, C., Gong, Y., Su, L., Zhang, B., Wang, Z., wang, D., Zhou, Y., Xu, F., Li, P., Zheng, Y., Song, L., and Zhou, X. (2014) India Ink Incorporated Multifunctional Phase-transition Nanodroplets for Photoacoustic/Ultrasound Dual-modality Imaging and Photoacoustic Effect Based Tumor Therapy. *Theranostics*, **4** (10), 1026–1038.

28. Vannan, M.A., and Kuersten, B. (2000) Imaging Techniques for Myocardial Contrast Echocardiography. *Eur. J. Echocardiogr.*, **1** (3), 224–226.

29. Nakatsuka, M.A., Hsu, M.J., Esener, S.C., Cha, J.N., and Goodwin, A.P. (2011) DNA-Coated Microbubbles with Biochemically Tunable Ultrasound Contrast Activity. *Adv. Mater.*, **23** (42), 4908–4912.

30. Bach, D., and Wachtel, E. (2003) Phospholipid/cholesterol model membranes: formation of cholesterol crystallites. *Biochim. Biophys. Acta BBA - Biomembr.*, **1610** (2), 187–197.

31. Veatch, S.L., and Keller, S.L. (2003) Separation of Liquid Phases in Giant Vesicles of Ternary Mixtures of Phospholipids and Cholesterol. *Biophys. J.*, **85** (5), 3074–3083.

32. Rapoport, N., Gao, Z., and Kennedy, A. (2007) Multifunctional Nanoparticles for Combining Ultrasonic Tumor Imaging and Targeted Chemotherapy. *JNCI J. Natl. Cancer Inst.*, **99** (14), 1095–1106.

33. Wang, Z., and Yang, S. (2008) Adsorption Behaviors of DPPC/MO Aggregates on SiO2 Surfaces. *Langmuir*, **24** (20), 11616–11624.

34. Shaikh, S.R., Dumaual, A.C., Jenski, L.J., and Stillwell, W. (2001) Lipid phase separation in phospholipid bilayers and monolayers modeling the plasma membrane. *Biochim. Biophys. Acta BBA - Biomembr.*, **1512** (2), 317–328.

35. Anton, N., Pierrat, P., Lebeau, L., F. Vandamme, T., and Bouriat, P. (2013) A study of insoluble monolayers by deposition at a bubble interface. *Soft Matter*, **9** (42), 10081–10091.

36. Nicolas, J.-P., Lin, Y., Lambeau, G., Ghomashchi, F., Lazdunski, M., and Gelb, M.H. (1997) Localization of Structural Elements of Bee Venom Phospholipase A2 Involved in N-type Receptor Binding and Neurotoxicity. *J. Biol. Chem.*, **272** (11), 7173–7181.

37. Dong, Z., Liu, Y., Scott, K.F., Levin, L., Gaitonde, K., Bracken, R.B., Burke, B., Zhai, Q.J., Wang, J., Oleksowicz, L., and Lu, S. (2010) Secretory phospholipase A2-IIa is involved in prostate cancer progression and may potentially serve as a biomarker for prostate cancer. *Carcinogenesis*, **31** (11), 1948–1955.

38. Kupert, E., Anderson, M., Liu, Y., Succop, P., Levin, L., Wang, J., Wikenheiser-brokamp, K., Chen, P., Pinney, S.M., Macdonald, T., Dong, Z., Starnes, S., and Lu, S. (2011) Plasma secretory phospholipase A2-IIa as a potential biomarker for lung cancer in patients with solitary pulmonary nodules. *BMC Cancer*, **11**, 513.

39. Chapman, R., Lin, Y., Burnapp, M., Bentham, A., Hillier, D., Zabron, A., Khan, S., Tyreman, M., and Stevens, M.M. (2015) Multivalent Nanoparticle Networks Enable Point-of-Care Detection of Human Phospholipase-A2 in Serum. *ACS Nano*, **9** (3), 2565–2573.

Chapter 5. Interfacial Influence of Lipids, Polymers, and Proteins on Liquid Crystal Orientation in Phospholipid-Coated Emulsions: Applications in Phospholipase A_2 Sensing

5.1. Abstract

This work describes alignment of liquid crystals in phospholipid-coated emulsions as a function of lipid acyl chain length and ambient proteins. The ability of liquid crystals (LCs) to align in response to molecular interactions at the aqueous-LC interface has led to investigations into surface and emulsion-based biomolecular detection platforms. However, the sensitivity of droplet LC alignment to interfacial composition makes these droplets vulnerable to false positives via nonspecific binding, along with instability due to droplet coalescence. Phospholipids and lipopolymers are known to provide resistance to non-specific protein adsorption. Based on the observations with the phospholipid-stabilized droplets used in this study, we hypothesize that the packing of lipids in the droplet shell is an important determinant of LC orientation, with a liquid-phase monolayer allowing for a radial orientation. In accordance with this hypothesis, DLPC (C14) and DPPC (C16) produced predominantly radial droplets, while previously unexplored long-chain lipids like DSPC (C18) and DBPC (C22) produced non-radial (predominantly bipolar) droplets. However, adding low melting lipids such as DOPC (C18:1) to DSPC produced predominantly radial emulsions. Moreover, addition of excess poly(ethylene glycol) to the monolayer left the LC alignment mostly unchanged, in contrast to previous studies on planar surfaces. While, non-specific proteins like BSA, lysozyme, and fibrinogen were found not to affect LC alignment significantly, interaction with C18 DSPC-coated droplets by phospholipase A_2 significantly transitioned non-radial droplets into radial, providing a different mechanism of LC transition than

other studies showing the reverse transition for short-chain DLPC droplets. This report provides a framework for the design of stable, lipid-coated LC emulsions for tuning the encapsulated LC orientation as desired.

5.2. Introduction

Because thermotropic liquid crystals (LC) are able to change their alignment based on adsorption of surfactants, their utility as an indicator for biomolecules has been explored extensively over the past several years[1]. First, the inherent property of LC birefringence allows for different optical appearances of LC orientation under cross-polarized light. Usually, at the interface between a low molecular weight LC and an aqueous phase, the native LC orientation is planar; *i.e.* the LC director is aligned parallel to the interface[2]. Upon adsorption of certain types of surfactants, the orientation of a LC can transition to homeotropic; *i.e.*, the LC director is aligned perpendicular to the interface[3]. Similarly, specific binding of proteins has been utilized to alter the LC orientation at surfactant-covered aqueous-LC interfaces[2,4,5]. Such observations pertaining to the change of LC orientation based on interfacial composition at the surface have led to applications in protein detection via direct LC transition[6] or through DNA-hybridization mediated LC reorientation[7,8]. detection of nucleic acids[9]. detection of heavy metal ions[10], and glucose sensing[11], among others.

LC emulsions represent an opportunity for rapid biomolecular detection due to reduced analyte diffusion time. Because the emulsion interface is curved rather than planar, the terminology of LC orientation is slightly different. In one case, the LC may align completely in the "radial" direction, or normal to the interface. Alternatively, the LC may align without radial symmetry (*e.g.,* with axial symmetry), giving rise to a "bipolar" configuration (see below). In previously reported studies, analyte adsorption to the interface has been shown to cause an LC transition from radial

to bipolar, or vice versa[12–22]. Most notably, Abbott and co-workers showed the direct detection of low concentrations (on the order of pg/mL) of bacterial endotoxin[21]. However, in practice, LC-in-water droplets without any stabilizing shell material should coalesce within a few hours or less[21,22]. Surfactants like CTAB have been used on LC emulsions to sense bile acids[18,19] and cancer cells[20], but such surfactants with a high critical micelle concentration adsorb at the interface reversibly, resulting in emulsions with relatively low stability. Polymer-shelled emulsions have also been used to detect analytes like glucose[12] and IgG[13,14], to differentiate between various types of bacteria and viruses,[15] and to adhere to cells for reporting of toxic environmental agents[17]. While crosslinked polymer-shelled emulsions are usually resistant to rapid ripening and/or coalescence, they require time and expertise to prepare[23].

This work reports the effect of phospholipid monolayers on LC emulsions as a general platform for in-solution biosensing. Phospholipid shelled nano- and microparticles are known to be highly stable and biocompatible[24,25], and adding a lipopolymer like DSPE-PEG to the shell affords stability from days to weeks[26]. In addition, longer fatty acid tails are known to provide greater lipid stability and residence time in an emulsion monolayer[27]. However, phospholipids are not simply innocent bystanders in these biosensing technologies, as surfactant tail length also appears to have a large effect on LC orientation: a short-chain surfactant like OTAB (eight carbon atoms in the chain: C8) preserves a planar LC alignment at a surface, whereas the longer DTAB (C12) and CTAB (C16) produce a homeotropic alignment[28]. Low-melting point phospholipids like DLPC, DPPC, and DOPC (C18:1) also induce a homeotropic LC orientation[18,21,22]. On the other hand, phospholipids with a higher melting temperature, like DSPC and DBPC, have not been studied in this context. On surfaces, previous studies have posited that a surface containing L-DPPC or L-DLPC between liquid crystal forming 4-cyano-4′-pentylbiphenyl (5CB) and aqueous

media will undergo transition of the LC orientation from homeotropic to planar in 1-2 h upon binding of specific proteins like phospholipase[2,4] and neutravidin[2]. However, non-specific adsorption of proteins like albumin, cytochrome-c, and lysozyme, at a 1 μM concentration, apparently does not alter the 5CB arrangement[4]. Similar studies have so far not been conducted for the aqueous-LC interface in lipid-coated droplets. In this paper, we sought to tune LC orientation in such emulsions by altering lipid composition, structure, and packing in the monolayer of droplets formed by actively incorporating lipids into the shell. This study provides a means to not only distinguish the behavior of phospholipids on LC emulsions with those on LC surfaces, but also to detail how to design LC emulsions for in-solution biosensing through interactions with intended proteins and resistance to the effects of nonspecific binding.

5.3. Experimental Section

5.3.1. Materials. All phospholipids and their derivatives, including DLPC, DPPC, DSPC, DBPC, DOPC, DSPE-PEG2000, DSPE-PEG5000, and DSPE-PEG2000-Biotin (see *Abbreviations*), were purchased from Avanti Polar Lipids, Inc. (Alabaster, AL). 4-Cyano-4′-pentylbiphenyl (5CB) was obtained from TCI America (Portland, OR). Ethylenediaminetetraacetic acid (EDTA), NHS-Rhodamine, streptavidin, and fetal bovine serum (FBS) were purchased from ThermoFisher Scientific. Bovine serum albumin (BSA) was purchased from US Biological (Salem, MA). Lysozyme (from chicken egg white), fibrinogen (from human plasma), phospholipase A_2 from honey bee venom (*Apis mellifera*), and $CaCl_2.2H_2O$ were procured from Sigma Aldrich (St. Louis, MO). Chloroform, from Fisher Scientific (Pittsburgh, PA), and Tris buffered saline (TBS, 25 mM Tris base, 137 mM NaCl, pH 7.4) from Quality Biological Inc. (Gaithersburg, MD), were also used.

5.3.2. Formulation and Incubation of Nanodroplets. Hydrated phospholipid stocks of DLPC, DPPC, DSPC, DBPC, DSPC/DOPC, and subsequent lipid-DSPE-PEG solutions, were prepared in TBS according to a general procedure as described previously[24,26]. The concentration of phospholipid was maintained at approximately 1.3 mM, which translates into 1 mg/mL for DPPC. Liquid crystal emulsions were formed by probe-sonication (Branson SLPe, Branson Ultrasonics, Danbury, CT) of 20 μL 5CB in 980 μL of a 96:4 (mole %) phospholipid:DSPE-PEG solution at room temperature. Each sonication cycle was carried out at a 2 min cycle of 1 s on–9 s off bursts at 70% amplitude. For biotin-streptavidin experiments, 1 mol% DSPE-PEG-Biotin was used along with 3 mol% DSPE-PEG2000 to make a combined 4 mol% DSPE-PEG. The emulsions were then subjected to centrifugation at 1600 *g* for 1 min. The supernatant was recovered and centrifuged at 6000 *g* for 4.5 min, followed by centrifuge-washing under the same conditions. The pellet was then resuspended in TBS.[26] Size distribution and concentration of 5CB droplets were measured via Nanoparticle Tracking Analysis (NTA) using a NanoSight LM10 setup (Malvern Instruments Ltd., WR, United Kingdom). For interaction of different proteins with droplets, samples containing approximately $1x10^9$-$5x10^9$ droplets were incubated with the proteins to a final volume of 100 μL at room temperature. All samples were prepared in TBS at pH 7.4, unless specified otherwise.

5.3.3. Preparation of Fluorescently Labeled BSA and Adsorption to Droplets. To each mL of a 10 mg/mL solution of BSA in 50 mM $NaHCO_3$ buffer (pH ~8.5), 100 uL of 1 mg/mL NHS-Rhodamine was added dropwise while stirring, and the reaction was stirred for 2 h on ice. Following this, the product was centrifuged and washed using a 30k MWCO filter, followed by resuspension in TBS. To test the adsorption of albumin onto 5CB droplets, droplets were

incubated in a total volume of 0.5 mL in TBS with 1 μM rhodamine-BSA at RT. The droplets were then centrifuged and the pellet washed four times with TBS at 6000 *g* for 4.5 min: the resultant pellet was resuspended in TBS before fluorescent imaging.

5.3.4. Imaging of Nanodroplets and Analysis. 8 μL of a 5CB droplet suspension in TBS was placed between a fresh slide and a coverslip and imaged between cross polarizers of a Zeiss Axio Imager A2 to obtain polarization images. Bright-field images were captured without the analyzer in place. Fluorescent microscopy was conducted using the same microscope in an epifluorescence mode through a red emission channel.

The polarization images were then analyzed by first thresholding the image and then counting the total number of droplets using ImageJ (NIH). To quantify the fraction of radial droplets reported below, each droplet was assigned a category (radial or non-radial, where the latter included mostly bipolar and some pre-radial droplets) based on its appearance **(Figure 5.1A)** and counted manually, thus providing the fraction of radial droplets in each image. This procedure is consistent with previous reports by others[18,21,22]. It should also be noted that these measurements were taken at equilibrium, so there is no information about the transition itself. For images showing no clear non-radial droplets, a 100% radial droplet fraction was considered. Error bars for each data point in each plot with '% Radial droplets' on the y-axis represent one standard deviation for 3-6 polarization images, each containing between 40-400 droplets, over multiple experiments analyzed for the respective sample.

5.3.5. Flow Cytometry of Nanodroplets and Analysis. obtain flow cytometry plots of side scatter vs forward scatter (SSC vs FSC), approximately $1x10^7$-$5x10^7$ droplets (100 times more diluted

than a microscopy image sample) in a total volume of 0.5 mL were used for measurements. All such samples were analyzed using a Accuri C6 Plus flow cytometer (BD Biosciences) at 50000 events recorded at a flowrate of 14 μL per min.

5.4. Results

5.4.1. Formulation and Characteristics of LC droplets. The droplets in this study are mostly in the sub-micron range with a packed lipid monolayer, chosen for their prolonged stability, ease of synthesis by probe sonication, and simple identification of LC phases by polarized light microscopy. LC droplets **(Figure 5.1B)** were composed of 5CB, a common thermotropic liquid crystal **(Figure 5.1C),** and stabilized by a combination of phospholipid (**Figure 5.1D**) and 4 mol% DSPE-PEG, without which the droplets would be prone to aggregation and/or coalescence.[24]

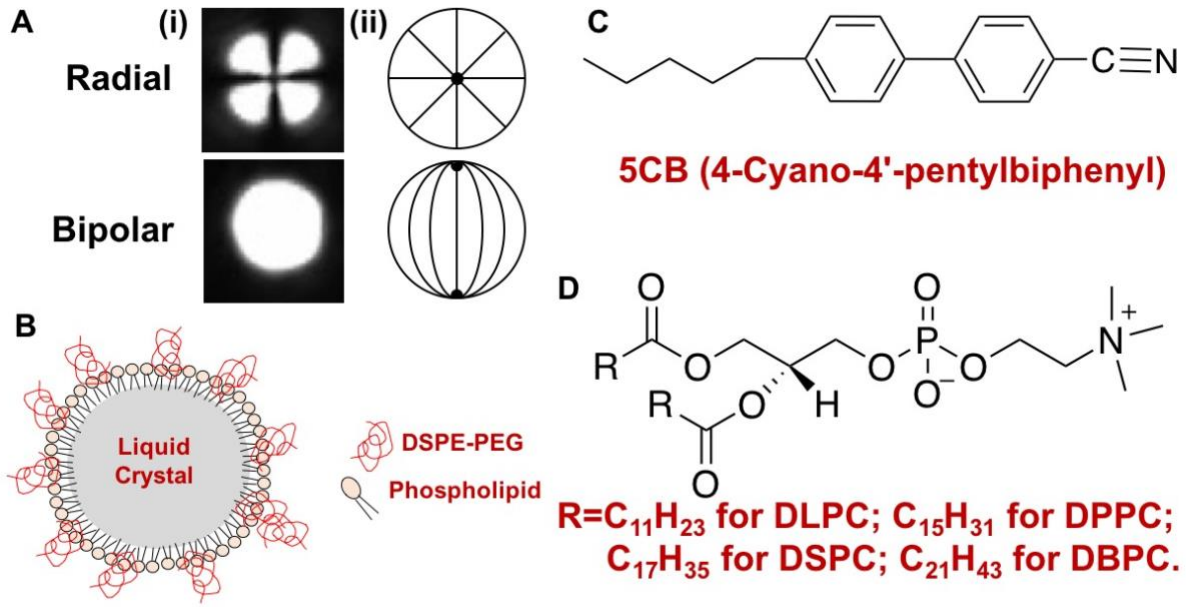

Figure 5.1. **A**. Polarized light microscopy images **(i)** of representative droplets with radial and bipolar orientations of 5CB, along with corresponding schematic illustrations **(ii)**. **B.** Schematic of

a lipid-coated liquid crystal droplet. **C.** Structure of 5CB. **D.** Structure of various saturated phospholipids used for the present study.

Following probe sonication, the droplets had a mean size ranging between 300-400 nm as measured by Nanoparticle Tracking Analysis (NTA) (**Figure 5.2**). Due to the limits of NTA for detecting larger particles, droplets above 1.5-2 μm were not counted by this method. However, previous reports have shown that sizes below 5-10 μm should not affect LC orientation, as the lipids in the shell are at a near-saturation coverage[16,29].

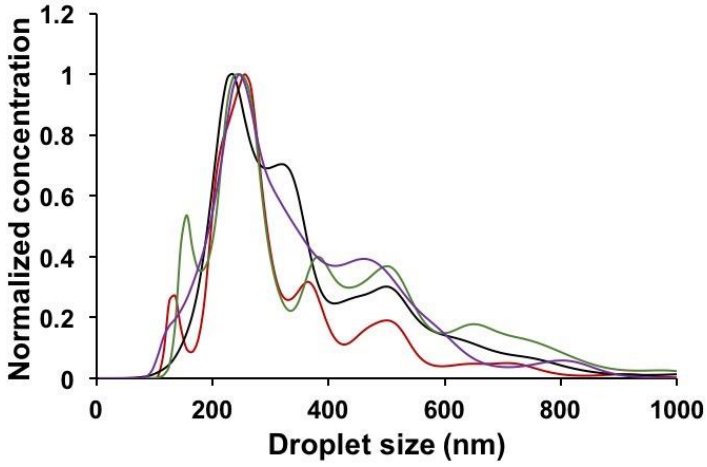

Figure 5.2. Size distribution of DLPC (*red*), DPPC (*black*), DSPC (*green*), and DBPC (*purple*) nanodroplets with a 5CB core, as measured via nanoparticle tracking analysis (NTA).

5.4.2. Effect of Phospholipid Acyl Chain Structure on LC Orientation. To study the effect of acyl chain length, emulsions with 5CB cores were prepared with DLPC (C12:0), DPPC (C16:0), DSPC (C18:0), or DBPC (C22:0) as the primary lipid component in their shell **(Figure 5.1D)**. For emulsions containing approximately 1 mg/mL of short-chained lipids (DLPC and DPPC), the LC orientation was found to be radial, analogous to a homeotropic alignment on surfaces. However,

as the chain length increased from C16:0 to C18:0, the orientation of emulsions abruptly transitioned from radial (homeotropic) to mostly non-radial (planar) (**Figure 5.3A** and **5.3B**). We attribute this change to increased packing of the DSPC and DBPC monolayers owing to increased van der Waals interactions with increase in each $–CH_2$ group in the acyl chain of a phospholipid. Assuming 2D hexagonal packing of acyl chains in a monolayer, the increase in cohesive energy between two acyl chains from DPPC (C16:0) to DBPC (C22:0) has been shown to be almost 50%[30].

Characterization of LC alignment within emulsions is usually performed, as done here, with polarization optical microscopy. More recently, flow cytometry was shown to offer another means to characterize these droplets by comparing the anisotropy of light scattering by aligned LC emulsions with the approximately isotropic light scattering by radial emulsions. The result, as shown by Abbott and coworkers, is that bipolar droplets exhibit a broad distribution of SSC for each FSC, whereas radial droplets have a much narrower distribution[31].

Here, flow cytometry experiments were conducted for each lipid set, and scatterplots of side scatter vs forward scatter (SSC vs FSC) were generated for each sample. The scatterplot of DLPC and DPPC droplets show a narrow distribution, which confirms the primarily radial orientation, while broader scattering dependence for DSPC and DBPC droplets indicates a non-radial orientation (**Figure 5.3C**). Using this technique, it was also found that phospholipid-shelled LC droplets remained stable and retained their LC orientation ranging from days to weeks (**Figure 5.4**).

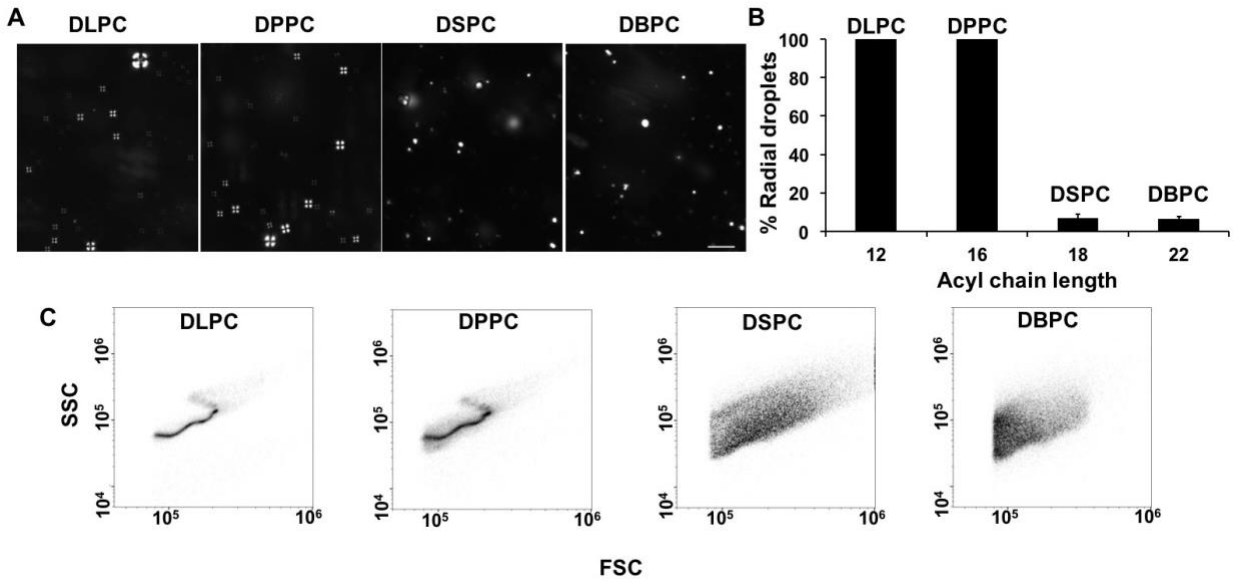

Figure 5.3. A. Polarized light microscopy images of 5CB droplets with different phospholipid compositions in the monolayer (each containing 4 mol% DSPE-PEG2000 along with the primary lipid/s component). Scale bar: 5 μm. **B.** 5CB orientation in DLPC, DPPC, DSPC, and DBPC droplets. **C.** Flow cytometry scatterplots for DLPC, DPPC, DSPC, and DBPC droplets. FSC = forward scatter; SSC = side scatter.

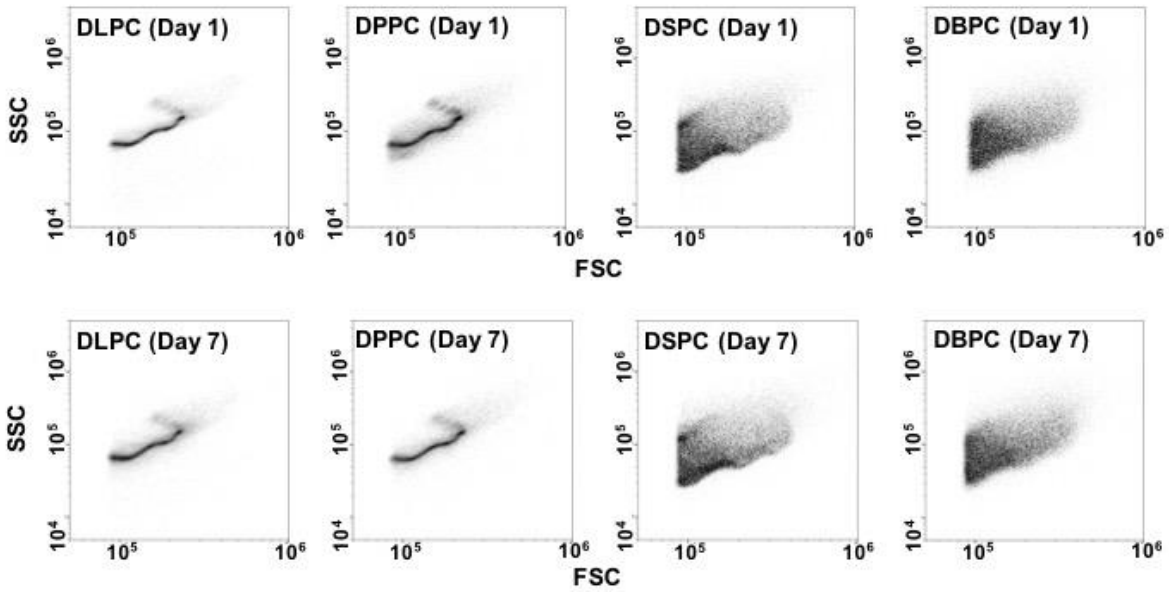

Figure 5.4. Flow cytometry scatter plots of the same DLPC, DPPC, DSPC, and DBPC droplet samples just after (Day 1) and a week after (Day 7) preparation. Droplets were stored at 4^0C.

Because the LC alignment appeared to depend on melting temperature of the encapsulating lipid, adding low-melting, unsaturated lipids to a bipolar droplet would likely cause transition back to radial. To test this hypothesis, DOPC was mixed in different ratios with DSPC in the monolayer. As can be seen from **Figure 5.5**, as DOPC concentration increased from 1 to 25 mol% relative to DSPC, the fraction of emulsions with radial LC orientation increased as well. Again, flow cytometry confirmed this result, in which a 75:25 mol% DSPC:DOPC formulation produced droplets with similar distribution as for a DPPC sample (**Figure 5.5C, Figure 5.6, Figure 5.7**). The unsaturated DOPC likely disrupts the packing in the gel phase, which allows the LC to interact with the lipid tails and the LC to adopt a radial conformation

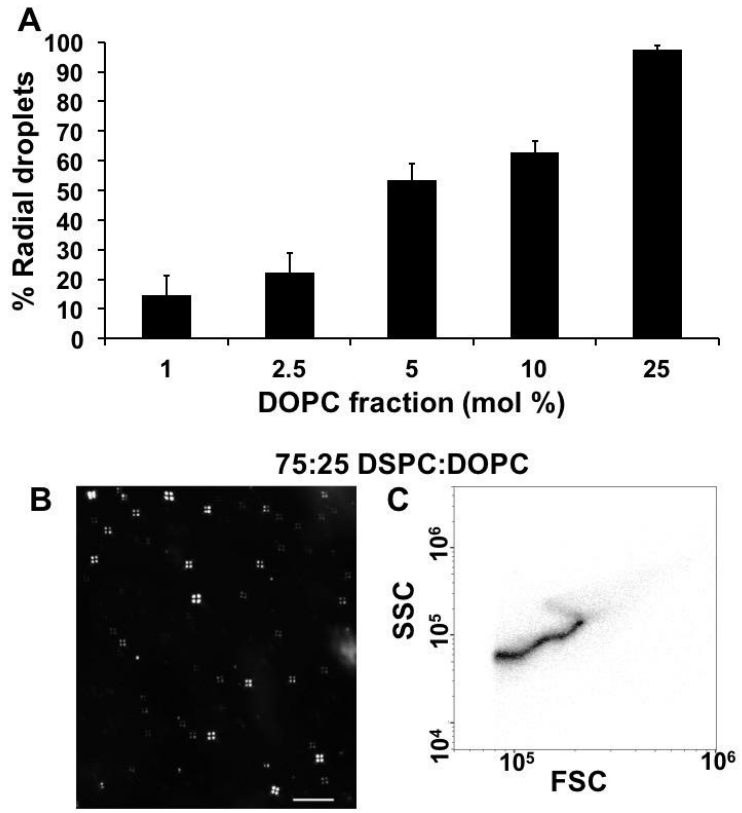

F**igure 5.5. A.** 5CB orientation in droplets containing different ratios of DSPC:DOPC in the monolayer (each containing 4 mol% DSPE-PEG2000). **B-C.** 5CB droplets with 75:25 mol% DSPC:DOPC in the monolayer exhibit a largely radial orientation as seen through polarized light microscopy (**B**) and flow cytometry (**C**).

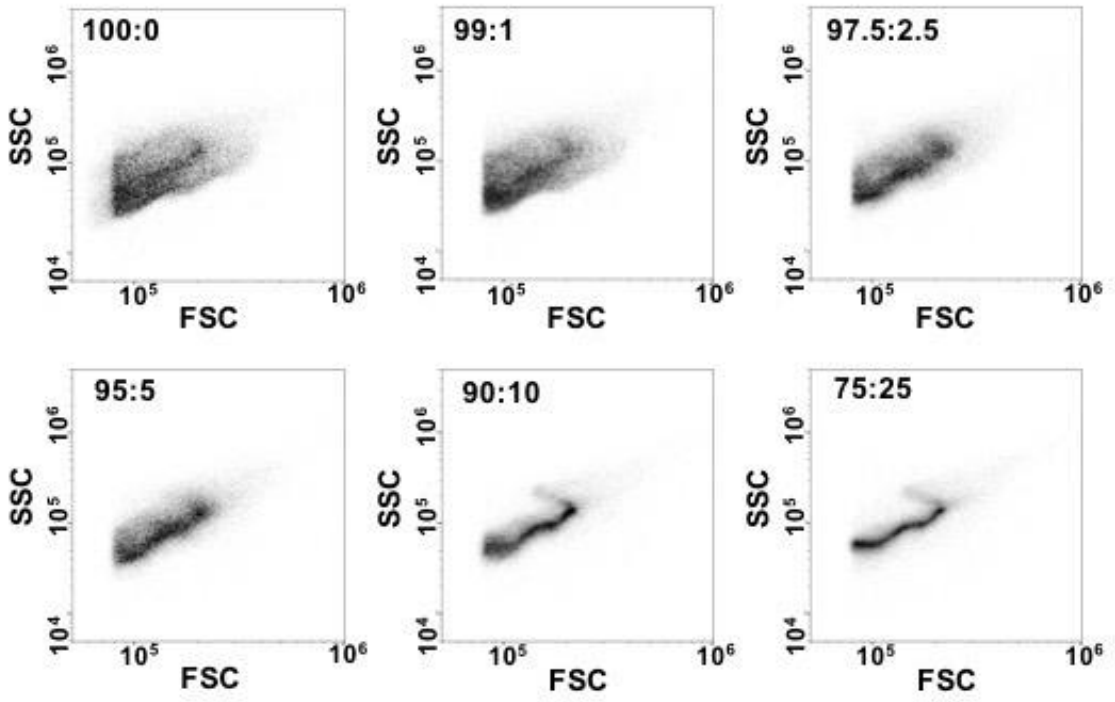

Figure 5.6. Flow cytometry scatter plots of 5CB droplets with different ratios of DSPC:DOPC (0, 1, 2.5, 5, 10, and 25 mol% DOPC) in their monolayers (each composition contains 4 mol% DSPE-PEG2000). The droplets slowly transitioned from non-radial to radial as the DOPC fraction was increased.

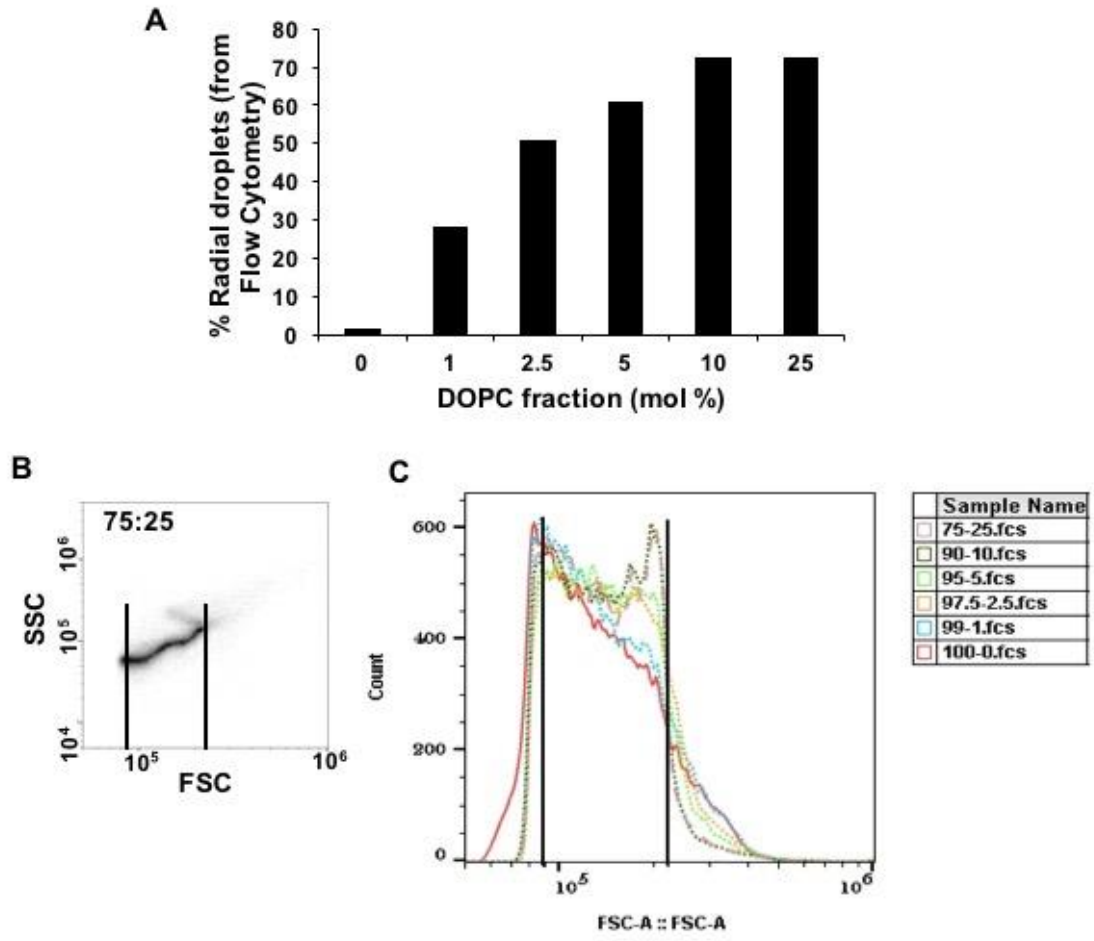

Figure 5.7. A. 5CB orientation in droplets containing different ratios of DSPC:DOPC in the monolayer, *as calculated from Flow Cytometry data*. **B.** Flow cytometry scatter plot of 75:25 DSPC:DOPC. **C.** Histogram representations of data from **Figure 5.6**. All lines are dotted except 100:0 (*solid*) and 75:25 (*dashed*). To corroborate the results from polarized light microscopy data (as presented in **Figure 5.5**), the % radial droplets was calculated using a similar method as detailed by Abbott and coworkers previously.[1] For radial droplets, the scatter plot has a distinct narrow shape, which usually stretches between FSC values of ~90,000 to ~230000. The number of droplets can be calculated as the area under the histogram of the scatter plot for each sample. The two vertical lines in **Figure 5.7B (**and **Figure 5.7C**) chart out the ~90,000-230,000 range over which the area under the curve is considered, while the histograms from DLPC (radial) and DBPC

(non-radial) scatter plots (**Figure 5.3C**) are taken as positive (completely radial) and negative (completely non-radial) controls respectively. Normalizing the area under each histogram in **Figure 5.7C** with these controls as maximum and minimum count values, the %Radial droplets is derived (**Figure 5.7A**).

5.4.3. Effect of PEG Loading on LC Phase. LC droplets and LC surfaces were found to behave differently as a function of poly(ethylene glycol) (PEG) concentration in the droplet shell. In this study, droplets were prepared with 4, 10, and 30 mol% DSPE-PEG2000 or DSPE-PEG5000, with the remaining fraction being the primary phospholipid. Analysis of both the polarized images (**Figure 5.8** and **Figure 5.9C)** and the representative flow cytometry scatterplots (**Figure 5.9A-B)** showed that increasing DSPE-PEG concentration up to even 30 mol% had only a marginal effect on the orientation of the LC in the droplets (**Figure 5.10**). In contrast, a previous study of LC orientation on planar surfaces[32] found that as little as 10 mol% DSPE-PEG2000 and 90% DPPC caused the formation of islands with planar (bipolar) configuration, and 30 mol% caused the whole LC to appear planar. We attribute this apparent difference to the curvature of the droplets, which provides more space for the PEG brush without necessarily changing the lipid packing on the LC interface.

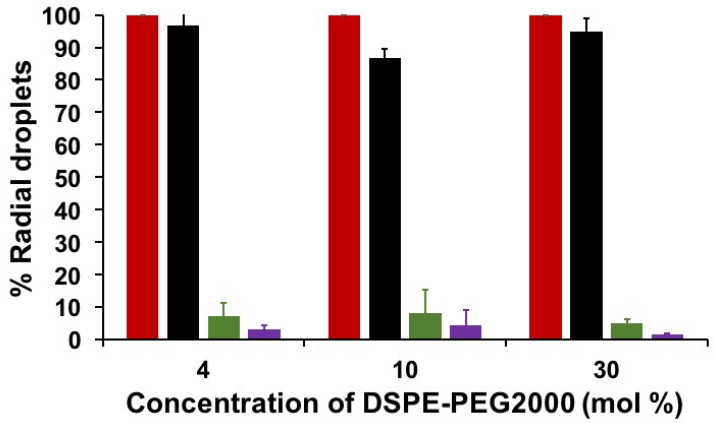

Figure 5.8. 5CB orientation in DLPC (*red*), DPPC (*black*), DSPC (*green*), and DBPC (*purple*) droplets with 4, 10, and 30 mol% DSPE-PEG2000.

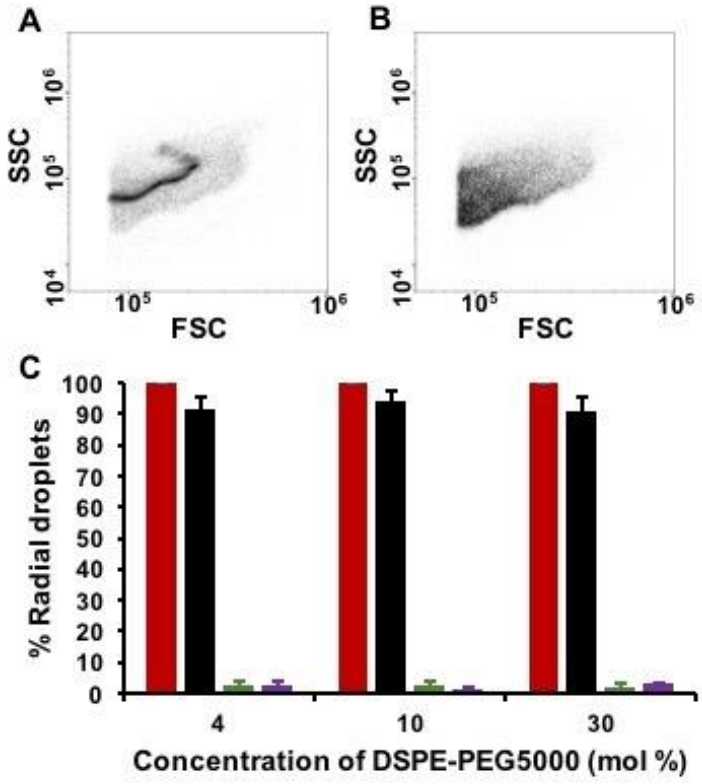

Figure 5.9. A-B. Flow cytometry scatter plots of DLPC (**A**) and DSPC (**B**) droplets with 30 mol% DSPE-PEG2000. **C.** 5CB orientation in DLPC (red), DPPC (black), DSPC (green), and DBPC (purple) droplets with 4, 10, and 30 mol% DSPE-PEG5000.

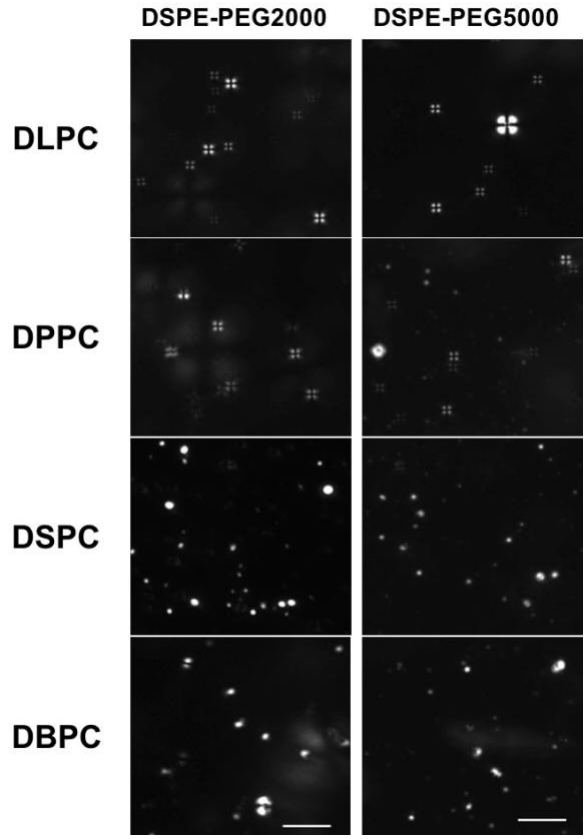

Figure 5.10. Polarized light microscopy images of 5CB droplets with 30 mol% DSPE-PEG. Scale bar: 5 μm.

5.4.4. Nonspecific Protein Interactions. Because rapid biomolecular assays represent a primary application for LC-in-water droplets, the effect of nonspecific protein interactions on LC alignment should be determined to predict the effects of complex sample media such as serum, plasma, or whole blood. As test proteins, bovine serum albumin (BSA, MW ~ 66 kDa, pI ~ 4.8) and lysozyme (MW ~ 15 kDa, pI ~11) were chosen as model proteins because of their ubiquity and different ionizations at pH 7.4. DLPC, DPPC, DSPC, and DBPC droplets were separately incubated with 1 μM of each non-specific protein for 1 h and imaged under cross-polarized light. The results

indicate (**Figure 5.11A, Figure 5.12**) that challenge with either protein had little effect on 5CB orientation, with deviations less than 10-15% from those measured without protein. However, a larger change was observed for binding of the large plasma protein fibrinogen (FBG, 340 kDa, pI ~ 4.8), from about 100% radial for DPPC without FBG to ~81% radial with FBG. It is possible that the multivalent binding of FBG to the phosphate groups in the lipids interferes with lipid packing. To verify whether proteins were retained on the emulsion shell, emulsions with different lipid monolayers were incubated with BSA-labelled with rhodamine for 1 h, followed by centrifuge washing **(Figure 5.11B)**. While retention was generally small, retention decreased with increasing chain length from DPPC to DBPC, corresponding to the magnitude of net change in 5CB orientation transition. Interestingly, DLPC droplets showed no fluorescence at all, indicating negligible retention of BSA, though this may be due to the short-chained (C12) DLPC leaving the monolayer and binding to the BSA in solution.

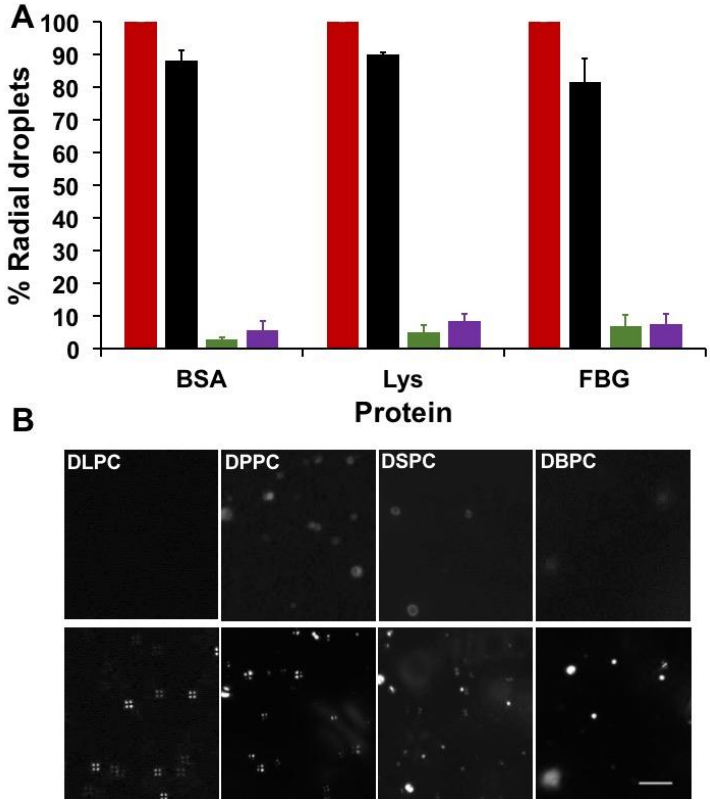

Figure 5.11. A. 5CB orientation in DLPC (*red*), DPPC (*black*), DSPC (*green*), and DBPC (*purple*) droplets incubated with 1 μM bovine serum albumin (BSA), lysozyme (Lys), and fibrinogen (FBG) for 1 h. (See Figure 1B for comparison with droplets without any proteins). **B.** Fluorescent (*top*) and polarization (*bottom*) images of 5CB droplets (from left to right: DLPC, DPPC, DSPC, DBPC) incubated with 1 μM rhodamine-BSA for 1hr, followed by centrifuge-washing. Scale bar: 5 μm.

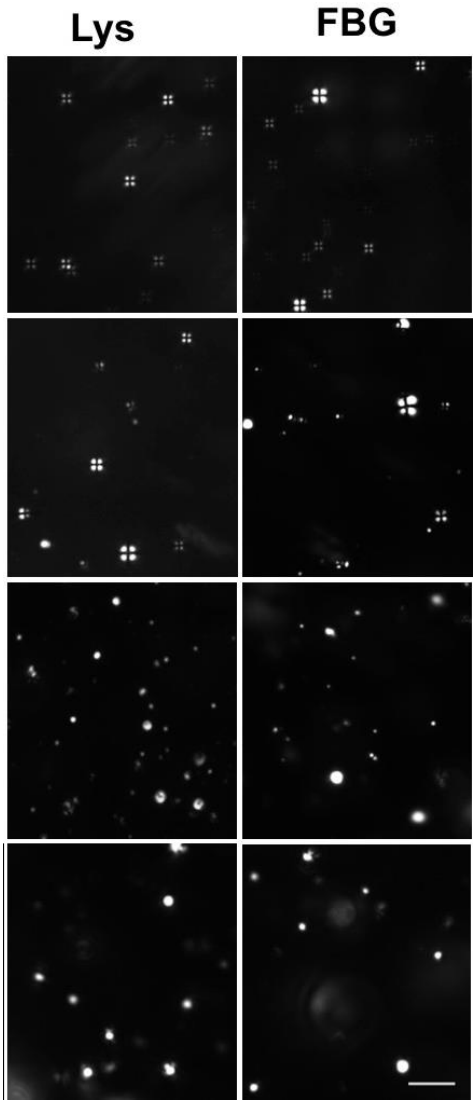

Figure 5.12. Polarized light microscopy images of 5CB droplets (*top to bottom:* DLPC, DPPC, DSPC, DBPC) incubated with 1 μM lysozyme (Lys) and fibrinogen (FBG) for 1 h. Scale bar: 5 μm.

5.4.5. Specific Protein Interactions. Having established that transition of orientation of 5CB in lipid-coated droplets was resistant to serum protein adsorption, we next tested interactions between two model proteins that would represent association with either the outer polymer brush or the lipid monolayer[4]. In the former case, streptavidin was chosen because it forms a very strong noncovalent bond (dissociation constant $K_d \sim 10^{-14}$ M) with biotin. By designing the emulsions to bind with the DSPE-PEG protruding out of the droplet shell, the streptavidin can be confined to the exterior of the shell. PLA_2, on the other hand, binds to phospholipids when it catalyzes the hydrolysis of the *sn*2 position of the phospholipid glycerol backbone, thus disrupting the organization of the lipid monolayer itself. Because it interacts with lipids and surfaces directly, PLA_2 has been detected via surface-based LC based platforms[33–35], along with a study by Abbott and coworkers that showed the effect of PLA_2 on LC droplet orientation for DLPC only[29]. Also, as mentioned in **Chapter 4.4.7**, PLA_2 can serve as a marker for snake venom poisoning and for certain types of cancers.

First, to test the effect of streptavidin (STV), droplets were formulated using 1 mol% DSPE-PEG2000-biotin in their shell[36], then incubated with 1 μM STV for 1 h. While the binding of STV was evident from droplet aggregation (**Figure 5.13**), the droplets in the aggregates appeared radial (DLPC, DPPC) or non-radial (DSPC, DBPC). Although these images could not be quantitatively analyzed due to the difficulty in accurately counting droplets in each aggregate,

qualitatively the LC orientation appears to be preserved even with STV binding.

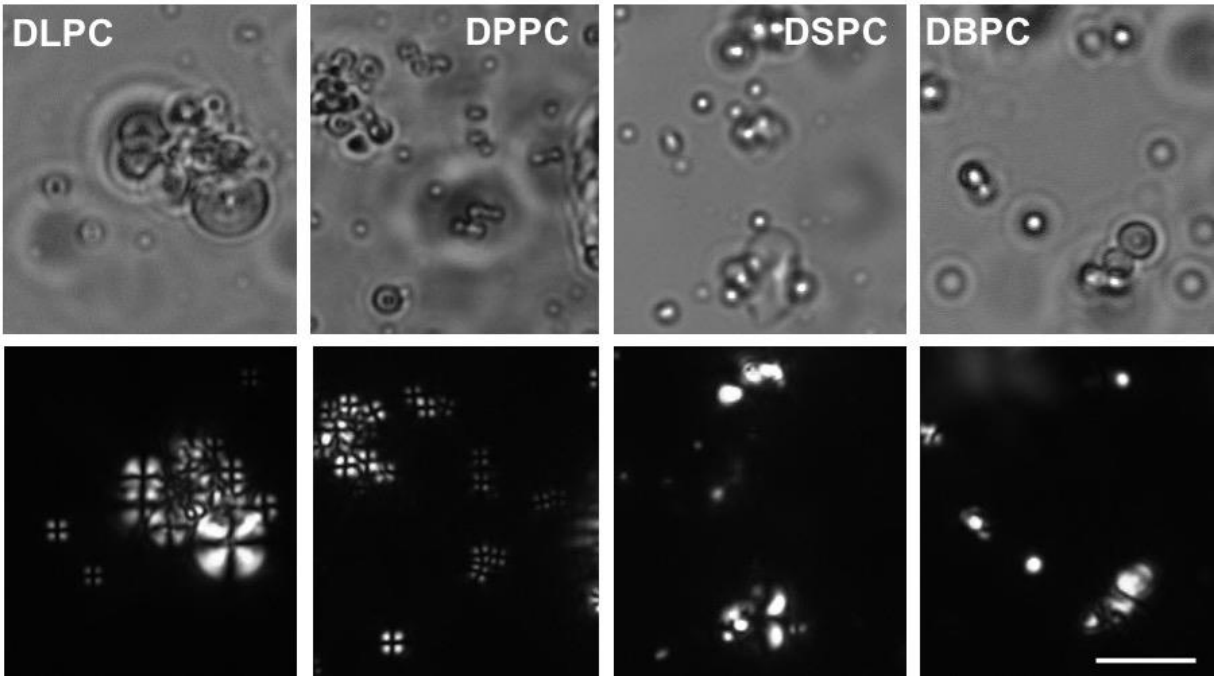

Figure 5.13. Bright field and polarization images of biotinylated 5CB droplets (from left to right: DLPC, DPPC, DSPC, DBPC) incubated with 1 μM streptavidin for 1h. Scale bar: 5 μm.

Next, 100 nM PLA_2 was mixed with 5CB droplets for 1 h in 5 mM Ca^{2+} at pH 8.9 before imaging **(Figure 5.14A)**. DLPC droplets transitioned to almost completely non-radial, while DPPC droplets transitioned partially. The sensitivity of this droplet detection system was approximately 10 nM PLA_2, though this value may be affected by droplet loading and size, and required 30-60 min to obtain full transition (**Figure 5.14B**). Near-full transition to non-radial was supported by diffuse flow cytometry side scatter vs. forward scatter plot (**Figure 5.14D**). In comparison, DLPC droplets with 100 nM PLA_2 in the presence of 5 mM EDTA (to bind with any free Ca^{2+}) did not show any transition to non-radial, indicating the necessity of Ca^{2+} for catalysis by PLA_2 (**Figure 5.15**). For DPPC, the smaller transition from radial to non-radial is probably due to the greater stability of longer chain lipids. The residence time of DLPC (C12:0) molecules in the monolayer is almost

100 times lower than that of DPPC (C16:0)[27], leading to considerably less desorption of DPPC lipid components than DLPC. DSPC droplets underwent a significant change from mostly non-radial droplets to an approximately 50% radial fraction (**Figure 5.14A)** in as little as 10 min with almost no time dependence. This result suggests that transition to radial was mediated by interaction rather than hydrolysis. The partial transition was supported by flow cytometry data, which shows the simultaneous presence of a dark narrow band (radial) and diffuse area (non-radial) on the scatterplot (**Figure 5.14E**). Finally, the DBPC gel-phase monolayer was not measurably affected by the enzyme. These studies were performed while controlling for the effects of both pH and Ca^{2+} addition, the results of which are summarized in **Figures 5.16-5.17.**

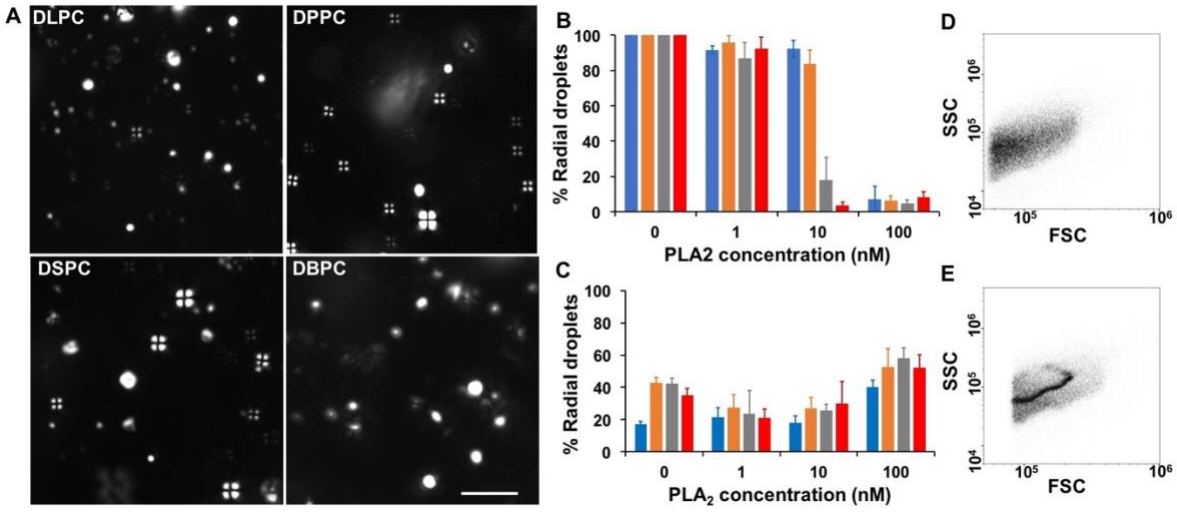

Figure 5.14. A. Polarized light microscopy images of 5CB droplets (from left to right: DLPC, DPPC, DSPC, DBPC) incubated with 100 nM PLA_2 in TBS with 5 mM Ca^{2+} at pH ~8.9 for 1hr. Scale bar: 5 μm. **B-C.** 5CB orientations in DLPC (**B**) and DSPC (**C**) droplets in TBS at pH 8.9 with 5 mM Ca^{2+} in the presence of different PLA_2 concentrations after 10 (*blue*), 30 (*orange*), 60 (*gray*), and 120 (*red*) min. **D-E.** Flow cytometry scatter plots of DLPC (**D**) and DSPC (**E**) droplets incubated with 100 nM PLA_2 in TBS at pH 8.9 with 5 mM Ca^{2+} for 60 min.

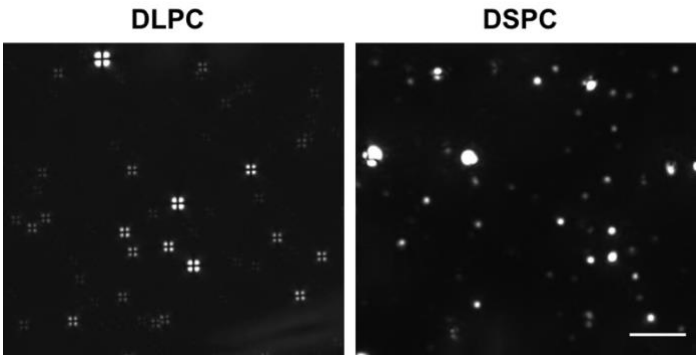

Figure 5.15. Polarized light microscopy images of 5CB droplets incubated with 100 nM phospholipase A_2 (PLA_2) for 1 h in the presence of 5 mM EDTA. Absence of Ca^{2+} prevents PLA_2 from causing 5CB orientation change. Scale bar: 5 μm.

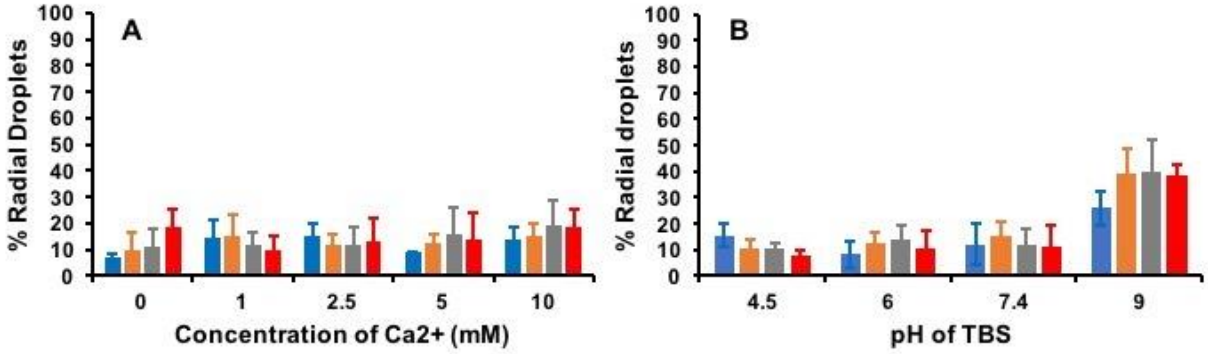

Figure 5.16. 5CB orientations in DSPC droplets in TBS after 10 (blue), 30 (orange), 60 (gray), and 120 (red) min (**A)** at pH 7.4 in the presence of different Ca^{2+} concentrations, and **(B)** at different values of pH with no Ca^{2+}.

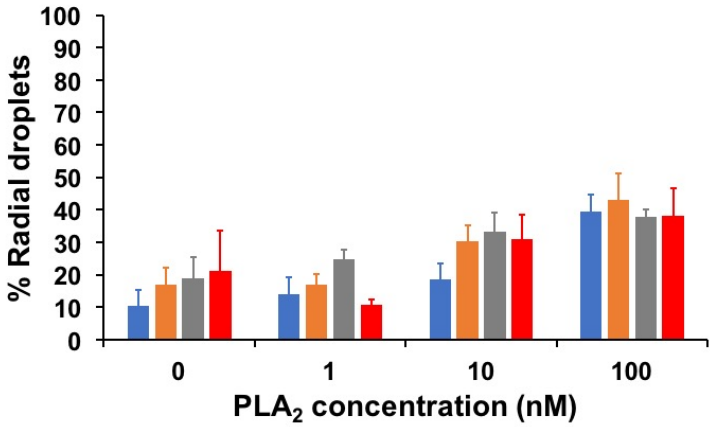

Figure 5.17. 5CB orientations in DSPC droplets in TBS at pH 7.4 with 5 mM Ca^{2+} in the presence of different PLA_2 concentrations after 10 (*blue*), 30 (*orange*), 60 (*gray*), and 120 (*red*) min.

5.5. Discussion

The current study presents the effects of lipid composition and protein interactions on phospholipid-stabilized liquid crystal emulsions. LC orientations in droplets with shorter-chain DLPC and DPPC monolayers were radial, while for previously unexplored longer-chained lipids like DSPC and DBPC shelled droplets, the alignment was non-radial (mostly bipolar). Incorporation of unsaturation in the form of DOPC in DSPC monolayers resulted in a drastic non-radial-to-radial transition. While it has been proposed that longer tails of lipids/surfactants should promote a radial, or homeotropic alignment[28], we hypothesize that fluidity of the lipid monolayer, which is related to acyl lipid chain length, is of considerable importance for LC orientation. Lipid tails of monolayers firmly in the gel phase at room temperature (DSPC, DBPC) do not appear to interact appreciably with LC mesogens, providing little driving force to break the

internal LC alignment. Conversely, a monolayer in a more liquid phase (DLPC, DPPC, DSPC with DOPC) can solvate the 5CB at the interface, allowing the LC molecules to align perpendicular to the interface in a radial fashion (**Figure 5.18**). Interestingly, an excess of PEG failed to affect LC orientation in any kind of droplets, indicating that droplet curvature appears to have a significant effect on LC behavior, leading to different results between planar and curved LC interfaces.

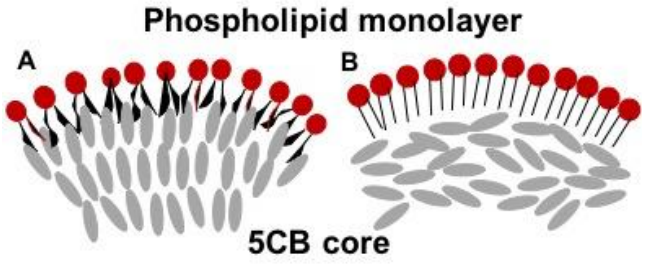

Figure 5.18. Schematic showing the alignment of 5CB molecules in the droplet core when the phospholipid monolayer is firmly in the liquid-expanded phase (**A**: DLPC, DPPC) and gel (**B**: DSPC, DBPC) phase.

The resistance of LC orientation to change in the presence of serum proteins makes lipid-coated emulsions a promising option for biosensing assays. This effect may be due in part to the PEG layer, which may be trapping nonspecifically-binding proteins away from the lipid monolayer, which is supported by the streptavidin binding studies. The lack of change in 5CB alignment stems from the STV not being able to penetrate between the lipid molecules in the monolayer and therefore not being able to significantly affect the lipid packing. However, previously reported studies showed that droplets with a biotinylated poly(acrylic acid) shell transitioned from radial to bipolar on binding with avidin[37]. In addition, surface studies have reported that neutravidin can cause a patterned distribution in biotinylated DLPC monolayers on a surface, with the protein-rich areas appearing tilted or planar[2]. In each of these cases, however, the biotin was connected directly to the interfacial component in contact with the LC, while in this work the flexible PEG

chain may serve as a way to keep proteins away from the sensitive monolayer. Proteins that bind specifically to the lipids, however, induce more dramatic changes in LC orientation. Phospholipase A_2 appeared to transition radial DLPC-coated droplets into largely bipolar, likely because lipid molecules desorb from the monolayer. To show the usefulness of LC droplets in biomarker assays, a proof-of-concept concentration study for PLA_2 allowed for the detection of the same by DLPC-5CB droplets via flow cytometry down to 0.1 nM (**Figure 5.19**). This preliminary framework for tuning LC orientation in lipid-coated nanodroplets may aid in the future design of stable and versatile systems for biomolecular detection.

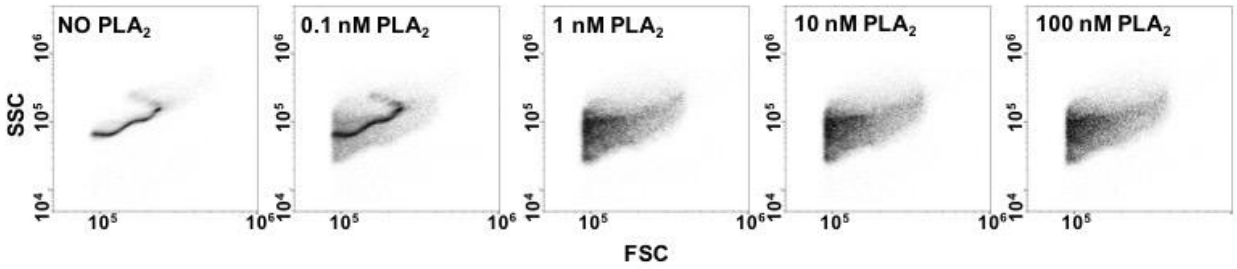

Figure 5.19. Flow cytometry scatter plots of DLPC droplets incubated with different amounts of PLA_2 in TBS at pH 8.9 with 5 mM Ca^{2+} for 30 min. Note that the detection limit for this study was 0.1 nM as opposed to 10 nM for polarized light microscopy (**Figure 5.14B**) since flow cytometry required a 100x more dilute sample than the one required for microscopy.

5.6. Conclusion

In summary, this study brings to light the following major observations for the first time:

- Monotonous increase of surfactant chain length at the aqueous-LC interface does not keep increasing the radial nature of droplets – membrane fluidity is as much a factor as acyl chain length.

- Unlike surfaces, addition of PEG at the interface for droplets does not change the orientation of LC in the internal phase.

- Lipid-cleaving proteins like PLA_2 do not just transition short chain lipid-coated interfaces from radial (homeotropic) to bipolar (planar). PLA_2 may also causes the reverse effect in case of longer chain lipids like DSPC at the interface, where the LC appearance instead changes from non-radial to radial.

This work thus presents the first example showing the interfacial dynamics and biosensing potential of long-chained lipids at the aqueous-LC interface. This preliminary framework for tuning LC orientation in lipid-coated nanodroplets may aid in the future design of stable and versatile systems for biomolecular detection.

5.7. Acknowledgement

This work was supported by NIH grants DP2EB020401 and R21EB018034. The authors thank Katherine M. Macri and Prof. Daniel K. Schwartz for initial training and suggestions on polarized light microscopy.

5.8. Abbreviations

DLPC: 1,2-dilauroyl-sn-glycero-3-phosphocholine; DPPC: 1,2-dipalmitoyl-sn-glycero-3-phosphocholine; DSPC: 1,2-distearoyl-sn-glycero-3-phosphocholine; DBPC: 1,2-dibehenoyl-sn-glycero-3-phosphocholine; DOPC: 1,2-dioleoyl-sn-glycero-3-phosphocholine; DSPE-PEG2000: 1,2-distearoyl-sn-glycero-3-phosphoethanolamine-N-[amino(polyethyleneglycol)-2000] (ammonium salt); DSPE-PEG5000: 1,2-distearoyl-sn-glycero-3-phosphoethanolamine-N-

[methoxy(polyethylene glycol)-5000] (ammonium salt); DSPE-PEG2000-Biotin:1,2-distearoyl-sn-glycero-3-phosphoethanolamine-N-[biotinyl(polyethylene glycol)-2000]. 5CB: 4-Cyano-4'pentylbiphenyl.

5.9. References.

1. Hussain, A., Pina, A.S., and Roque, A.C.A. (2009) Bio-recognition and detection using liquid crystals. *Biosens. Bioelectron.*, **25** (1), 1–8.

2. Brake, J.M., Daschner, M.K., Luk, Y.-Y., and Abbott, N.L. (2003) Biomolecular Interactions at Phospholipid-Decorated Surfaces of Liquid Crystals. *Science*, **302** (5653), 2094–2097.

3. Lockwood, N.A., and Abbott, N.L. (2005) Self-assembly of surfactants and phospholipids at interfaces between aqueous phases and thermotropic liquid crystals. *Curr. Opin. Colloid Interface Sci.*, **10** (3), 111–120.

4. Brake, J.M., and Abbott, N.L. (2007) Coupling of the Orientations of Thermotropic Liquid Crystals to Protein Binding Events at Lipid-Decorated Interfaces. *Langmuir*, **23** (16), 8497–8507.

5. Park, J.-S., and Abbott, N.L. (2008) Ordering Transitions in Thermotropic Liquid Crystals Induced by the Interfacial Assembly and Enzymatic Processing of Oligopeptide Amphiphiles. *Adv. Mater.*, **20** (6), 1185–1190.

6. Seo, J.-M., Khan, W., and Park, S.-Y. (2012) Protein detection using aqueous/ LC interfaces decorated with a novel polyacrylic acid block liquid crystalline polymer. *Soft Matter*, **8** (1), 198–203.

7. Price, A.D., and Schwartz, D.K. (2008) DNA Hybridization-Induced Reorientation of Liquid Crystal Anchoring at the Nematic Liquid Crystal/Aqueous Interface. *J. Am. Chem. Soc.*, **130** (26), 8188–8194.

8. Noonan, P.S., Mohan, P., Goodwin, A.P., and Schwartz, D.K. (2014) DNA Hybridization-Mediated Liposome Fusion at the Aqueous Liquid Crystal Interface. *Adv. Funct. Mater.*, **24** (21), 3206–3212.

9. Noonan, P.S., Roberts, R.H., and Schwartz, D.K. (2013) Liquid Crystal Reorientation Induced by Aptamer Conformational Changes. *J. Am. Chem. Soc.*, **135** (13), 5183–5189.

10. Yang, S., Wu, C., Tan, H., Wu, Y., Liao, S., Wu, Z., Shen, G., and Yu, R. (2013) Label-Free Liquid Crystal Biosensor Based on Specific Oligonucleotide Probes for Heavy Metal Ions. *Anal. Chem.*, **85** (1), 14–18.

11. Khan, M., and Park, S.-Y. (2014) Liquid Crystal-Based Proton Sensitive Glucose Biosensor. *Anal. Chem.*, **86** (3), 1493–1501.

12. Kim, J., Khan, M., and Park, S.-Y. (2013) Glucose Sensor using Liquid-Crystal Droplets Made by Microfluidics. *ACS Appl. Mater. Interfaces*, **5** (24), 13135–13139.

13. Aliño, V.J., Pang, J., and Yang, K.-L. (2011) Liquid Crystal Droplets as a Hosting and Sensing Platform for Developing Immunoassays. *Langmuir*, **27** (19), 11784–11789.

14. Lee, K., Chandra Gupta, K., Park, S.-Y., and Kang, I.-K. (2016) Anti-IgG-anchored liquid crystal microdroplets for label free detection of IgG. *J. Mater. Chem. B*, **4** (4), 704–715.

15. Sivakumar, S., Wark, K.L., Gupta, J.K., Abbott, N.L., and Caruso, F. (2009) Liquid Crystal Emulsions as the Basis of Biological Sensors for the Optical Detection of Bacteria and Viruses. *Adv. Funct. Mater.*, **19** (14), 2260–2265.

16. Gupta, J.K., Sivakumar, S., Caruso, F., and Abbott, N.L. (2009) Size-Dependent Ordering of Liquid Crystals Observed in Polymeric Capsules with Micrometer and Smaller Diameters. *Angew. Chem. Int. Ed.*, **48** (9), 1652–1655.

17. Manna, U., Zayas-Gonzalez, Y.M., Carlton, R.J., Caruso, F., Abbott, N.L., and Lynn, D.M. (2013) Liquid Crystal Chemical Sensors That Cells Can Wear. *Angew. Chem. Int. Ed.*, **52** (52), 14011–14015.

18. Bera, T., and Fang, J. (2013) Optical Detection of Lithocholic Acid with Liquid Crystal Emulsions. *Langmuir*, **29** (1), 387–392.

19. Niu, X., Luo, D., Chen, R., Wang, F., Sun, X., and Dai, H. (2016) Optical biosensor based on liquid crystal droplets for detection of cholic acid. *Opt. Commun.*, **381**, 286–291.

20. Yoon, S.H., Gupta, K.C., Borah, J.S., Park, S.-Y., Kim, Y.-K., Lee, J.-H., and Kang, I.-K. (2014) Folate Ligand Anchored Liquid Crystal Microdroplets Emulsion for in Vitro Detection of KB Cancer Cells. *Langmuir*, **30** (35), 10668–10677.

21. Lin, I.-H., Miller, D.S., Bertics, P.J., Murphy, C.J., Pablo, J.J. de, and Abbott, N.L. (2011) Endotoxin-Induced Structural Transformations in Liquid Crystalline Droplets. *Science*, **332** (6035), 1297–1300.

22. S. Miller, D., and L. Abbott, N. (2013) Influence of droplet size, pH and ionic strength on endotoxin-triggered ordering transitions in liquid crystalline droplets. *Soft Matter*, **9** (2), 374–382.

23. Wang, X., Bukusoglu, E., and Abbott, N.L. (2017) A Practical Guide to the Preparation of Liquid Crystal-Templated Microparticles. *Chem. Mater.*, **29** (1), 53–61.

24. Chattaraj, R., M. Goldscheitter, G., Yildirim, A., and P. Goodwin, A. (2016) Phase behavior of mixed lipid monolayers on perfluorocarbon nanoemulsions and its effect on acoustic contrast. *RSC Adv.*, **6** (112), 111318–111325.

25. Borden, M.A., Kruse, D.E., Caskey, C.F., Zhao, S., Dayton, P.A., and Ferrara, K.W. (2005) Influence of lipid shell physicochemical properties on ultrasound-induced microbubble destruction. *IEEE Trans. Ultrason. Ferroelectr. Freq. Control*, **52** (11), 1992–2002.

26. Mohan, P., Noonan, P.S., Nakatsuka, M.A., and Goodwin, A.P. (2014) On-Demand Droplet Fusion: A Strategy for Stimulus-Responsive Biosensing in Solution. *Langmuir*, **30** (41), 12321–12327.

27. Israelachvili, J.N. (2015) *Intermolecular and Surface Forces*, Academic Press.

28. Brake, J.M., Mezera, A.D., and Abbott, N.L. (2003) Effect of Surfactant Structure on the Orientation of Liquid Crystals at Aqueous−Liquid Crystal Interfaces. *Langmuir*, **19** (16), 6436–6442.

29. Gupta, J.K., Zimmerman, J.S., de Pablo, J.J., Caruso, F., and Abbott, N.L. (2009) Characterization of Adsorbate-Induced Ordering Transitions of Liquid Crystals within Monodisperse Droplets. *Langmuir*, **25** (16), 9016–9024.

30. Garg, S., Thomas, A.A., and Borden, M.A. (2013) The effect of lipid monolayer in-plane rigidity on in vivo microbubble circulation persistence. *Biomaterials*, **34** (28), 6862–6870.

31. Miller, D.S., Wang, X., Buchen, J., Lavrentovich, O.D., and Abbott, N.L. (2013) Analysis of the Internal Configurations of Droplets of Liquid Crystal Using Flow Cytometry. *Anal. Chem.*, **85** (21), 10296–10303.

32. I. Kinsinger, M., M. Lynn, D., and L. Abbott, N. (2010) Nematic ordering drives the phase separation of mixed monolayers containing phospholipids modified with poly(ethylene glycol) at aqueous–liquid crystal interfaces. *Soft Matter*, **6** (17), 4095–4104.

33. Hartono, D., Bi, X., Yang, K.-L., and Yung, L.-Y.L. (2008) An Air-Supported Liquid Crystal System for Real-Time and Label-Free Characterization of Phospholipases and Their Inhibitors. *Adv. Funct. Mater.*, **18** (19), 2938–2945.

34. Hartono, D., Lai, S.L., Yang, K.-L., and Yung, L.-Y.L. (2009) A liquid crystal-based sensor for real-time and label-free identification of phospholipase-like toxins and their inhibitors. *Biosens. Bioelectron.*, **24** (7), 2289–2293.

35. Liu, Y., Cheng, D., Lin, I.-H., L. Abbott, N., and Jiang, H. (2012) Microfluidic sensing devices employing in situ -formed liquid crystal thin film for detection of biochemical interactions. *Lab. Chip*, **12** (19), 3746–3753.

36. Chattaraj, R., Mohan, P., Besmer, J.D., and Goodwin, A.P. (2015) Selective Vaporization of Superheated Nanodroplets for Rapid, Sensitive, Acoustic Biosensing. *Adv. Healthc. Mater.*, **4** (12), 1790–1795.

37. Khan, M., and Park, S.-Y. (2015) Specific detection of avidin–biotin binding using liquid crystal droplets. *Colloids Surf. B Biointerfaces*, **127**, 241–246.

Chapter 6. Concluding Remarks

This work contributes several new and salient observations regarding the effects of the phospholipid shell on the nandodroplet (ND) internal phase behavior, with and without the presence of an external stimulus. First, it demonstrates the potential of NDs to perform as rapid, sensitive sensors in solution, as evidenced by the detection of picomolar levels of vascular endothelial growth factor and phospholipase A_2. Second, it shows that aggregation of perfluorocarbon (PFC) nanodroplets can enhance the ultrasound response under HIFU activation, probably due to increased superharmonic focusing. Third, it shows how the heterogeneous distribution of lipids and lipopolymers in a PFC droplet shell may change acoustic contrast and droplet yield. Finally, it re-evaluates the influence of increasing lipid acyl chain length on the orientation of liquid crystal molecules in droplets.

There remain, however, significant future avenues to be pursued in this line of investigation. One of the most prominent challenges is the interactions with non-specific proteins present in physiological media. For example, we have found that vaporization threshold for PFC NDs is reduced in serum, which increases baseline levels of acoustic contrast and adversely affects ND sensitivity to analyte detection. It is therefore imperative to study the composition of the non-specific protein corona in the droplet monolayer and explore methods to reduce or tune it for better function both *in vitro* and *in vivo*. Tuning the protein corona would help in droplets reaching their physiological targets with greater efficiency, and by extension help in applications beyond biosensing, like drug delivery or tissue ablation. Addressing these issues would allow extension of this work to *in vivo* models and provide more detailed information regarding the design of these droplets as biosensors and therapeutic agents.

Bibliography

Aliño, V.J., Pang, J., and Yang, K.-L. (2011) Liquid Crystal Droplets as a Hosting and Sensing Platform for Developing Immunoassays. *Langmuir*, **27** (19), 11784–11789.

Anton, N., Pierrat, P., Lebeau, L., F. Vandamme, T., and Bouriat, P. (2013) A study of insoluble monolayers by deposition at a bubble interface. *Soft Matter*, **9** (42), 10081–10091.

Bach, D., and Wachtel, E. (2003) Phospholipid/cholesterol model membranes: formation of cholesterol crystallites. *Biochimica et Biophysica Acta (BBA) - Biomembranes*, **1610** (2), 187–197.

Bai, Y., and Abbott, N.L. (2011) Recent Advances in Colloidal and Interfacial Phenomena Involving Liquid Crystals. *Langmuir*, **27** (10), 5719–5738.

Baoukina, S., Mendez-Villuendas, E., and Tieleman, D.P. (2012) Molecular view of phase coexistence in lipid monolayers. *J. Am. Chem. Soc.*, **134** (42), 17543–17553.

Bera, T., Deng, J., and Fang, J. (2014) Protein-Induced Configuration Transitions of Polyelectrolyte-Modified Liquid Crystal Droplets. *J. Phys. Chem. B*, **118** (18), 4970–4975.

Bera, T., and Fang, J. (2013) Optical Detection of Lithocholic Acid with Liquid Crystal Emulsions. *Langmuir*, **29** (1), 387–392.

Borden, M.A., Kruse, D.E., Caskey, C.F., Zhao, S., Dayton, P.A., and Ferrara, K.W. (2005) Influence of lipid shell physicochemical properties on ultrasound-induced microbubble destruction. *IEEE Transactions on Ultrasonics, Ferroelectrics, and Frequency Control*, **52** (11), 1992–2002.

Borden, M.A., Martinez, G.V., Ricker, J., Tsvetkova, N., Longo, M., Gillies, R.J., Dayton, P.A., and Ferrara, K.W. (2006) Lateral Phase Separation in Lipid-Coated Microbubbles. *Langmuir*, **22** (9), 4291–4297.

Brake, J.M., and Abbott, N.L. (2007) Coupling of the Orientations of Thermotropic Liquid Crystals to Protein Binding Events at Lipid-Decorated Interfaces. *Langmuir*, **23** (16), 8497–8507.

Brake, J.M., Daschner, M.K., Luk, Y.-Y., and Abbott, N.L. (2003) Biomolecular Interactions at Phospholipid-Decorated Surfaces of Liquid Crystals. *Science*, **302** (5653), 2094–2097.

Brake, J.M., Mezera, A.D., and Abbott, N.L. (2003) Effect of Surfactant Structure on the Orientation of Liquid Crystals at Aqueous−Liquid Crystal Interfaces. *Langmuir*, **19** (16), 6436–6442.

Burgess, M.T., and Porter, T.M. (2015) Acoustic Cavitation-Mediated Delivery of Small Interfering Ribonucleic Acids with Phase-Shift Nano-Emulsions. *Ultrasound in Medicine and Biology*, **41** (8), 2191–2201.

Cavalieri, F., Micheli, L., Kaliappan, S., Teo, B.M., Zhou, M., Palleschi, G., and Ashokkumar, M. (2013) Antimicrobial and Biosensing Ultrasound-Responsive Lysozyme-Shelled Microbubbles. *ACS Appl. Mater. Interfaces*, **5** (2), 464–471.

Chapman, R., Lin, Y., Burnapp, M., Bentham, A., Hillier, D., Zabron, A., Khan, S., Tyreman, M., and Stevens, M.M. (2015) Multivalent Nanoparticle Networks Enable Point-of-Care Detection of Human Phospholipase-A2 in Serum. *ACS Nano*, **9** (3), 2565–2573.

Chattaraj, R., M. Goldscheitter, G., Yildirim, A., and P. Goodwin, A. (2016) Phase behavior of mixed lipid monolayers on perfluorocarbon nanoemulsions and its effect on acoustic contrast. *RSC Advances*, **6** (112), 111318–111325.

Chattaraj, R., Mohan, P., Besmer, J.D., and Goodwin, A.P. (2015) Selective Vaporization of Superheated Nanodroplets for Rapid, Sensitive, Acoustic Biosensing. *Adv. Healthcare Mater.*, **4** (12), 1790–1795.

Chattaraj, R., Mohan, P., Livingston, C.M., Besmer, J.D., Kumar, K., and Goodwin, A.P. (2016) Mutually-Reactive, Fluorogenic Hydrocyanine/Quinone Reporter Pairs for In-Solution Biosensing via Nanodroplet Association. *ACS Appl. Mater. Interfaces*, **8** (1), 802–808.

Chen, A.K., Behlke, M.A., and Tsourkas, A. (2007) Avoiding false-positive signals with nuclease-vulnerable molecular beacons in single living cells. *Nucleic Acids Res*, **35** (16), e105–e105.

Cheng, Y.-S.L., Rees, T., and Wright, J. (2014) A review of research on salivary biomarkers for oral cancer detection. *Clin Trans Med*, **3** (1), 3.

Chime, S.A., Kenechukwu, F.C., and Attama, A.A. (2014) Nanoemulsions — Advances in Formulation, Characterization and Applications in Drug Delivery.

Chinen, A.B., Guan, C.M., Ferrer, J.R., Barnaby, S.N., Merkel, T.J., and Mirkin, C.A. (2015) Nanoparticle Probes for the Detection of Cancer Biomarkers, Cells, and Tissues by Fluorescence. *Chem. Rev.*, **115** (19), 10530–10574.

Choi, C.-H., Kim, J., Nam, J.-O., Kang, S.-M., Jeong, S.-G., and Lee, C.-S. (2014) Microfluidic Design of Complex Emulsions. *ChemPhysChem*, **15** (1), 21–29.

Coley, B.D., Trambert, M.A., and Mattrey, R.F. (1994) Perfluorocarbon-enhanced sonography: value in detecting acute venous thrombosis in rabbits. *American Journal of Roentgenology*, **163** (4), 961–964.

Dayton, P.A., Zhao, S., Bloch, S.H., Schumann, P., Penrose, K., Matsunaga, T.O., Zutshi, R., Doinikov, A., and Ferrara, K.W. (2006) Application of Ultrasound to Selectively Localize Nanodroplets for Targeted Imaging and Therapy. *Mol Imaging*, **5** (3), 7290.2006.00019.

Deshpande, N., Needles, A., and Willmann, J.K. (2010) Molecular ultrasound imaging: current status and future directions. *Clinical Radiology*, **65** (7), 567–581.

Dijkstra, S., Mulders, P.F.A., and Schalken, J.A. (2014) Clinical use of novel urine and blood based prostate cancer biomarkers: A review. *Clinical Biochemistry*, **47** (10), 889–896.

Dong, Z., Liu, Y., Scott, K.F., Levin, L., Gaitonde, K., Bracken, R.B., Burke, B., Zhai, Q.J., Wang, J., Oleksowicz, L., and Lu, S. (2010) Secretory phospholipase A2-IIa is involved in prostate cancer progression and may potentially serve as a biomarker for prostate cancer. *Carcinogenesis*, **31** (11), 1948–1955.

Edidin, M. (2003) The State of Lipid Rafts: From Model Membranes to Cells. *Annual Review of Biophysics and Biomolecular Structure*, **32** (1), 257–283.

Elghanian, R., Storhoff, J.J., Mucic, R.C., Letsinger, R.L., and Mirkin, C.A. (1997) Selective Colorimetric Detection of Polynucleotides Based on the Distance-Dependent Optical Properties of Gold Nanoparticles. *Science*, **277** (5329), 1078–1081.

F.R.S, L.R.O.M. (1917) VIII. On the pressure developed in a liquid during the collapse of a spherical cavity. *The London, Edinburgh, and Dublin Philosophical Magazine and Journal of Science*, **34** (200), 94–98.

Fabiilli, M.L., Haworth, K.J., Fakhri, N.H., Kripfgans, O.D., Carson, P.L., and Fowlkes, J.B. (2009) The role of inertial cavitation in acoustic droplet vaporization. *IEEE Trans Ultrason Ferroelectr Freq Control*, **56** (5), 1006–1017.

Fabiilli, M.L., Haworth, K.J., Sebastian, I.E., Kripfgans, O.D., Carson, P.L., and Fowlkes, J.B. (2010) Delivery of Chlorambucil Using an Acoustically-Triggered Perfluoropentane Emulsion. *Ultrasound in Medicine and Biology*, **36** (8), 1364–1375.

Ferrara, K., Pollard, R., and Borden, M. (2007) Ultrasound Microbubble Contrast Agents: Fundamentals and Application to Gene and Drug Delivery. *Annual Review of Biomedical Engineering*, **9** (1), 415–447.

Feshitan, J.A., Chen, C.C., Kwan, J.J., and Borden, M.A. (2009) Microbubble size isolation by differential centrifugation. *Journal of Colloid and Interface Science*, **329** (2), 316–324.

Filipe, V., Hawe, A., and Jiskoot, W. (2010) Critical Evaluation of Nanoparticle Tracking Analysis (NTA) by NanoSight for the Measurement of Nanoparticles and Protein Aggregates. *Pharmaceutical Research; New York*, **27** (5), 796–810.

Fitch, K.R., and Goodwin, A.P. (2014) Mechanochemical Reaction Cascade for Sensitive Detection of Covalent Bond Breakage in Hydrogels. *Chem. Mater.*, **26** (23), 6771–6776.

Fix, S.M., Borden, M.A., and Dayton, P.A. (2015) Therapeutic gas delivery via microbubbles and liposomes. *Journal of Controlled Release*, **209**, 139–149.

Forsberg, F., Roy, R., Merton, D.A., Rawool, N.M., Liu, J.-B., Huang, M., Kessler, D., and Goldberg, B.B. (1998) Conventional and hypobaric activation of an ultrasound contrast agent. *Ultrasound in Medicine and Biology*, **24** (8), 1143–1150.

Freeman, R., Girsh, J., Fang-ju Jou, A., Ho, J.A., Hug, T., Dernedde, J., and Willner, I. (2012) Optical Aptasensors for the Analysis of the Vascular Endothelial Growth Factor (VEGF). *Anal. Chem.*, **84** (14), 6192–6198.

Gao, Z., Kennedy, A.M., Christensen, D.A., and Rapoport, N.Y. (2008) Drug-loaded nano/microbubbles for combining ultrasonography and targeted chemotherapy. *Ultrasonics*, **48** (4), 260–270.

Garg, S., Thomas, A.A., and Borden, M.A. (2013) The effect of lipid monolayer in-plane rigidity on in vivo microbubble circulation persistence. *Biomaterials*, **34** (28), 6862–6870.

Giesecke, T., and Hynynen, K. (2003) Ultrasound-mediated cavitation thresholds of liquid perfluorocarbon droplets in vitro. *Ultrasound in Medicine and Biology*, **29** (9), 1359–1365.

Goodwin, A.P., Nakatsuka, M.A., and Mattrey, R.F. (2015) Stimulus–responsive ultrasound contrast agents for clinical imaging: motivations, demonstrations, and future directions. *WIREs Nanomed Nanobiotechnol*, **7** (1), 111–123.

Grinstaff, M.W., and Suslick, K.S. (1991) Air-filled proteinaceous microbubbles: synthesis of an echo-contrast agent. *PNAS*, **88** (17), 7708–7710.

Guiot, C., Cavalli, R., Gaglioti, P., Danelon, D., Musacchio, C., Trotta, M., and Todros, T. (2004) Temperature monitoring using ultrasound contrast agents: in vitro investigation on thermal stability. *Ultrasonics*, **42** (1), 927–930.

Guo, S., Shi, A., Xu, S., Du, X., Wang, X., Zong, Y., Bouakaz, A., and Wan, M. (2017) Lowering of acoustic droplet vaporization threshold via aggregation. *Appl. Phys. Lett.*, **111** (25), 254102.

Guo, Z., Park, S., Yoon, J., and Shin, I. (2014) Recent progress in the development of near-infrared fluorescent probes for bioimaging applications. *Chemical Society Reviews*, **43** (1), 16–29.

Gupta, A., Burak Eral, H., Alan Hatton, T., and S. Doyle, P. (2016) Nanoemulsions: formation, properties and applications. *Soft Matter*, **12** (11), 2826–2841.

Gupta, J.K., Sivakumar, S., Caruso, F., and Abbott, N.L. (2009) Size-Dependent Ordering of Liquid Crystals Observed in Polymeric Capsules with Micrometer and Smaller Diameters. *Angewandte Chemie International Edition*, **48** (9), 1652–1655.

Gupta, J.K., Zimmerman, J.S., de Pablo, J.J., Caruso, F., and Abbott, N.L. (2009) Characterization of Adsorbate-Induced Ordering Transitions of Liquid Crystals within Monodisperse Droplets. *Langmuir*, **25** (16), 9016–9024.

Hamaguchi, N., Ellington, A., and Stanton, M. (2001) Aptamer Beacons for the Direct Detection of Proteins. *Analytical Biochemistry*, **294** (2), 126–131.

Hancock, J.F. (2006) Lipid rafts: contentious only from simplistic standpoints. *Nature Reviews Molecular Cell Biology*, **7** (6), 456–462.

Hannah, A.S., VanderLaan, D., Chen, Y.-S., and Emelianov, S.Y. (2014) Photoacoustic and ultrasound imaging using dual contrast perfluorocarbon nanodroplets triggered by laser pulses at 1064 nm. *Biomed. Opt. Express, BOE*, **5** (9), 3042–3052.

Hartono, D., Bi, X., Yang, K.-L., and Yung, L.-Y.L. (2008) An Air-Supported Liquid Crystal System for Real-Time and Label-Free Characterization of Phospholipases and Their Inhibitors. *Adv. Funct. Mater.*, **18** (19), 2938–2945.

Hartono, D., Lai, S.L., Yang, K.-L., and Yung, L.-Y.L. (2009) A liquid crystal-based sensor for real-time and label-free identification of phospholipase-like toxins and their inhibitors. *Biosensors and Bioelectronics*, **24** (7), 2289–2293.

Hettiarachchi, K., and Lee, A.P. (2010) Polymer–lipid microbubbles for biosensing and the formation of porous structures. *Journal of Colloid and Interface Science*, **344** (2), 521–527.

Hoff, L., Sontum, P.C., and Hovem, J.M. (2000) Oscillations of polymeric microbubbles: Effect of the encapsulating shell. *The Journal of the Acoustical Society of America*, **107** (4), 2272–2280.

Hussain, A., Pina, A.S., and Roque, A.C.A. (2009) Bio-recognition and detection using liquid crystals. *Biosensors and Bioelectronics*, **25** (1), 1–8.

I. Kinsinger, M., M. Lynn, D., and L. Abbott, N. (2010) Nematic ordering drives the phase separation of mixed monolayers containing phospholipids modified with poly(ethylene glycol) at aqueous–liquid crystal interfaces. *Soft Matter*, **6** (17), 4095–4104.

Idris, A., Ghazali, N.B., and Koh, D. (2015) Interleukin 1β—A Potential Salivary Biomarker for Cancer Progression? *Biomark Cancer*, **7**, 25–29.

Immordino, M.L., Dosio, F., and Cattel, L. (2006) Stealth liposomes: review of the basic science, rationale, and clinical applications, existing and potential. *Int J Nanomedicine*, **1** (3), 297–315.

Israelachvili, J.N. (2015) *Intermolecular and Surface Forces*, Academic Press.

Jian, J., Liu, C., Gong, Y., Su, L., Zhang, B., Wang, Z., wang, D., Zhou, Y., Xu, F., Li, P., Zheng, Y., Song, L., and Zhou, X. (2014) India Ink Incorporated Multifunctional Phase-transition Nanodroplets for Photoacoustic/Ultrasound Dual-modality Imaging and Photoacoustic Effect Based Tumor Therapy. *Theranostics*, **4** (10), 1026–1038.

Jiang, T., Olson, E.S., Nguyen, Q.T., Roy, M., Jennings, P.A., and Tsien, R.Y. (2004) Tumor imaging by means of proteolytic activation of cell-penetrating peptides. *PNAS*, **101** (51), 17867–17872.

Jin Lee, H., W. Wark, A., and M. Corn, R. (2008) Microarray methods for protein biomarker detection. *Analyst*, **133** (8), 975–983.

Jokerst, J.V., Khademi, C., and Gambhir, S.S. (2013) Intracellular Aggregation of Multimodal Silica Nanoparticles for Ultrasound-Guided Stem Cell Implantation. *Science Translational Medicine*, **5** (177), 177ra35-177ra35.

Julian McClements, D. (2012) Nanoemulsions versus microemulsions: terminology, differences, and similarities. *Soft Matter*, **8** (6), 1719–1729.

Karshafian, R., Bevan, P.D., Williams, R., Samac, S., and Burns, P.N. (2009) Sonoporation by Ultrasound-Activated Microbubble Contrast Agents: Effect of Acoustic Exposure Parameters on Cell Membrane Permeability and Cell Viability. *Ultrasound in Medicine and Biology*, **35** (5), 847–860.

Kasoji, S.K., Pattenden, S.G., Malc, E.P., Jayakody, C.N., Tsuruta, J.K., Mieczkowski, P.A., Janzen, W.P., and Dayton, P.A. (2015) Cavitation Enhancing Nanodroplets Mediate Efficient DNA Fragmentation in a Bench Top Ultrasonic Water Bath. *PLOS ONE*, **10** (7), e0133014.

Khan, M., and Park, S.-Y. (2014) Liquid Crystal-Based Proton Sensitive Glucose Biosensor. *Anal. Chem.*, **86** (3), 1493–1501.

Khan, M., and Park, S.-Y. (2015) Specific detection of avidin–biotin binding using liquid crystal droplets. *Colloids and Surfaces B: Biointerfaces*, **127**, 241–246.

Kim, J., Khan, M., and Park, S.-Y. (2013) Glucose Sensor using Liquid-Crystal Droplets Made by Microfluidics. *ACS Appl. Mater. Interfaces*, **5** (24), 13135–13139.

Klibanov, A.L. (2007) Ultrasound molecular imaging with targeted microbubble contrast agents. *J Nucl Cardiol*, **14** (6), 876.

Klibanov, A.L., Rasche, P.T., Hughes, M.S., Wojdyla, J.K., Galen, K.P., Wible, J.H., and Brandenburger, G.H. (2002) Detection of individual microbubbles of an ultrasound contrast agent: fundamental and pulse inversion imaging. *Acad Radiol*, **9 Suppl 2**, S279-281.

Klymchenko, A.S., Roger, E., Anton, N., Anton, H., Shulov, I., Vermot, J., Mely, Y., and Vandamme, T.F. (2012) Highly lipophilic fluorescent dyes in nano-emulsions: towards bright non-leaking nano-droplets. *RSC Adv.*, **2** (31), 11876–11886.

Kobayashi, H., and Choyke, P.L. (2011) Target-cancer cell specific activatable fluorescence imaging Probes: Rational Design and in vivo Applications. *Acc Chem Res*, **44** (2), 83–90.

Kopechek, J.A., Park, E., Mei, C.-S., McDannold, N.J., and Porter, T.M. (2013) Accumulation of Phase-Shift Nanoemulsions to Enhance MR-Guided Ultrasound-Mediated Tumor Ablation In Vivo. *Journal of Healthcare Engineering*.

Kopechek, J.A., Park, E., Mei, C.-S., McDannold, N.J., and Porter, T.M. (2013) Accumulation of Phase-Shift Nanoemulsions to Enhance MR-Guided Ultrasound-Mediated Tumor Ablation In Vivo. *Journal of Healthcare Engineering*.

Kopechek, J.A., Zhang, P., Burgess, M.T., and Porter, T.M. (2012) Synthesis of Phase-shift Nanoemulsions with Narrow Size Distributions for Acoustic Droplet Vaporization and Bubble-enhanced Ultrasound-mediated Ablation. *J Vis Exp*, (67).

Kripfgans, O.D., Fowlkes, J.B., Miller, D.L., Eldevik, O.P., and Carson, P.L. (2000) Acoustic droplet vaporization for therapeutic and diagnostic applications. *Ultrasound in Medicine and Biology*, **26** (7), 1177–1189.

Kundu, K., Knight, S.F., Lee, S., Taylor, W.R., and Murthy, N. (2010) A Significant Improvement of the Efficacy of Radical Oxidant Probes by the Kinetic Isotope Effect. *Angewandte Chemie International Edition*, **49** (35), 6134–6138.

Kundu, K., Knight, S.F., Willett, N., Lee, S., Taylor, W.R., and Murthy, N. (2009) Hydrocyanines: A Class of Fluorescent Sensors That Can Image Reactive Oxygen Species in Cell Culture, Tissue, and In Vivo. *Angewandte Chemie International Edition*, **48** (2), 299–303.

Kupert, E., Anderson, M., Liu, Y., Succop, P., Levin, L., Wang, J., Wikenheiser-brokamp, K., Chen, P., Pinney, S.M., Macdonald, T., Dong, Z., Starnes, S., and Lu, S. (2011) Plasma secretory phospholipase A2-IIa as a potential biomarker for lung cancer in patients with solitary pulmonary nodules. *BMC Cancer*, **11**, 513.

Kwan, J.J., and Borden, M.A. (2012) Lipid monolayer collapse and microbubble stability. *Advances in Colloid and Interface Science*, **183**–**184**, 82–99.

Ławicki, S., Zajkowska, M., Głażewska, E.K., Będkowska, G.E., and Szmitkowski, M. (2017) Plasma levels and diagnostic utility of VEGF, MMP-2 and TIMP-2 in the diagnostics of breast cancer patients. *Biomarkers*, **22** (2), 157–164.

Lee, J.H., Domaille, D.W., and Cha, J.N. (2012) Amplified Protein Detection and Identification through DNA-Conjugated M13 Bacteriophage. *ACS Nano*, **6** (6), 5621–5626.

Lee, K., Chandra Gupta, K., Park, S.-Y., and Kang, I.-K. (2016) Anti-IgG-anchored liquid crystal microdroplets for label free detection of IgG. *Journal of Materials Chemistry B*, **4** (4), 704–715.

Leighton, T. (2012) *The Acoustic Bubble*, Academic Press.

Li, J.J., Chu, Y., Lee, B.Y.-H., and Xie, X.S. (2008) Enzymatic signal amplification of molecular beacons for sensitive DNA detection. *Nucleic Acids Res*, **36** (6), e36–e36.

Li, W.-W., Heinze, J., and Haehnel, W. (2005) Site-Specific Binding of Quinones to Proteins through Thiol Addition and Addition−Elimination Reactions. *J. Am. Chem. Soc.*, **127** (17), 6140–6141.

Lin, I.-H., Miller, D.S., Bertics, P.J., Murphy, C.J., Pablo, J.J. de, and Abbott, N.L. (2011) Endotoxin-Induced Structural Transformations in Liquid Crystalline Droplets. *Science*, **332** (6035), 1297–1300.

Lin, M.Y., Lindsay, H.M., Weitz, D.A., Klein, R., Ball, R.C., and Meakin, P. (1990) Universal diffusion-limited colloid aggregation. *J. Phys.: Condens. Matter*, **2** (13), 3093.

Lindner, J.R. (2004) Microbubbles in medical imaging: current applications and future directions. *Nature Reviews Drug Discovery*, **3** (6), 527–533.

Lingwood, D., and Simons, K. (2010) Lipid Rafts As a Membrane-Organizing Principle. *Science*, **327** (5961), 46–50.

Liu, F., Lin, S., Zhang, Z., Hu, J., Liu, G., Tu, Y., Yang, Y., Zou, H., Mo, Y., and Miao, L. (2014) pH-Responsive Nanoemulsions for Controlled Drug Release. *Biomacromolecules*, **15** (3), 968–977.

Liu, H.-L., Fan, C.-H., Ting, C.-Y., and Yeh, C.-K. (2014) Combining Microbubbles and Ultrasound for Drug Delivery to Brain Tumors: Current Progress and Overview. *Theranostics*, **4** (4), 432–444.

Liu, N.J., Chapman, R., Lin, Y., Mmesi, J., Bentham, A., Tyreman, M., Abraham, S., and Stevens, M.M. (2016) Point of care testing of phospholipase A2 group IIA for serological diagnosis of rheumatoid arthritis. *Nanoscale*, **8** (8), 4482–4485.

Liu, N.J., Chapman, R., Lin, Y., Bentham, A., Tyreman, M., Philips, N., Khan, S.A., and Stevens, M.M. (2016) Phospholipase A2 as a point of care alternative to serum amylase and pancreatic lipase. *Nanoscale*, **8** (23), 11834–11839.

Liu, Y., Cheng, D., Lin, I.-H., L. Abbott, N., and Jiang, H. (2012) Microfluidic sensing devices employing in situ -formed liquid crystal thin film for detection of biochemical interactions. *Lab on a Chip*, **12** (19), 3746–3753.

Lockwood, N.A., and Abbott, N.L. (2005) Self-assembly of surfactants and phospholipids at interfaces between aqueous phases and thermotropic liquid crystals. *Current Opinion in Colloid & Interface Science*, **10** (3), 111–120.

Lockwood, N.A., Gupta, J.K., and Abbott, N.L. (2008) Self-assembly of amphiphiles, polymers and proteins at interfaces between thermotropic liquid crystals and aqueous phases. *Surface Science Reports*, **63** (6), 255–293.

Lowe, A.M., and Abbott, N.L. (2012) Liquid Crystalline Materials for Biological Applications. *Chem. Mater.*, **24** (5), 746–758.

Luke, G.P., Hannah, A.S., and Emelianov, S.Y. (2016) Super-Resolution Ultrasound Imaging in Vivo with Transient Laser-Activated Nanodroplets. *Nano Lett*, **16** (4), 2556–2559.

Mahendran, V., and Philip, J. (2013) A methanol sensor based on stimulus-responsive magnetic nanoemulsions. *Sensors and Actuators B: Chemical*, **185**, 488–495.

Mandal, S.K., Lequeux, N., Rotenberg, B., Tramier, M., Fattaccioli, J., Bibette, J., and Dubertret, B. (2005) Encapsulation of magnetic and fluorescent nanoparticles in emulsion droplets. *Langmuir*, **21** (9), 4175–4179.

Manna, U., Zayas-Gonzalez, Y.M., Carlton, R.J., Caruso, F., Abbott, N.L., and Lynn, D.M. (2013) Liquid Crystal Chemical Sensors That Cells Can Wear. *Angew. Chem. Int. Ed.*, **52** (52), 14011–14015.

Mashaghi, S., Abbaspourrad, A., Weitz, D.A., and van Oijen, A.M. (2016) Droplet microfluidics: A tool for biology, chemistry and nanotechnology. *TrAC Trends in Analytical Chemistry*, **82**, 118–125.

Mason, H.S. (1955) Reactions between Quinones and Proteins. *Nature*, **175** (4461), 771–772.

Matsunaga, T.O., Sheeran, P.S., Luois, S., Streeter, J.E., Mullin, L.B., Banerjee, B., and Dayton, P.A. (2012) Phase-Change Nanoparticles Using Highly Volatile Perfluorocarbons: Toward a Platform for Extravascular Ultrasound Imaging. *Theranostics*, **2** (12), 1185–1198.

McMullen, T.P.W., Lewis, R.N.A.H., and McElhaney, R.N. (2004) Cholesterol–phospholipid interactions, the liquid-ordered phase and lipid rafts in model and biological membranes. *Current Opinion in Colloid & Interface Science*, **8** (6), 459–468.

Mercado, K.P., Radhakrishnan, K., Stewart, K., Snider, L., Ryan, D., and Haworth, K.J. (2016) Size-isolation of ultrasound-mediated phase change perfluorocarbon droplets using differential centrifugation. *The Journal of the Acoustical Society of America*, **139** (5), EL142-EL148.

Miller, D.S., Wang, X., Buchen, J., Lavrentovich, O.D., and Abbott, N.L. (2013) Analysis of the Internal Configurations of Droplets of Liquid Crystal Using Flow Cytometry. *Anal. Chem.*, **85** (21), 10296–10303.

Miller, E.W., Albers, A.E., Pralle, A., Isacoff, E.Y., and Chang, C.J. (2005) Boronate-Based Fluorescent Probes for Imaging Cellular Hydrogen Peroxide. *J. Am. Chem. Soc.*, **127** (47), 16652–16659.

Miller, E.W., Tulyathan, O., Isacoff, E.Y., and Chang, C.J. (2007) Molecular imaging of hydrogen peroxide produced for cell signaling. *Nature Chemical Biology*, **3** (5), 263–267.

Min, C., Shao, H., Liong, M., Yoon, T.-J., Weissleder, R., and Lee, H. (2012) Mechanism of Magnetic Relaxation Switching Sensing. *ACS Nano*, **6** (8), 6821–6828.

Mohan, P., Noonan, P.S., Nakatsuka, M.A., and Goodwin, A.P. (2014) On-Demand Droplet Fusion: A Strategy for Stimulus-Responsive Biosensing in Solution. *Langmuir*, **30** (41), 12321–12327.

Mountford, P.A., Smith, W.S., and Borden, M.A. (2015) Fluorocarbon Nanodrops as Acoustic Temperature Probes. *Langmuir*, **31** (39), 10656–10663.

Mountford, P.A., Thomas, A.N., and Borden, M.A. (2015) Thermal activation of superheated lipid-coated perfluorocarbon drops. *Langmuir*, **31** (16), 4627–4634.

Moyer, L.C., Timbie, K.F., Sheeran, P.S., Price, R.J., Miller, G.W., and Dayton, P.A. (2015) High-intensity focused ultrasound ablation enhancement in vivo via phase-shift nanodroplets compared to microbubbles. *Journal of Therapeutic Ultrasound*, **3**, 7.

Muller, Y.A., Li, B., Christinger, H.W., Wells, J.A., Cunningham, B.C., and Vos, A.M. de (1997) Vascular endothelial growth factor: Crystal structure and functional mapping of the kinase domain receptor binding site. *PNAS*, **94** (14), 7192–7197.

Mura, S., Nicolas, J., and Couvreur, P. (2013) Stimuli-responsive nanocarriers for drug delivery. *Nature Materials*, **12** (11), 991–1003.

Nakatsuka, M.A., Barback, C.V., Fitch, K.R., Farwell, A.R., Esener, S.C., Mattrey, R.F., Cha, J.N., and Goodwin, A.P. (2013) In vivo ultrasound visualization of non-occlusive blood clots with thrombin-sensitive contrast agents. *Biomaterials*, **34** (37), 9559–9565.

Nakatsuka, M.A., Hsu, M.J., Esener, S.C., Cha, J.N., and Goodwin, A.P. (2011) DNA-Coated Microbubbles with Biochemically Tunable Ultrasound Contrast Activity. *Adv. Mater.*, **23** (42), 4908–4912.

Nakatsuka, M.A., Mattrey, R.F., Esener, S.C., Cha, J.N., and Goodwin, A.P. (2012) Aptamer-Crosslinked Microbubbles: Smart Contrast Agents for Thrombin-Activated Ultrasound Imaging. *Adv. Mater.*, **24** (45), 6010–6016.

Nam, J.-M., Thaxton, C.S., and Mirkin, C.A. (2003) Nanoparticle-Based Bio-Bar Codes for the Ultrasensitive Detection of Proteins. *Science*, **301** (5641), 1884–1886.

Nicolas, J.-P., Lin, Y., Lambeau, G., Ghomashchi, F., Lazdunski, M., and Gelb, M.H. (1997) Localization of Structural Elements of Bee Venom Phospholipase A2 Involved in N-type Receptor Binding and Neurotoxicity. *J. Biol. Chem.*, **272** (11), 7173–7181.

Niu, X., Luo, D., Chen, R., Wang, F., Sun, X., and Dai, H. (2016) Optical biosensor based on liquid crystal droplets for detection of cholic acid. *Optics Communications*, **381**, 286–291.

Noonan, P.S., Mohan, P., Goodwin, A.P., and Schwartz, D.K. (2014) DNA Hybridization-Mediated Liposome Fusion at the Aqueous Liquid Crystal Interface. *Adv. Funct. Mater.*, **24** (21), 3206–3212.

Noonan, P.S., Roberts, R.H., and Schwartz, D.K. (2013) Liquid Crystal Reorientation Induced by Aptamer Conformational Changes. *J. Am. Chem. Soc.*, **135** (13), 5183–5189.

Olson, E.S., Jiang, T., Aguilera, T.A., Nguyen, Q.T., Ellies, L.G., Scadeng, M., and Tsien, R.Y. (2010) Activatable cell penetrating peptides linked to nanoparticles as dual probes for in vivo fluorescence and MR imaging of proteases. *PNAS*, **107** (9), 4311–4316.

Oushiki, D., Kojima, H., Terai, T., Arita, M., Hanaoka, K., Urano, Y., and Nagano, T. (2010) Development and Application of a Near-Infrared Fluorescence Probe for Oxidative Stress Based on Differential Reactivity of Linked Cyanine Dyes. *J. Am. Chem. Soc.*, **132** (8), 2795–2801.

Park, J.-H., von Maltzahn, G., Zhang, L., Schwartz, M.P., Ruoslahti, E., Bhatia, S.N., and Sailor, M.J. (2008) Magnetic Iron Oxide Nanoworms for Tumor Targeting and Imaging. *Adv. Mater.*, **20** (9), 1630–1635.

Park, J.-S., and Abbott, N.L. (2008) Ordering Transitions in Thermotropic Liquid Crystals Induced by the Interfacial Assembly and Enzymatic Processing of Oligopeptide Amphiphiles. *Adv. Mater.*, **20** (6), 1185–1190.

Pellow, C., Goertz, D.E., and Zheng, G. Breaking free from vascular confinement: status and prospects for submicron ultrasound contrast agents. (2017) *WIREs Nanomed Nanobiotechnol*.

Perng, J.K., Lee, S., Kundu, K., Caskey, C.F., Knight, S.F., Satir, S., Ferrara, K.W., Taylor, W.R., Degertekin, F.L., Sorescu, D., and Murthy, N. (2012) Ultrasound Imaging of Oxidative Stress *In Vivo* with Chemically-Generated Gas Microbubbles. *Ann Biomed Eng*, **40** (9), 2059–2068.

Perrin, P., Porcar, I., and Tribet, C. (2003) Stimuli-responsive emulsions stabilized by polymeric surfactants. *Polym. Int.*, **52** (4), 465–470.

Phillips, P. and Gardner, E. (2004) Contrast–agent detection and quantification. *Eur. Radiol. Suppl.*, **14** (8), P4–P10.

Pitt, W.G., Singh, R.N., Perez, K.X., Husseini, G.A., and Jack, D.R. (2014) Phase transitions of perfluorocarbon nanoemulsion induced with ultrasound: A mathematical model. *Ultrasonics Sonochemistry*, **21** (2), 879–891.

Porter, T.R., Iversen, P.L., Li, S., and Xie, F. (1996) Interaction of diagnostic ultrasound with synthetic oligonucleotide-labeled perfluorocarbon-exposed sonicated dextrose albumin microbubbles. *Journal of Ultrasound in Medicine*, **15** (8), 577–584.

Potty, A.S.R., Kourentzi, K., Fang, H., Jackson, G.W., Zhang, X., Legge, G.B., and Willson, R.C. (2009) Biophysical characterization of DNA aptamer interactions with vascular endothelial growth factor. *Biopolymers*, **91** (2), 145–156.

Price, A.D. (2008) DNA Hybridization-Induced Reorientation of Liquid Crystal Anchoring at the Nematic Liquid Crystal/Aqueous Interface. *J. Am. Chem. Soc.*, **130** (26), 8188–8194.

Quinn, P.J., and Wolf, C. (2009) The liquid-ordered phase in membranes. *Biochimica et Biophysica Acta (BBA) - Biomembranes*, **1788** (1), 33–46.

Rapoport, N. (2012) Phase-shift, stimuli-responsive perfluorocarbon nanodroplets for drug delivery to cancer. *WIREs Nanomed Nanobiotechnol*, **4** (5), 492–510.

Rapoport, N., Gao, Z., and Kennedy, A. (2007) Multifunctional Nanoparticles for Combining Ultrasonic Tumor Imaging and Targeted Chemotherapy. *J Natl Cancer Inst*, **99** (14), 1095–1106.

Rapoport, N., Nam, K.-H., Gupta, R., Gao, Z., Mohan, P., Payne, A., Todd, N., Liu, X., Kim, T., Shea, J., Scaife, C., Parker, D.L., Jeong, E.-K., and Kennedy, A.M. (2011) Ultrasound-mediated tumor imaging and nanotherapy using drug loaded, block copolymer stabilized perfluorocarbon nanoemulsions. *Journal of Controlled Release*, **153** (1), 4–15.

Rapoport, N.Y., Kennedy, A.M., Shea, J.E., Scaife, C.L., and Nam, K.-H. (2009) Controlled and targeted tumor chemotherapy by ultrasound-activated nanoemulsions/microbubbles. *Journal of Controlled Release*, **138** (3), 268–276.

Razgulin, A., Ma, N., and Rao, J. (2011) Strategies for in vivo imaging of enzyme activity: an overview and recent advances. *Chem. Soc. Rev.*, **40** (7), 4186–4216.

S. Miller, D., and L. Abbott, N. (2013) Influence of droplet size, pH and ionic strength on endotoxin-triggered ordering transitions in liquid crystalline droplets. *Soft Matter*, **9** (2), 374–382.

Saha, K., Agasti, S.S., Kim, C., Li, X., and Rotello, V.M. (2012) Gold Nanoparticles in Chemical and Biological Sensing. *Chem Rev*, **112** (5), 2739–2779.

Sanchez-Dominguez, M., and Rodriguez-Abreu, C. (2016) *Nanocolloids: A Meeting Point for Scientists and Technologists*, Elsevier.

Santangelo, P.J., Nix, B., Tsourkas, A., and Bao, G. (2004) Dual FRET molecular beacons for mRNA detection in living cells. *Nucleic Acids Res*, **32** (6), e57–e57.

Sboros, V. (2008) Response of contrast agents to ultrasound. *Advanced Drug Delivery Reviews*, **60** (10), 1117–1136.

Schutt, E.G., Klein, D.H., Mattrey, R.M., and Riess, J.G. (2003) Injectable Microbubbles as Contrast Agents for Diagnostic Ultrasound Imaging: The Key Role of Perfluorochemicals. *Angewandte Chemie International Edition*, **42** (28), 3218–3235.

Seo, J.-M., Khan, W., and Park, S.-Y. (2012) Protein detection using aqueous/ LC interfaces decorated with a novel polyacrylic acid block liquid crystalline polymer. *Soft Matter*, **8** (1), 198–203.

Setsukinai, K., Urano, Y., Kakinuma, K., Majima, H.J., and Nagano, T. (2003) Development of Novel Fluorescence Probes That Can Reliably Detect Reactive Oxygen Species and Distinguish Specific Species. *J. Biol. Chem.*, **278** (5), 3170–3175.

Shah, R.K., Shum, H.C., Rowat, A.C., Lee, D., Agresti, J.J., Utada, A.S., Chu, L.-Y., Kim, J.-W., Fernandez-Nieves, A., Martinez, C.J., and Weitz, D.A. (2008) Designer emulsions using microfluidics. *Materials Today*, **11** (4), 18–27.

Shaikh, S.R., Dumaual, A.C., Jenski, L.J., and Stillwell, W. (2001) Lipid phase separation in phospholipid bilayers and monolayers modeling the plasma membrane. *Biochimica et Biophysica Acta (BBA) - Biomembranes*, **1512** (2), 317–328.

Shapiro, M.G., Goodwill, P.W., Neogy, A., Yin, M., Foster, F.S., Schaffer, D.V., and Conolly, S.M. (2014) Biogenic gas nanostructures as ultrasonic molecular reporters. *Nature Nanotechnology*, **9** (4), 311–316.

Sheeran, P.S., Matsuura, N., Borden, M.A., Williams, R., Matsunaga, T.O., Burns, P.N., and Dayton, P.A. (2017) Methods of Generating Submicrometer Phase-Shift Perfluorocarbon Droplets for Applications in Medical Ultrasonography. *IEEE Transactions on Ultrasonics, Ferroelectrics, and Frequency Control*, **64** (1), 252–263.

Sheeran, P.S., and Dayton, P.A. (2012) Phase-Change Contrast Agents for Imaging and Therapy. *Curr Pharm Des*, **18** (15), 2152–2165.

Sheeran, P.S., Luois, S., Dayton, P.A., and Matsunaga, T.O. (2011) Formulation and Acoustic Studies of a New Phase-Shift Agent for Diagnostic and Therapeutic Ultrasound. *Langmuir*, **27** (17), 10412–10420.

Sheeran, P.S., Wong, V.P., Luois, S., McFarland, R.J., Ross, W.D., Feingold, S., Matsunaga, T.O., and Dayton, P.A. (2011) Decafluorobutane as a Phase-Change Contrast Agent for Low-Energy Extravascular Ultrasonic Imaging. *Ultrasound in Medicine and Biology*, **37** (9), 1518–1530.

Shpak, O., Verweij, M., Vos, H.J., Jong, N. de, Lohse, D., and Versluis, M. (2014) Acoustic droplet vaporization is initiated by superharmonic focusing. *PNAS*, **111** (5), 1697–1702.

Sirsi, S.R., and Borden, M.A. (2014) State-of-the-art materials for ultrasound-triggered drug delivery. *Advanced Drug Delivery Reviews*, **72**, 3–14.

Sivakumar, S., Wark, K.L., Gupta, J.K., Abbott, N.L., and Caruso, F. (2009) Liquid Crystal Emulsions as the Basis of Biological Sensors for the Optical Detection of Bacteria and Viruses. *Adv. Funct. Mater.*, **19** (14), 2260–2265.

Smoluchowski, M. v. (1918) Versuch einer mathematischen Theorie der Koagulationskinetik kolloider Lösungen. *Zeitschrift für Physikalische Chemie*, **92U** (1), 129–168.

Solans, C., and Solé, I. (2012) Nano-emulsions: Formation by low-energy methods. *Current Opinion in Colloid & Interface Science*, **17** (5), 246–254.

Swift, D.L., and Friedlander, S.K. (1964) The coagulation of hydrosols by brownian motion and laminar shear flow. *Journal of Colloid Science*, **19** (7), 621–647.

Terai, T., and Nagano, T. (2008) Fluorescent probes for bioimaging applications. *Current Opinion in Chemical Biology*, **12** (5), 515–521.

Tighe, P.J., Ryder, R.R., Todd, I., and Fairclough, L.C. (2015) ELISA in the multiplex era: Potentials and pitfalls. *Prot. Clin. Appl.*, **9** (3–4), 406–422.

Tyagi, S., and Kramer, F.R. (1996) Molecular Beacons: Probes that Fluoresce upon Hybridization. *Nature Biotechnology*, **14** (3), 303–308.

Vannan, M.A., and Kuersten, B. (2000) Imaging Techniques for Myocardial Contrast Echocardiography. *Eur J Echocardiogr*, **1** (3), 224–226.

Veatch, S.L., and Keller, S.L. (2002) Organization in Lipid Membranes Containing Cholesterol. *Phys. Rev. Lett.*, **89** (26), 268101.

Veatch, S.L., and Keller, S.L. (2003) Separation of Liquid Phases in Giant Vesicles of Ternary Mixtures of Phospholipids and Cholesterol. *Biophysical Journal*, **85** (5), 3074–3083.

Veatch, S.L., and Keller, S.L. (2005) Seeing spots: Complex phase behavior in simple membranes. *Biochimica et Biophysica Acta (BBA) - Molecular Cell Research*, **1746** (3), 172–185.

Vilela, D., González, M.C., and Escarpa, A. (2012) Sensing colorimetric approaches based on gold and silver nanoparticles aggregation: Chemical creativity behind the assay. A review. *Analytica Chimica Acta*, **751**, 24–43.

von Maltzahn, G., Park, J.-H., Lin, K.Y., Singh, N., Schwöppe, C., Mesters, R., Berdel, W.E., Ruoslahti, E., Sailor, M.J., and Bhatia, S.N. (2011) Nanoparticles that communicate *in vivo* to amplify tumour targeting. *Nature Materials*, **10** (7), 545–552.

Wang, C.-H., Kang, S.-T., Lee, Y.-H., Luo, Y.-L., Huang, Y.-F., and Yeh, C.-K. (2012) Aptamer-conjugated and drug-loaded acoustic droplets for ultrasound theranosis. *Biomaterials*, **33** (6), 1939–1947.

Wang, K., Tang, Z., Yang, C.J., Kim, Y., Fang, X., Li, W., Wu, Y., Medley, C.D., Cao, Z., Li, J., Colon, P., Lin, H., and Tan, W. (2009) Molecular Engineering of DNA: Molecular Beacons. *Angewandte Chemie International Edition*, **48** (5), 856–870.

Wang, X., Bukusoglu, E., and Abbott, N.L. (2017) A Practical Guide to the Preparation of Liquid Crystal-Templated Microparticles. *Chem. Mater.*, **29** (1), 53–61.

Wang, Z., and Yang, S. (2008) Adsorption Behaviors of DPPC/MO Aggregates on SiO2 Surfaces. *Langmuir*, **24** (20), 11616–11624.

Webb, B.A., Chimenti, M., Jacobson, M.P., and Barber, D.L. (2011) Dysregulated pH: a perfect storm for cancer progression. *Nature Reviews Cancer*, **11** (9), 671–677.

Weissleder, R., Tung, C.-H., Mahmood, U., and Jr, A.B. (1999) In vivo imaging of tumors with protease-activated near-infrared fluorescent probes. *Nature Biotechnology*, **17** (4), 375–378.

Wilson, K., Homan, K., and Emelianov, S. (2012) Biomedical photoacoustics beyond thermal expansion using triggered nanodroplet vaporization for contrast-enhanced imaging. *Nature Communications*, **3**, 618.

Xu, S., Zong, Y., Li, W., Zhang, S., and Wan, M. (2014) Bubble size distribution in acoustic droplet vaporization via dissolution using an ultrasound wide-beam method. *Ultrasonics Sonochemistry*, **21** (3), 975–983.

Xu, X., Wang, B., Ye, C., Yao, C., Lin, Y., Huang, X., Zhang, Y., and Wang, S. (2008) Overexpression of macrophage migration inhibitory factor induces angiogenesis in human breast cancer. *Cancer Letters*, **261** (2), 147–157.

Yang, S., Wu, C., Tan, H., Wu, Y., Liao, S., Wu, Z., Shen, G., and Yu, R. (2013) Label-Free Liquid Crystal Biosensor Based on Specific Oligonucleotide Probes for Heavy Metal Ions. *Anal. Chem.*, **85** (1), 14–18.

Yoon, S.H., Gupta, K.C., Borah, J.S., Park, S.-Y., Kim, Y.-K., Lee, J.-H., and Kang, I.-K. (2014) Folate Ligand Anchored Liquid Crystal Microdroplets Emulsion for in Vitro Detection of KB Cancer Cells. *Langmuir*, **30** (35), 10668–10677.

Zarzar, L.D., Sresht, V., Sletten, E.M., Kalow, J.A., Blankschtein, D., and Swager, T.M. (2015) Dynamically reconfigurable complex emulsions via tunable interfacial tensions. *Nature*, **518** (7540), 520–524.

Zhang, P., and Porter, T. (2010) An in vitro Study of a Phase-Shift Nanoemulsion: A Potential Nucleation Agent for Bubble-Enhanced HIFU Tumor Ablation. *Ultrasound in Medicine and Biology*, **36** (11), 1856–1866.

Zhang, X., and Yadavalli, V.K. (2011) Surface immobilization of DNA aptamers for biosensing and protein interaction analysis. *Biosensors and Bioelectronics*, **26** (7), 3142–3147.

Zhao, Z., Al-Ameen, M.A., Duan, K., Ghosh, G., and Fujiou Lo, J. (2015) On-chip porous microgel generation for microfluidic enhanced VEGF detection. *Biosensors and Bioelectronics*, **74**, 305–312.

Zhou, Y., Wang, Z., Chen, Y., Shen, H., Luo, Z., Li, A., Wang, Q., Ran, H., Li, P., Song, W., Yang, Z., Chen, H., Wang, Z., Lu, G., and Zheng, Y. (2013) Microbubbles from Gas-Generating Perfluorohexane Nanoemulsions for Targeted Temperature-Sensitive Ultrasonography and Synergistic HIFU Ablation of Tumors. *Adv. Mater.*, **25** (30), 4123–4130.

Zhu, X.-Q., Wang, C.-H., and Liang, H. (2010) Scales of Oxidation Potentials, pKa, and BDE of Various Hydroquinones and Catechols in DMSO. *J. Org. Chem.*, **75** (21), 7240–7257.